REMOTE SENSING ANALYSIS OF NATURAL OIL AND GAS SEEPS ON THE CONTINENTAL SLOPE OF THE NORTHERN GULF OF MEXICO

A Thesis

by

SOPHIE MAGDALENA DE BEUKELAER

Submitted to the Office of Graduate Studies of
Texas A&M University
in partial fulfillment of the requirements for the degree of

MASTER OF SCIENCE

August 2003

Major Subject: Oceanography

REMOTE SENSING ANALYSIS OF NATURAL OIL AND GAS SEEPS ON THE CONTINENTAL SLOPE OF THE NORTHERN GULF OF MEXICO

A Thesis

by

SOPHIE MAGDALENA DE BEUKELAER

Submitted to Texas A&M University
in partial fulfillment of the requirements
for the degree of

MASTER OF SCIENCE

Approved as to style and content by:

Ian R. MacDonald
(Co-Chair of Committee)

William W. Sager
(Co-Chair of Committee)

Gilbert T. Rowe
(Member)

Raghavan Srinivasan
(Member)

Wilford Gardner
(Head of Department)

August 2003

Major Subject: Oceanography

ABSTRACT

Remote Sensing Analysis of Natural Oil and Gas Seeps on the Continental Slope of the Northern Gulf of Mexico. (August 2003)

Sophie Magdalena De Beukelaer, B.A., New College

Co-Chairs of Advisory Committee: Dr. Ian R. MacDonald
Dr. William W. Sager

Natural hydrocarbon seeps harbor distinctive geological, chemical, and biological features in the marine environment. This thesis verified remote sensing signatures of seeps using in-situ observation and repeated collections of satellite imagery. Bubble streams in the Gulf of Mexico water column from four natural seep sites on the upper continental slope were imaged by a side-scan sonar, which was operated from a submarine near the seafloor, and by acoustic profilers, which were operated from surface ships. These data were correlated with sea surface slicks imaged by Synthetic Aperture Radar (SAR) on the RADARSAT satellite. Comparing non-oily bubble streams from rapidly venting mud volcanoes with oily bubble streams from shallow deposits of gas hydrate showed that they produced notably different signatures. Non-oily bubbles produced high backscatter on the side-scan sonar records, but were difficult to detect with the acoustic profilers. Oily bubbles from hydrate deposits produced acoustic shadows on the side-scan sonar records. The oily bubbles generated clear signatures extending from the seafloor to the near surface on the acoustic profile records. RADARSAT SAR images verified the presence of surface oil slicks over the hydrate deposits, but not over the mud volcanoes. This indicates that SAR imagery will not be able to capture every oil and gas seep in a region because non-oily bubble streams do not create surface oil slicks. A total of 113 natural oily seep sources were identified based on surface slicks in eleven SAR images collected over the northern continental slope. A persistence analysis verified that SAR is a dependable tool for capturing oil slicks because 93.5% of the slick sources identified in the 2001 images were corroborated with slicks in the 2002 images. The sources ranged in depth from 100 to 2000 m and 79% of the sources were in 900 meters or greater of water. Seventy-six percent of the seep sources were associated with salt less than 1500 m below the seafloor and none of the sources were located in the bottom of salt withdrawal basins. Geographical Information Systems (GIS) proved to be a useful tool in these analyses.

ACKNOWLEDGEMENTS

I am grateful for having had the opportunity to conduct most of my graduate research offshore and underwater. Thanks to Gil Rowe and Ian MacDonald for introducing me to deep-sea research and giving me the opportunity to learn invaluable information outside of the classroom. I value Dr. Srinivasan's insights and support of my research and work. Thank you to Will Sager for agreeing to co-chair my committee towards this projects completion. I appreciate being able to work at the Geochemical and Environmental Research Group (GERG) and am grateful for the rich resources in people and equipment that the organization gave me. I am especially appreciative of Norman Guinasso's constructive criticism of my thesis and his suggestions for improving the arguments in my work. Thanks to the crew from the *R/V Gyre* and *R/V Seward Johnson I and II* for enriching my offshore experiences. Desmond Power and C-core processed the original RADARSAT images and were very helpful with the SAR imagery analysis. I am also thankful for having worked with John "Voyager" Murray and appreciate his patience and collaboration during the side-scan sonar surveys on the Johnson Sea Link submarine. Thanks to all of my friends for their endless support and encouragement during my graduate school years, I could not have done it without you!

TABLE OF CONTENTS

Page

LIST OF FIGURES

FIGURE Page

LIST OF TABLES

CHAPTER I

INTRODUCTION AND LITERATURE REVIEW

INTRODUCTION

Natural hydrocarbon seeps on the continental slope of the northern Gulf of Mexico slope apparently produce distinctive remote sensing signatures. However, the characteristics of seeps in the water column and their temporal variability require further investigation. The objectives of this research were to investigate water column signatures of natural oil and gas seeps, to correlate those findings with sea surface expressions, to catalog the regional extent of oil slicks and their sources on the northern continental slope, and to compare the sources with geologic features. Locating and quantifying seeps is of interest to the scientific community, oil and gas companies, and the Minerals Management Service (MMS) because seeps supply organic carbon to the benthos and water column, they can be indicative of the extent of mature oil sources on the slope, and seeps are correlated to interesting diverse small- and large-scale biological and geological features. The hydrocarbon signatures of seeps and biological communities as related to this research are briefly outlined in this chapter. I will further provide information on the use of satellite imagery for detecting seeps.

In order to interpret Synthetic Aperture Radar (SAR) data correctly, we need to understand how oil is transferred from the seafloor through the water column to the sea surface. In the Chapter II, I present results of acoustic profile surveys of oil and gas streams rising from seeps. Further information on characteristics of these bubble streams was obtained by side scan sonar surveys conducted at the sea floor by a submersible. These results were used to constrain my interpretation of the satellite data.

This thesis follows the style and format of Geo-Marine Letters.

In the Chapter III, I analyze RADARSAT SAR images collected in two intensive periods separated by an interval of one year. These results confirm the temporal persistence of seep signatures and provide a catalog of seep locations. Historic data on slope geology are examined to determine correlation between seep locations and geologic features.

LITERATURE REVIEW

Hydrocarbon seepage and its associated geologic features

Seeps are streams of naturally occurring hydrocarbons that migrate from below the sediments and can flow through the water column as oil drops, bubbles, and oily coated bubbles. Deeply buried Mesozoic and Cenozoic carbonate and siliclastic source rocks have reached maturation and provide the hydrocarbon source for the natural oil and gas seeps on the northern Gulf of Mexico continental slope (Sassen et al. 2001a). The hydrocarbons migrate over six vertical kilometers to Miocene and Pleistocene reservoirs, and then proceed to migrate to the seafloor through near-surface faults (Reilly et al. 1996). These faults can be a result of the movement by the subsurface salt layer and local failures of the slope. The subsurface salt layer is referred to as the Louann Salt and was deformed by the rapid sedimentation that followed the salt deposition during the Middle Jurassic. The characteristics of the allochthonous salt layer continue to be altered by halokinesis and its effects are evident in the "hummocky" (Bouma and Roberts 1990) appearance of the seafloor bathymetry of the continental slope (Bryant et al. 1990, 1991). Vertical oil and gas migration is thought to be focused "at the edges of actively charged salt-withdrawal mini-basins, over salt ridges, and near the Sigsbee Escarpment (Sassen et al. 1999)," which is the southern edge of the Louann Salt.

The continental slope of the northern Gulf of Mexico supports about 90 intraslope basins with approximately 20 basins each in the Garden Banks, Green Canyon, and Keathly Canyon Lease Areas (Bryant et al. 1990). Local inclines can be as great as 40º at the sides or flanks of basins and mounds but the average continental slope incline is about 1º. Interlobal basins shaped by deeply rooted salt and by coalescing salt tongues, are dominant on the upper continental slope (Fig. I-1). Seeps are hypothesized to be more prevalent on the upper continental slope in relation with these interlobal basins rather than with the more circular supralobal basins evident on the lower slope (Bryant, personal communication). The supralobal basins are thought to be formed by the downbuilding of salt and are patchier than the irregular shaped basins on the upper slope. Therefore, oil and gas seeps are not as common on the lower and middle slope as they are on the upper slope.

The continental slope of the northern Gulf of Mexico is an economically important hydrocarbon basin. As oil-drilling technologies improve and reservoirs on the continental shelf are depleted, more companies are leasing drilling areas on the slope. The number and extent of natural oil and gas seeps on the slope reveal the promise of economically viable reservoirs. In order to investigate areas for potential hydrocarbon reservoirs, oil companies can use expensive 3-D seismic data.

Three-dimensional seismic data can reveal the extent of the salt, the linearity of the sediment layers, and possible faults. Reilly et al. (1996) suggest that only antithetic faults connected to regional growth faults are conducive to continuous seepage, which would be necessary to support a chemosynthetic community reliant on the seeps' hydrocarbons. High amplitude or "wipe-out" zones on 3-D seismic records can be indicative of gas reservoirs, which can be associated with seeps (Roberts 1996; Roberts et al. 1996, 2002). So, geophysical data provides information on the distribution and persistence of seeps over geologic time. However, contemporary temporal and spatial changes are regulated by geologic, biological, and chemical processes that may not be evident in such data.

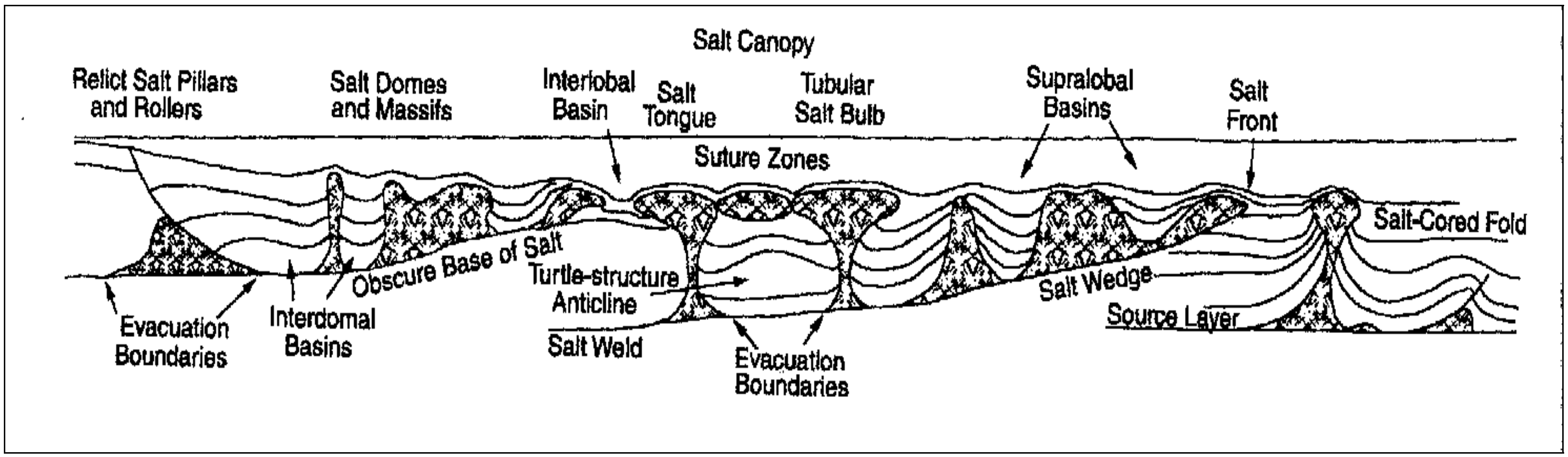

Fig. I-1. Cross-section of the subsurface salt structure of the north central Gulf of Mexico slope from north (left) to south (right) with the salt-cored fold representing Green Knoll (Simmons et al. 1996).

Temporal changes in seeps

Temporal changes in natural oil and gas seepage can be caused by various alterations to the current geologic state of its environment. The intensity and activity of flowing seepage is partially controlled by tectonics (MacGregor 1993), so we see changes in seepage due to aperiodic salt movement on the continental slope (Roberts et al. 1990). The intensity of the natural seepage can also be altered due to its connection to commercially exploited oil reservoirs (Kvenvolden and Harbaugh 1983). A 50% decrease in natural marine hydrocarbon seepage near Coal Point, California has been attributed to offshore oil production leading to the decline of reservoir pressure and hydrocarbon sources (Quigley et al. 1999). The Joilliet tension-legwork platform installed in 1989 in GC184 extracts hydrocarbons from the same source that provides oil and gas to the Bush Hill (GC185) chemosynthetic community (Kennicutt et al. 1988b). No alterations in the seepage rates have been recognized by researchers who have studied other aspects of the seep but no specific study has investigated this issue at Bush Hill.

Gas hydrates are a component of seafloor seeps (Brooks et al. 1984) and changes in hydrate stability can create temporally discernible changes in oil and gas seepage. Hydrate is thought to form in two different ways: as structure I, which consists of pure methane depleted in ^{13}C and as structure II, which contains C_1-C_4 hydrocarbons. Structure II hydrate is more stable that structure I hydrate (Fig. I-2). Destabilization of gas hydrate by hydrostatic pressure changes or temperature changes can cause inter- and intra-annual alterations in gas release (Roberts and Carney 1997; MacDonald et al. 2000). For example, warm core eddies splitting off from the Loop Current can cause warm water to sink which affects the stability of the shallow gas hydrate on the continental slope (Roberts et al. 2001). The upper slope bottom temperatures can be raised 4 to 6º C due to these anti-cyclonic eddies (Hamilton 1990). In this manner, the water temperature can be elevated above the stability level of the hydrate, which causes it to dissociate and release gas and oil. Hydrate can also clog the migration pathways of the oil and gas and prevent continued seepage, although usually the presence of hydrate in the area does not obstruct gas venting into the water column (Brooks et al. 1994).

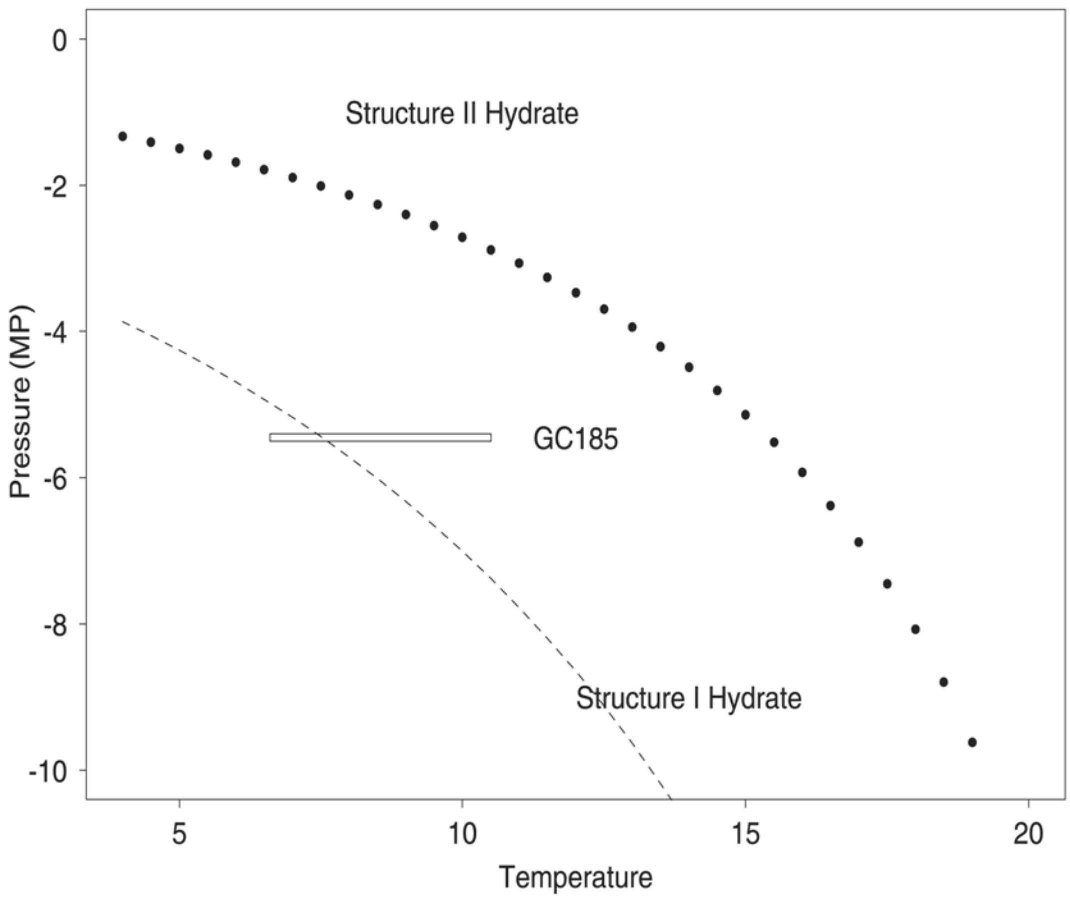

Fig. I-2. Stability fields for hydrate structures I and II. The pressure temperature region for Bush Hill (GC185) is indicated as a box, so Structure II hydrate is likely to be the only stable structure at the site (Prepared by Norman Guinasso using Sloan's CSMHYD dated 8/20/96 (MacDonald 2002)).

Mud volcanoes can be impressive geologic features formed by rapidly migrating fluids, gasses, and sediments (Roberts and Carney 1997). The conical mounds, which can be up to a kilometer wide and 50 meters high, appear to have a vertical pathway through which oil and gas can be discharged. The episodic eruptions of mud volcanoes seem to be tied to rapid fluctuations in the water temperature (MacDonald et al. 2000). This episodic nature and rapid venting, which also creates complimentary extruded mud sheets, tend to inhibit colonization of chemosynthetic organisms more complex than bacteria. Thus, hydrocarbons from these mud volcanoes tend to be non-biodegraded (Roberts and Carney 1997; Roberts et al. 2001).

Hydrocarbons

The life span of oil on the sea surface is dependent on many factors and is influenced by numerous parameters. Crude oils include light-, medium-, and heavyweight components containing from ten to more than twenty carbon atoms, respectively (MacDonald et al. 2002). The ratio of hydrogen and carbon atoms in oil is about 1.85 H to 1 C (Hunt 1979). Oil is also composed of a small amount of sulfur, nitrogen, and oxygen but 84.5% of the oil is carbon (Hunt 1979). On the surface, the oil spreads downwind with a speed that is dependent on the oils' viscosity. The lighter components of the oil will evaporate first but high winds and temperatures can increase the evaporation rate of the heavier components. The slicks will be dispersed by waves and turbulence, which also influences the dissolution of the oil in the upper water column. Biodegradation by microbes and adhesion to sediment or organic matter can remove the oil from the sea surface. A photochemical parameter that affects the life span of the slick is oxidation of the oil, which can form soluble products or compounds such as tar.

Oil and gas are the products of the transformation of organic matter in an anoxic environment. Seeping gas can be either of thermogenic or biogenic origin. Within 100 m of the seafloor, free thermogenic and biogenic gas in patches of 250 to 500 m in width can be found all over the Gulf of Mexico slope (Anderson and Bryant 1990). The existence of a bubbling gas stream, rising through the water column can be confirmed by acoustic surveys (Addy and Worzel 1979). The origin of the gas must be resolved by analyzing the geochemical composition of the bubbles. As the hydrocarbon flux through the sediment decreases, the oil is more heavily degraded by bacterial oxidation (Roberts and Carney 1997). Depletion in ^{13}C is a good indication that the sample, whether gas or carbonate rock, is of biogenic origin (Kennicutt et al. 1988a).

The water column carbon chemistry at seep sites is quite different than the surrounding deep-sea water column chemistry. At seeps there is an increased level of dissolved inorganic carbon (DIC) and a decreased value of δ^{13} C as compared to non-seep sites (Aharon et al. 1992). These anomalies are attributed to the product of carbon dioxide from microbial oxidation of the oil, which has a δ^{13} C composition of –26.0 ‰, from the seep (Aharon et al. 1992). Investigations into how this affects the carbon cycle must still be undertaken.

Carbon flux is an important aspect of oceanography because carbon is the building block of life. The carbon flux from seeps to the water column can be significant. Oil seepage in the Gulf of Mexico is estimated to be on the order of 0.4 to 1.1 x 10^8 liters per year as based on remote sensing imagery (Mitchell et al. 1999). Bubble streams comprise most of the carbon entering the water column. When bubbles coated with oil reach the surface, the gas escapes to the atmosphere and the oil remains on the surface. This surface slick can reduce gas fluxes between the atmosphere and water column, however, this probably does not influence the carbon cycle globally.

Biological communities

Carbon flux provides a nutrient source in the deep sea. Sediments affected by seepage are many orders of a magnitude greater in hydrocarbon concentrations than other deep-sea sediments. Typical seep sediments have as much as 10% of volume of liquid oil, which can lead to a formation of a distinctive benthic ecosystem. Basic biological response to the presence of hydrocarbons is consumption by free-living bacteria, which rapidly oxidize the hydrocarbons starting with methane. The secondary effect of biological response to the hydrocarbons is to produce high concentrations of hydrogen sulfide in the porefluids. Hydrogen sulfide production results from anaerobic hydrocarbon oxidation of water column sulfate by a consortium of archaea and sulfate reducing bacteria (Boetius et al. 2000). The seafloor environment of the seep vicinity is most dramatically changed by chemosynthetic metazoans such as clams, tubeworms, and mussels. These metazoans are supported by symbiotic bacteria and can be methanotrophic, as in the case with seep mussels or thiotrophic, as in the case with clams (Fisher 1990). These organisms can achieve very high densities at seeps (MacDonald et al. 1989) and collectively they transform the seep into a lush ecological setting referred to as a chemosynthetic community.

Chemosynthetic communities can be categorized according to the amount of fluid-gas flux (Roberts and Carney 1997; Roberts et al. 2001) or by style (MacDonald et al. 2002). Roberts and Carney (1997) compared the biological, chemical, and geological features in rapid, to transitional, to slow flux areas. Rapid venting by mud volcanoes, mud flows and gas expulsion features tend to support only localized communities and release non-biodegraded hydrocarbons. Transitional flux areas support a more diverse and widespread chemosynthetic community around isolated authigenic carbonates and possible hydrate mounds. Slow flux hydrocarbons tend to be very biodegraded and support only localized communities around authigenic carbonate mounds and nodules and possible mineralized cones and chimneys. Meanwhile, MacDonald (2002) describes hydrocarbon seeps according to seafloor phenomenology. He suggests two categories: sediment diffusion seeps and brine pooling seeps. Sediment diffusion seeps support widespread tubeworm bushes, bivalves, and sulfide-oxidizing bacteria. Authigenic carbonates and gas hydrates are prominent geological features at the sediment diffusion seeps. Brine pools contain hypersaline fluids with the potential of supporting large mussel beds if the interface between the brine and the seawater is sharp (~1 cm) (MacDonald et al. 1990). So, the structure of a biological community can indicate the approximate flux rate, as well as the temporal variability, of a seep. For example, the presence of large tubeworm bushes within the community can indicate continued seepage for over 100 years (Bergquist et al. 2000).

Seeps are an important aspect of deep-sea biology not only because they support chemosynthetic organisms, but because of their influence on non-endemic fauna such as benthic predators. The endemic mega-benthos found in a chemosynthetic community rely primarily on the symbiosis with chemoautotrophic bacteria as a nutritional resource (Hyun et al. 1997). Isotopic analysis of these invertebrates suggests a $\delta^{13}C$ depleted carbon source, which the hydrocarbons from the natural oil seeps provide. The carbon isotope composition of trawled chemosynthetic invertebrates was found to range from –14 to –58 $^0/_{00}$ (Kennicutt et al. 1988a). Carbon isotope compositions of predators, non-endemic fauna of a chemosynthetic community, showed that they complemented their photosynthetic-derived diet with a substantial amount of chemosynthetic biomass (MacAvoy et al. 2002).

Biological functions can also generate significant geological features in an area surrounding a seep. The bacterial oxidation of the thermogenic hydrocarbon gas precipitates authigenic carbonate rock thus modifying the sea-floor geology (Sassen et al. 1998). The carbonates have $\delta^{13}C$ values ranging from –19.4 to –32.6 $^0/_{00}$ (Hyun et al. 1997) if they are in crude oil prone areas, but at methane-prone areas the $\delta^{13}C$ can range from –45 to –58 % Pee Dee Belemnite (Roberts et al. 2001). These authigenic carbonates are long-term geological expressions of natural oil and gas seeps (Roberts et al. 1990). The authigenic carbonates can form crusts, hardgrounds, nodular masses, and mound-like buildups to large mounds that can be several meters in height (Roberts et al. 2001).

Identifying natural oil and gas seeps on satellite images

A significant part of the oil and gas at natural seeps is consumed at the seafloor. However, a fraction of the oil and gas escape into the water column and rise to the sea surface. The fate of gas is uncertain, much may dissolve in the water column (Leifer and MacDonald 2003). The oil that does reach the surface forms a thin layer that floats downstream with the wind and current (MacDonald et al. 2002). For the purpose of this thesis, a consistent terminology will be used to describe the components of the seep process.

The terminology includes (MacDonald 1993, 2002; Venkataramaiah 1996):

1. **Seep source**: the seafloor position from which oil and gas escape
2. **Bubble stream**: the water column signature of an oil and gas seep
3. **Slick origin (surfacing footprint)**: the leading end of the slicks on the sea surface
4. **Slick**: the drift path of particles on the sea surface
5. **Surfacing perimeter:** the area within which the slick origins can be observed over time. The surfacing perimeter is dependent on the velocity and direction of the water column currents, as well as on the depth of the source.

The bubble streams and slicks have been referred to as "plumes." This can be misleading because unlike a true plume, a bubble stream or a surface slick does not become measurably broader and more diffuse as it migrates from its source. One of the objectives in this research was to substantiate the water column signatures and the surface signatures of seeps.

Satellite imagery has been used successfully to resolve the regional extent of natural seeps (MacDonald et al. 1996). Reilly (1995) suggests that the first step to finding a chemosynthetic community is by the identification of a surface slicks. MacDonald et al. (1996) identified 63 natural seep sources on the northern continental slope of the Gulf of Mexico based on satellite imagery that included a space shuttle photograph, a Landsat Thematic Mapper scene, and three European Radar Satellite scenes. These sources and the location of 43 chemosynthetic communities, confirmed by pictures from a photosled, ROV and submersible surveys, and trawling were located on the continental slope (MacDonald et al. 1996) and are depicted in Figure I-4. It was noted that slicks were often found in persistent locations, many of which coincided with known chemosynthetic community sites (MacDonald et al. 1993). From this research it appeared that relatively continuous expressions are recognizable on the sea surface above moderate and slow flux seeps. However, pulsed signals from high flux seeps, such as those from an eruption from a mud volcano, were more difficult to detect due to their temporal variability (MacDonald et al. 2000). Orange et al. (2002) suggest that gassy streams “may not produce pronounced sea surface slicks.” Therefore, the sensitivity of satellite imaging to the full range of seepage types and its ability to resolve temporal variability requires further investigation.

Synthetic Aperture Radar (SAR) has been a proven tool used for depicting oil slicks on the surface of the sea (MacDonald et al. 1996; Espedal et al. 1996). The SAR instrument is placed on a satellite and can image the sea surface both day and night. SAR transmits and receives microwaves that are not inhibited by clouds or rainstorms and are also about the same length (5.6 cm) as the sea surface waves that cause Bragg scattering. Slicks dampen Bragg scattering waves and appear dark on resulting satellite images. RARSAT SAR has been especially successful in detecting slicks because of its use of steep, 20-30º, incidence angles. RADARSAT orbits the Earth 14 times a day the Earth at an altitude of 798 kilometers.

Surface slick expression depends on the surface wind and currents. The optimal wind speed at which to view these expressions is between 3 and 10 m/s because when the wind speed is below 3 m/s the slicks can’t be distinguished from the smooth sea and above 10 m/s, the slicks are dispersed. The summer months can provide the most optimal wind conditions over the Gulf of Mexico when considering SAR collections. Warm-core eddies direct the flow of the surface expressions of slicks because the eddies dominate the surface currents of the deep Northern Gulf of Mexico (Guinasso 2002).

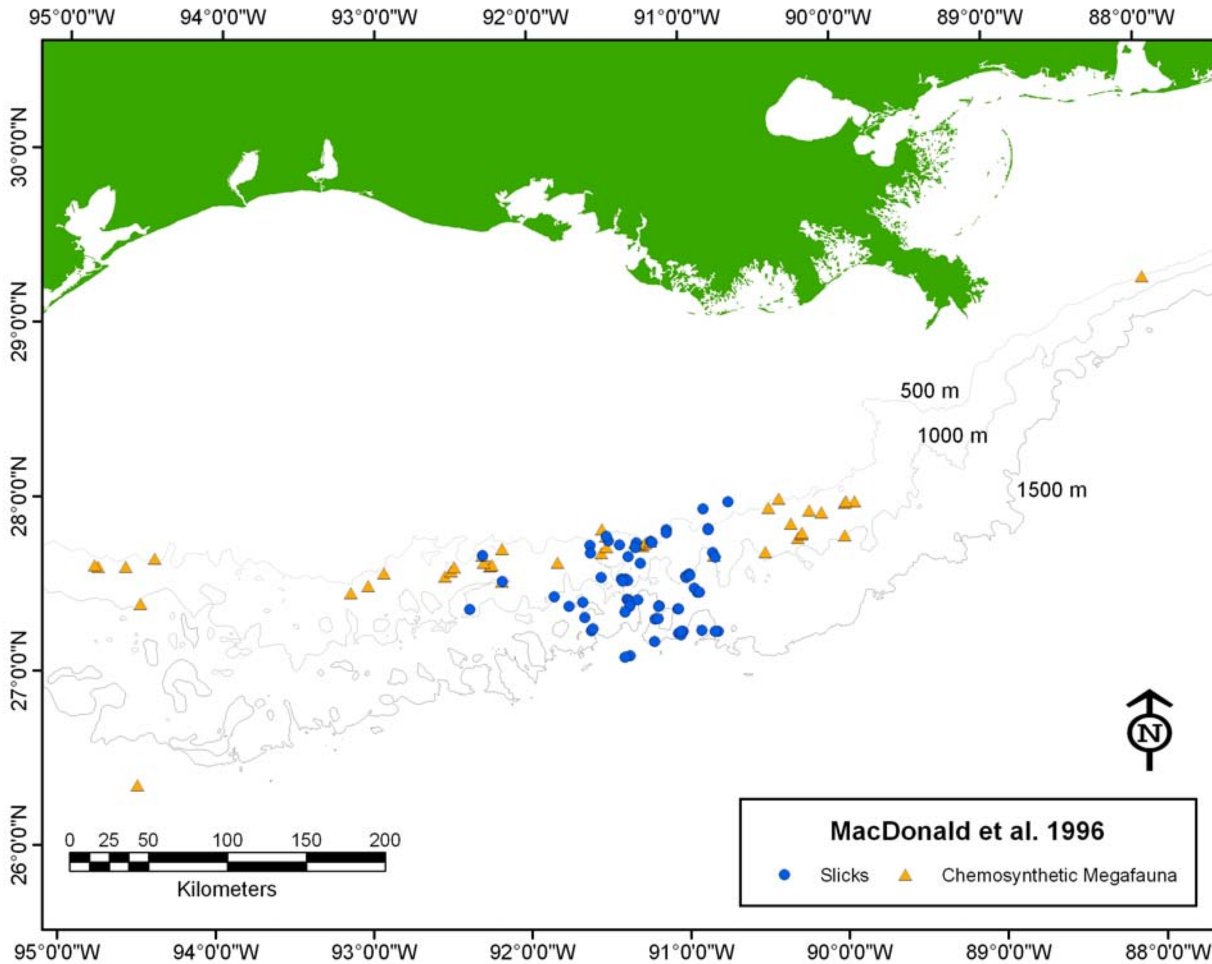

Fig. I-3. Slicks (blue dots) and chemosynthetic megafauna (yellow triangles) located on the continental slope of the northern Gulf of Mexico (locations from MacDonald et al. 1996).

Both bottom and surface currents influence where the slick will surface relative to the seafloor vent. Venkataramaiah (1996) showed that an increased linear horizontal velocity leads to a greater lateral or horizontal offset of a slick from a seep. On average the origins of the slicks on the surface are displaced about 1000 m laterally from the seafloor vent (MacDonald et al. 2002). The offset can be caused by bottom currents, which flow to the east at a mean of 10 cm/s between the water depths of 500 to 1000 m and along the slope at 5 cm/s to the west or southwest in deeper waters, 2000 to 3000 m (Carney 2002). Detailed studies of temperature and currents have found diurnal periodicity in the water temperature and current speed for sites at 500 to 600 m in depth. This suggests that bottom currents at these depths can be tidally forced and studies are underway to determine the extent of this influence (MacDonald et al. 2003).

CHAPTER II

DISTINCT SIDE-SCAN SONAR, RADARSAT SAR, AND ACOUSTIC PROFILER SIGNATURES OF OIL AND GAS SEEPS ON THE GULF OF MEXICO SLOPE

INTRODUCTION

Natural oil and gas seeps are widespread across the northern Gulf of Mexico slope. At seeps, the geology and ecology of the seafloor is greatly affected by supply of organic carbon (Roberts et al. 2001; MacDonald et al. 1989). Geologic features found at seeps include massive carbonates, gas hydrate deposits, mud and/or brine flows, and pockmarks (Sager et al. 1998; Sager et al. in press). Biota at active seeps includes chemoautotrophic bacteria and tubeworms or mollusks with bacterial symbionts (Fisher 1990; Childress et al. 1986). Accurate estimates for the number of seeps and their distribution are important for assessing the impact of hydrocarbon seepage on basin-wide carbon cycling, zoogeography, and resource management.

The areas affected by seepage can be on the order of a square kilometer or more. Typically, gas and oil escape into the water from discrete vents within a larger seep site. Gas is released as small (1-10 mm) bubbles (Leifer and MacDonald 2003). When oil is present, such as at Minerals Management Services (MMS) Lease Block Green Canyon 185 and Green Canyon 234, the oil usually coats the walls of the bubbles or rises as gassy droplets (Leifer and MacDonald 2003). When the oil reaches the surface, it spreads into thin, very elongated layers that coalesce and are then recognized as “slicks” because they tend to suppress surface wavelets. Slicks are readily detected by satellite remote sensing methods such as Synthetic Aperture Radar (SAR). Remote sensing surveys of the northern slope have been used to quantify the total magnitude of seepage and its distribution (Kornacki et al. 1994; MacDonald et al. 1996; Mitchell et al. 2000).

One shortcoming in this approach is the lack of information about what happens to the oil and gas between its departure from the seafloor, where observers in submarines can see it, and the appearance of oil as slicks on the sea surface, where the slicks can be detected by SAR. Furthermore, although it is possible to observe individual gas and oil vents within a seep, the bubble eruptions are often ephemeral features, making it difficult to map all of the active vents within a given seep area. Ultimately, the flux of carbon from natural hydrocarbon seeps depends on the number and size of individual gas and oil streams. This paper is intended to document gas and oil discharge within four representative seep areas on the upper continental slope where the general locations of venting was known and from which we can extrapolate the results to other seep areas on the northern continental slope. Using acoustic profiles, we were able to trace the origins of the bubble streams from the seeps to specific seafloor locations. Side-scan sonar surveys were then used to detect fine scale details of the bubble streams at the seep sites beyond the limited field of view from the submarine. Furthermore, repeated remote sensing imaging was available to confirm the continued formation, or lack, of sea surface oil slicks above the explored seep areas. These results verify suppositions concerning the complex shapes of floating slicks and provide a basis for extrapolating from the details of remote sensing surveys to regional estimates of the total number of oil and gas vents.

SITES

The four sites (Fig. II-1) examined in this study represent a variety of seep types. Bush Hill in MMS Lease Block Green Canyon 185 (GC185) and Green Canyon 234 (GC234) are both considered moderate flux seep sites and support complex communities made up of the seep-mussels (*Bathymodiolus childressi*, Mytilidae: Bivalvia), lucinid and vesycomyid clams, vestimentiferan tube worms and bacterial mats (*Beggiatoa*) (Roberts and Carney 1997; Roberts et al. 2001). Bush Hill is a prominent mound about 700 m in base diameter and rising 30 to 40 m above the surrounding seafloor with an average depth of 580 meters (MacDonald et al. 1989). GC234 is a half-graben containing numerous faults and discharge zones arrayed across an east-to-west distance of ~1.5 km at depths ranging from 525 to 560 meters (MacDonald et al. 1990b; Reilly et al. 1996). GC185 and GC234 are characterized by high concentrations (as much as 10% by volume) of liquid oil in surface sediments and by gas comprised of significant fractions of ethane, propane, and butane, as well as methane. Gas hydrates at the sites have been identified as comprising structure II hydrate (Sassen et al. 1998). Bubbles from the sites have an oily coating (Leifer and MacDonald 2003). As a result, seeps at both GC185 and GC234 produce perennial slicks detected by satellite imagery (MacDonald et al. 1996).

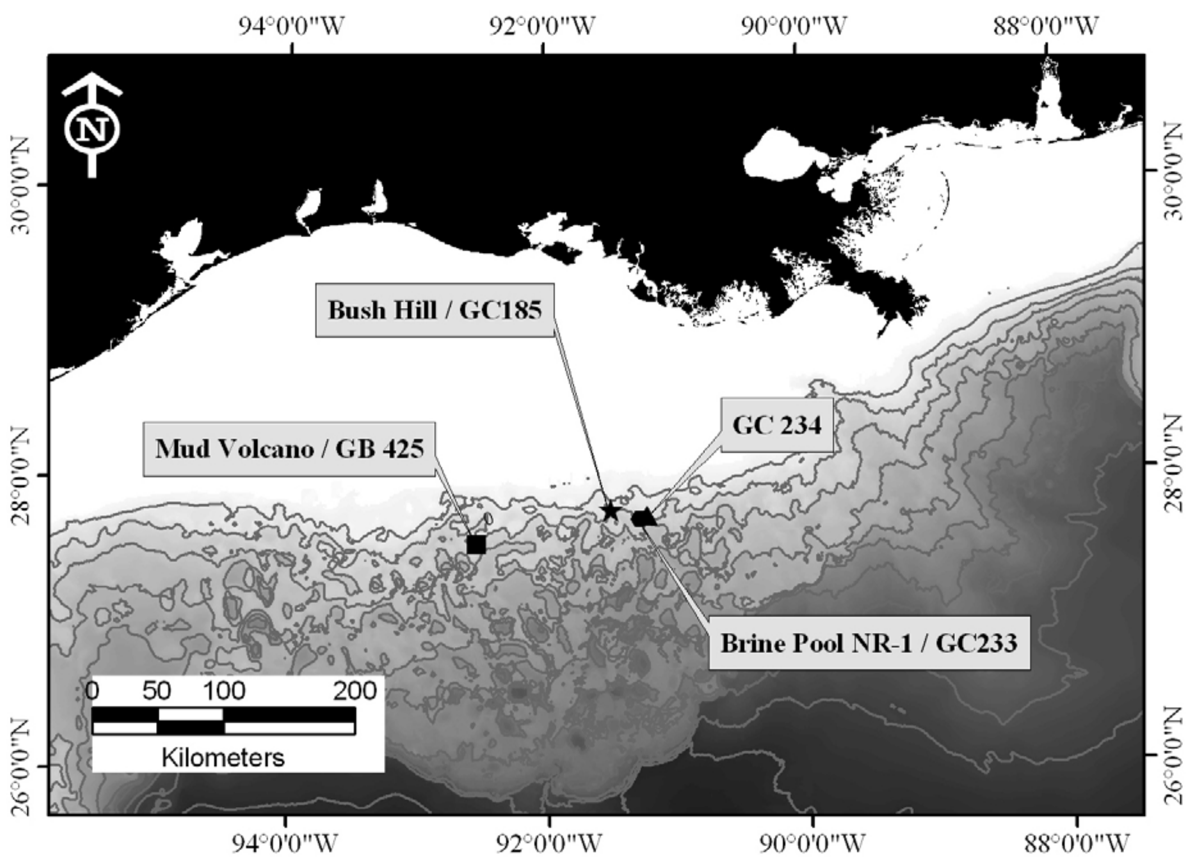

Fig. II-1. Location of study sites on the Gulf of Mexico continental slope south of Louisiana. Depth contour intervals are 300 meters.

The other two sites differed from those described above because they were areas of rapid, focused fluid discharge characterized by mud volcanoes and pools of hypersaline fluid. The study investigated the area around the large Brine Pool NR-1 surrounded by *Bathymodiolus childressi* in GC233 at 650 m depth, where gas containing >99% methane emanates through the center of the pool (MacDonald et al. 1990). The Brine Pool NR-1 is located above an inactive mud volcano. The dominant feature of the fourth site, GB425, is an active rapid venting mud-volcano surrounded by recognizable mudflows at a depth of 600 m. The edges of the mud volcano are colonized by seep mussels and bacterial mats. Venting gas at this site is also >99% methane (MacDonald et al. 2000). The gas bubbles at these two sites, GC233 and GB425, did not to have an evident oily coating (Leifer and MacDonald 2003).

METHODS

Acoustic profiling of streams in water column

Gas bubbles can be imaged using acoustic profiling techniques because of the acoustic impedance difference between gas and water. However, acoustic profiling instruments are intended to be used for depth finding or sub bottom profiling, so it was generally necessary to increase the gain of the instrument output in order to display the return from the gas in the water column. We used two acoustic instruments to detect bubble streams in the water column from the sea surface: A Datasonics Chirp II Acoustic profiling system at 10 kHz and a Simrad EQ50 echo sounder operating at 38/50 kHZ. The profiles conducted in July 2001 were based only on the Chirp II results but the Simrad results complement the Chirp II profiles in July 2002. The beam angles of these profilers were approximately 30º. Survey grids consisted of a series of straight track lines, which were 2 to 7 km in length, arrayed above known chemosynthetic communities where gas seepage was expected.

Side-scan sonar mapping of individual gas vents

To collect detailed information on gas venting and associated geological features, we used a high frequency side-scan sonar mounted under the *Johnson Sea Link* (JSL), a submarine utilized for oceanographic research. Deployed from its support vessel, *R/V Seward Johnson II*, the JSL completed four 3-hour side-scan surveys (Table II-1). The side scan sonar we used was a dual frequency (100 and 384 kHz) EdgeTech DF-1000. The optimal sonar range was 50 m but a 100 m range was also successfully used for several survey lines.

The side-scan surveys were planned to cover the locations of the streams previously detected in the acoustic surveys, while the target points and track lines were arrayed to optimize visual sighting of gas venting by the observers and subsequent sonar detection. Navigation was provided by short baseline (ORE Trackpoint II) acoustic transponders synchronized with the GPS from the *R/V Seward Johnson II*. The average speed of the JSL was 0.8 knots during the surveys but the submersible often had to stop to allow the surface ship to regain tracking of the submarine. The altitude of the JSL was generally ~1 m, but occasionally reached 4 meters off of the bottom.

Table II-1. Side-scan sonar surveys details. For location see Fig. II-1. Lines refer to individual track lines and stops were navigation fixes.

Date	**Dive**	**Location**	**Lines**	**Stops**
July 4, 2002	4443	GC185 (Bush Hill)	16	4
July 7, 2002	4449	GC234	6	12
July 13, 2002	4457	GC233 (Brine Pool)	13	20
July 19, 2002	4466	GB425 (Mud Volcano)	6	9

RADARSAT SAR images of oil slicks

The satellite employed by RADARSAT acquired 11 Synthetic Aperture Radar (SAR) images covering the extent of the Green Canyon MMS Lease Blocks (Table II-2).

SAR can be used to capture regional oil seepage events on the ocean surface. Utilizing C-band radar, SAR transmits and receives microwaves that are not impeded by cloud cover and allows for 24-hour surveillance of the sea surface. Because SAR images detect the backscatter from the ocean surface, the slicks appear dark because the Bragg scattering is dampened by even a very thin layer of oil on the sea surface (Hovland-Espedal et al. 1994).

The SAR images were first rectified in ERMapper using the corner points given by the Canadian Space Agency Data for Research Use (CSA DRU). The images were then more precisely georeferenced in ArcMap to coordinates of oil platforms, which are easily identified in the SAR images. The surface oil slicks from all images were manually traced and made into a shape file for each individual image. Incorporating all of the shape files into one GIS project allowed for spatial interpretations of the slicks.

Table II-2. Details of Synthetic Aperture Radar (SAR) images collected with RADARSAT over the northern continental slope of the Gulf of Mexico. The SAR wide 1 and 2 settings have swath widths of 160 km and 150 km, respectively, compared to the SAR Standard, which has a swath width of 100 km.

Date	**UTC**	**Beam Mode**	**Orbit**	**Incidence Angle**	**Resolution**
7/9/2001	12:12	Wide2	Descending	30.8º - 39.5º	~27 m
7/12/2001	0:05	Wide2	Ascending	30.8º - 39.5º	~27 m
7/16/2001	12:08	Wide1	Descending	20.0º- 31.2º	~35 m
7/19/2001	0:01	Wide1	Ascending	20.0º- 31.2º	~35 m
7/22/2001	0:13	Standard 6	Ascending	41.4º- 46.5º	~25 m
6/10/2002	12:12	Wide1	Descending	20.0º- 31.2º	~35 m
6/17/2002	12:08	Wide1	Descending	20.0º- 31.2º	~35 m
6/20/2002	0:01	Standard 2	Ascending	24.2º- 31.2º	~25 m
7/4/2002	12:12	Wide1	Descending	20.0º- 31.2º	~35 m
7/11/2002	12:08	Wide1	Descending	20.0º- 31.2º	~35 m
7/14/2002	0:01	Standard 2	Ascending	24.2º- 31.2º	~25 m

RESULTS

Bubble streams in the water column

We detected bubble streams in the water column at all four of our study areas. Bubble streams were evident as "hyperbolic echoes" (Addy and Worzel 1979) in acoustic profiler records and emanated from a traceable origin on the seafloor. The breadth and distribution of the active bubble streams were readily identified at the seep sites. However, the oily bubble streams displayed different signatures than the non-oily bubble streams on the acoustic records.

The oily bubble streams from the GC234 and GC185 study areas were broad, columnar regions of enhanced backscatter that appeared to narrow as they approached the surface. In GC185 at the Bush Hill site, the 2001 survey (Fig. II-2) detected one set of bubble streams rising from the crest of the main mound and a second set originating from a site ~1.2 km west of the mound. Both bubble streams appeared to include a main column from a distinct origin and a fainter, secondary stream from a less distinct origin. The streams were both noticeably deflected toward the east as they approached the surface until the scattering in the upper 100 meters obscured the return. When we returned to the site in 2002, we did not detect any streams west from Bush Hill.

The non-oily bubble streams detected at GB425 and GC233 produced a different acoustic image. The streams were much wider than those at GC185 and GC234 and these streams only extended to about 150 m above the seafloor. The bubble streams were not noticeably deflected in the water column and they never reached the sea surface on the acoustic profiler records. In 2002 we successfully imaged the bubble stream above Brine Pool NR-1 in GC233 but were unable to do so in the 2001 survey. Acoustic profiles were conducted at GB425 in 2002. Short, wide bubble streams were only detected by the higher frequency Simrad echo sounder, not with the Chirp profiler.

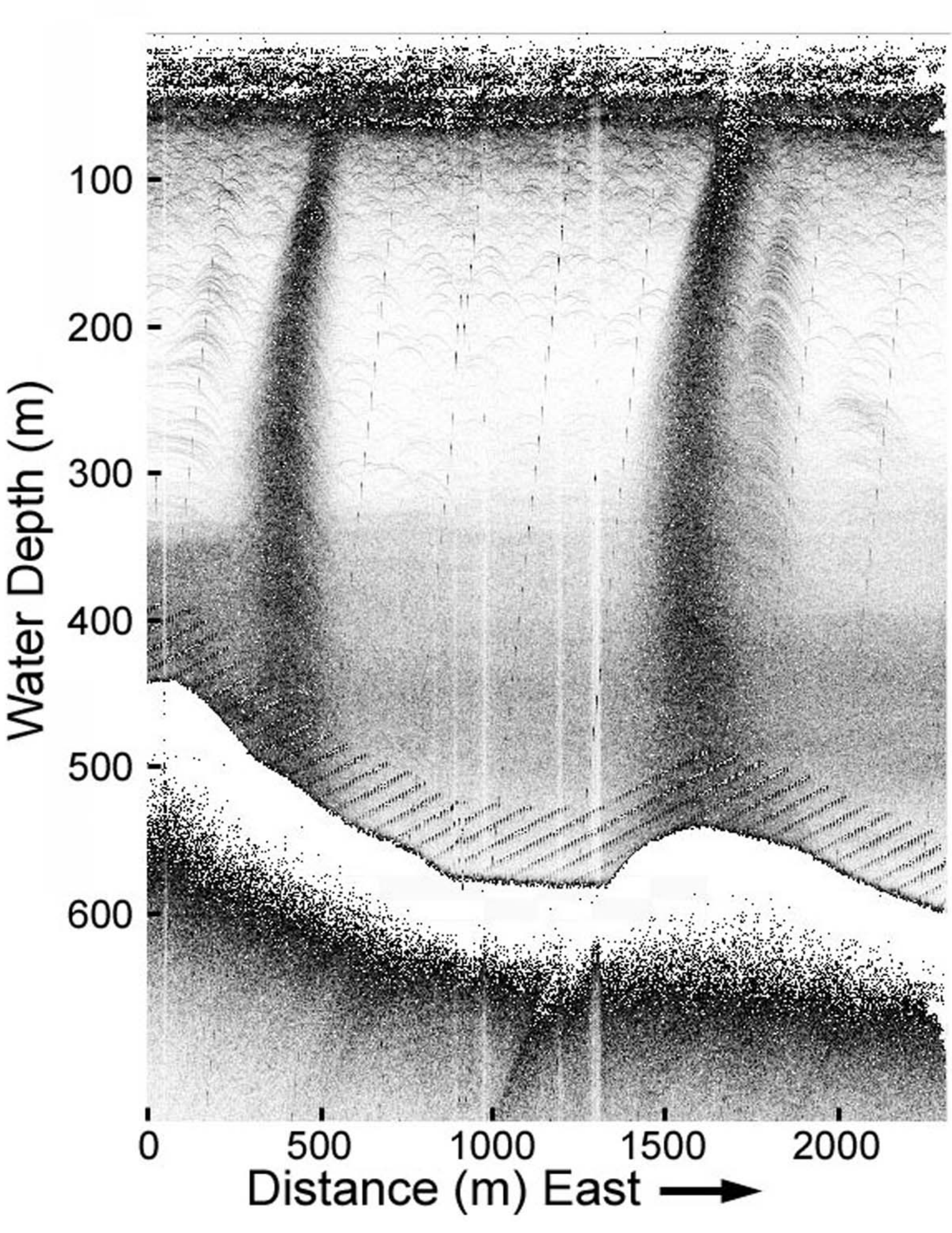

Fig. II-2. Acoustic survey transect of GC185, collected on July 11, 2001, showing two bubble streams about 1.2 km apart.

The bubble streams evident on the Chirp profiler and the Simrad echo sounder display were plotted according to the GPS location of the ship at the time the middle section of the bottom of the bubble streams were imaged (Fig. II-3). The bubble streams at GC234 and GB425 were more dispersed over the local seep area than the streams at GC185. We also detected several bubble streams about 4 km to the NW of the Brine Pool NR-1 in GC233 in 2001. These bubble streams were recognized as straight broad dark columns originating from a distinct origin on the seafloor, rising to the surface without being deflected in the water column.

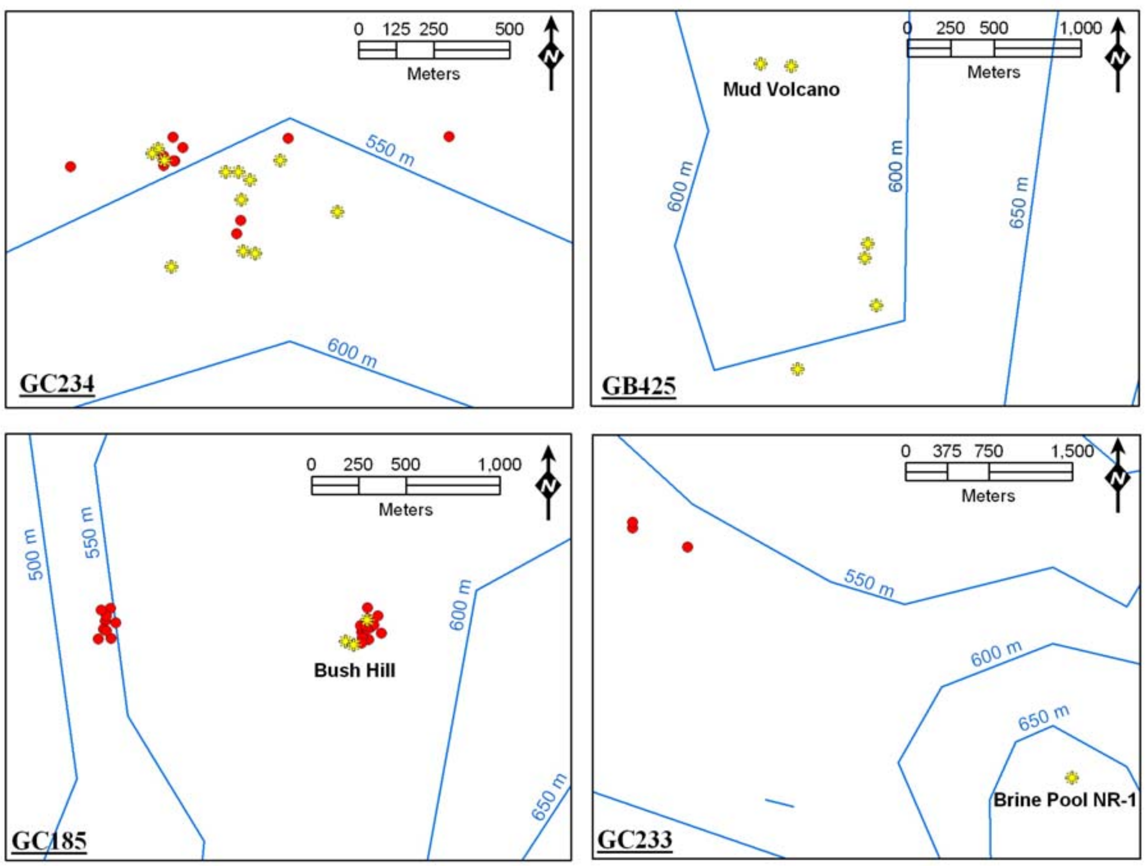

Fig. II-3. Locations of bubble streams evident in acoustic profile surveys of the chemosynthetic organism sites. The red dots are streams indicated on the 2001 surveys and the yellow stars represent streams imaged in 2002. The depth contours are 50 meters.

Side-scan sonar imaging of bubble streams

We were able to image several examples of gas bubbles rising from the seafloor with the side-scan sonar (Fig. II-4), but not all of the streams detected by the acoustic profilers were imaged with the side-scan sonar. The side-scan records portrayed the oily bubble streams as long, linear shadows perpendicular to the submersible track. In contrast, non-oily bubble streams appeared as areas of high backscatter, also perpendicular to the submersible track.

The sloping terrain at GC234 made it difficult to image bubble streams with side-scan sonar. In along-slope track-lines the two sides of the survey swath tended to intersect the bottom at very different angles. In cross-slope track-lines, it was difficult to maintain appropriate altitude. However, we were able to capture a large bubble stream in an area surrounded by thriving tubeworms and bacterial mats (Fig. II-4a). This bubble stream is evident as an acoustic shadow and its origin is surrounded by large areas of high backscatter, which are most likely produced by the tubeworms bushes, carbonate rocks but could also be produced by hydrate mounds. We noted many other features associated with hydrocarbons including pockmarks, ridges of carbonate rock, and meter-sized hummocks, all of which generated distinctive side-scan sonar signatures.

The topography of Bush Hill in GC185 made it relatively easier to maintain suitable altitude during the side-scan sonar surveys. We detected individual bubble streams at three separate locations. In several cases, we visually observed bubble streams at locations where they were subsequently detected by the side-scan sonar. At Bush Hill, the streams are evident as linear shadows with distinct origins (Fig. II-4b and II-4c). Active bubble streams in this area are well documented (MacDonald et al. 1994; Brooks et al. 1994; Roberts and Carney 1997; Sassen et al. 2001b; Leifer and MacDonald 2003). The points of origin were areas of markedly high backscatter, which could be mussel shells, mounds of gas hydrate, or the streams themselves. After rising about 6 meters from the seafloor, the bubble streams deflected northward (this is more noticeable in Fig. II-4c). This deflection was probably due to the current because the submersible also drifted to the northeast during the side-scan survey.

The inactive mud volcano at GC233 includes a large elliptical brine pool surrounded by mussels. This feature was very clearly imaged the side-scan sonar record (Fig. II-4d). The elongated areas of reduced backscatter on the mussel beds are the shadows of the markers located around the Brine Pool NR-1. The areas of high backscatter within the pool are areas from which bubble streams were seen on other dives (arrows in Fig. II-4d). However, we were unable to visually confirm gas venting during the side-scan survey.

The bubble stream at GB425 was imaged by the side-scan sonar and visually observed on several separate occasions during the dive. Clouds of sediment from the pool were entrained by the bubbles as they rose up from the mud vent but we did not see any associated oil seepage with this bubble stream. We also witnessed pulses of large non-oily bubbles episodically released from the central mud vent. These non-oily bubble streams are easily recognizable on the side-scan sonar records as high backscatter on both frequencies of the sonar (Fig. II-4e portrays the 384 kHz record). Both active and dormant mudflows were pervasive and easily recognizable on the side-scan sonar records.

Fig. II- 4. Side-scan sonar images of bubble streams with white 5-meter scale bars and black arrows indicating the direction of travel of the submersible. The direction of view of each of the images is perpendicular to the submersible. High backscatter is shown as light and low backscatter as dark. a. One of the low backscatter GC234 bubble streams; b. Three bubble streams northeast of Bush Hill mound depicted as low backscatter on the side-scan record with small white arrow indicating the bubble stream furthest to the right; c. One of the bubble streams at Bush Hill with the small white arrow pointing out the deflected top part of the bubble stream; d. The elliptical Brine Pool NR-1 at GC233 with small white arrows pointing to areas of high backscatter; e. Bubble stream at GB425 with small white arrow indicating one of the high backscatter bubble pulses.

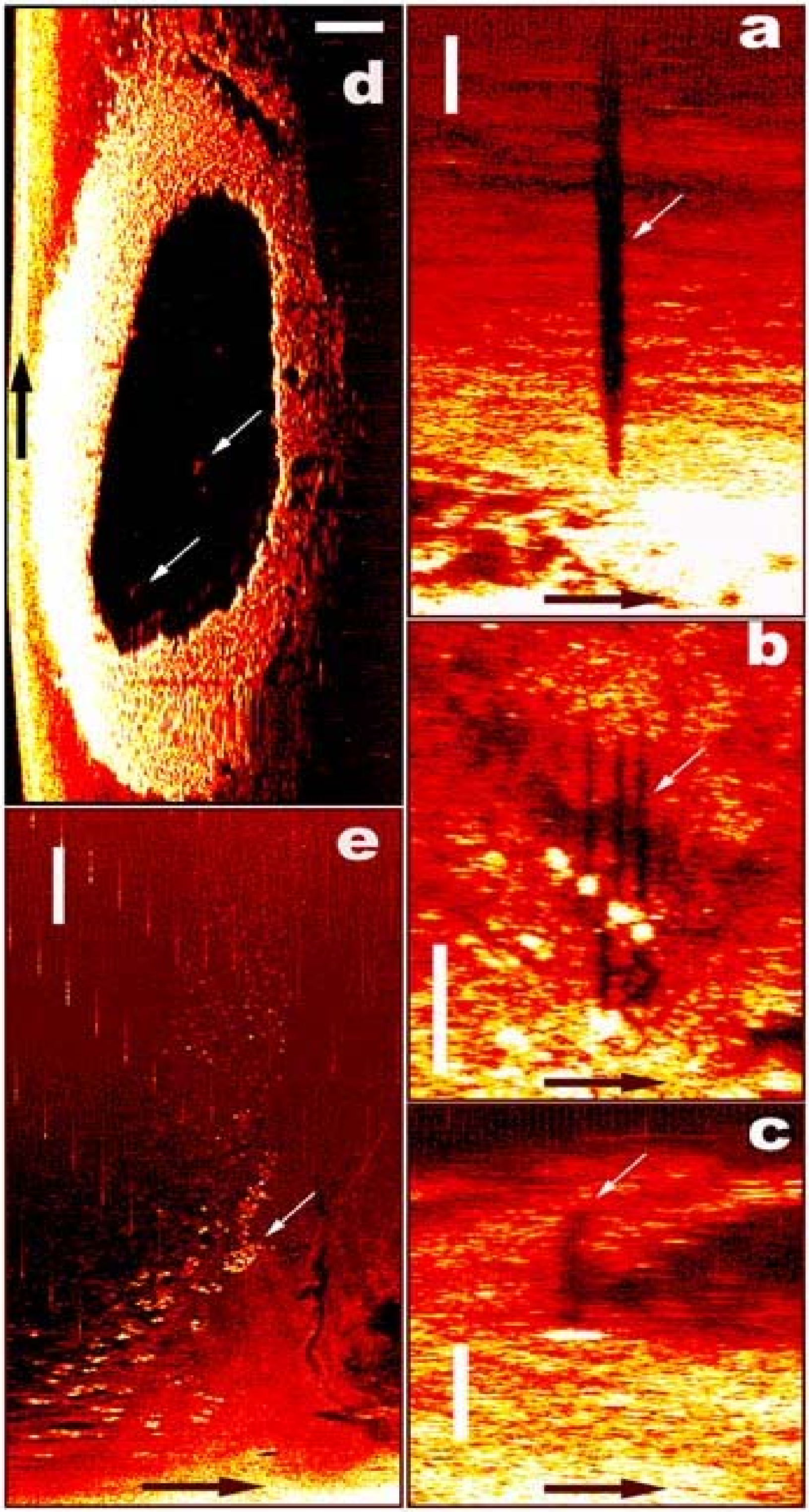
d
a
b
e
c

Detection of surface oil slicks by RADARSAT SAR

Distinct oil slick signatures were evident in all eleven RADARSAT SAR images. However, weather conditions clearly influenced the detection of slicks. Eight of the eleven satellite images included perennial slicks at Bush Hill in CG185, in the NW corner of GC233, and GC234 (Fig. II-5). However, no slicks were captured above the mud volcano sites, Brine Pool NR-1 at GC233 and GB425.

The morphology of these surface slicks is dependent on the surface wind and the currents. Figure II-5 depicts the traces of surface slicks whose direction of flow is influenced by different meteorological conditions on various days. On July 4, 2002, the slick at Bush Hill was located in a shear zone at the edge of a warm core eddy, which caused it to extend in two directions from the source of the seepage. We were unable to detect slicks above GC234 on June 17, 2002 and July 4, 2002 due to interference from rain cells. Rain cells impact the ability to detect slicks because rain cells, like slicks, can reduce backscatter from the sea surface. The sea surface can also be roughened by associated wind gusts and obscure the slicks (Melsheimer et al. 2001).

We manually traced the outlines of the slicks and calculated their areas. Table II-3 indicates the square kilometer area of the slicks at each of the respective sites based on the date the SAR images were taken. The number of origins detected by the SAR images differs between the three sites. The slicks above Bush Hill in GC185 all have one origin, but there are at least two distinct origins in the slicks above the NW corner of GC233 and four origins in most of the slicks above GC234. When there were more origins, the total area of the slicks was larger. The seepage at GC234 produces slicks covering an average of 4.814 km^2 from four suspected origins, while we see an average of 3.568 km^2 at the NW corner of GC233 from two potential seeps, and only an average of 2.024 km^2 from the bubble streams at Bush Hill (Table II-3). The average standard deviation of the total slick areas is only 1.57 km^2.

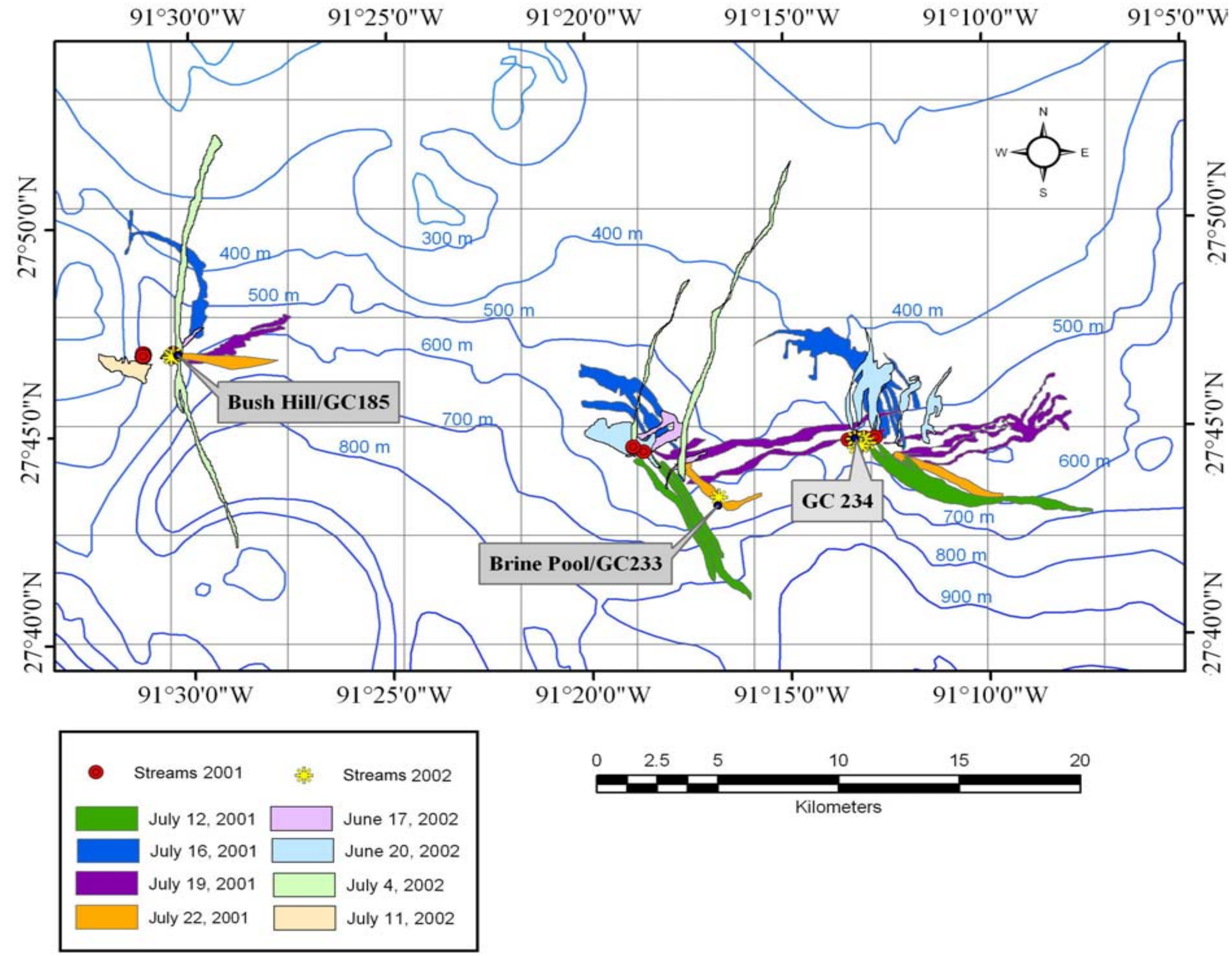

Fig. II-5. Traced oil slicks from natural seeps in MMS Lease Blocks GC 185, GC233, and GC234. The oil and gas streams detected by the acoustic profilers are noted in red (2001) and yellow (2002). The sites investigated by side-scan sonar surveys are the labeled blue dots.

Table II-3. Total area in square kilometers of the slicks at each site (separate slicks at the same site are added). Note that the slicks in GC233 are about 4 km to the NW of the Brine Pool NR-1 site (Fig. II-5). N/A means that the site was outside the perimeter of the image. "Sdev" stands for standard deviation of the average area of the slicks.

Site	7/12/01	7/16/01	7/19/01	7/22/01	6/17/02	6/20/02	7/4/02	7/11/02	Average	Sdev
GC185	N/A	2.501	1.897	1.513	0.468	N/A	4.461	1.303	2.024	1.251
GC233	4.861	4.994	5.464	1.277	2.329	2.634	3.417	no slicks	3.568	1.476
GC234	5.190	7.329	4.895	1.735	in rain cell	4.923	in rain cell	no slicks	4.814	1.987

DISCUSSION

We have integrated data from acoustic profiles, side-scan sonar and Synthetic Aperture Radar (SAR) images in order to document differences in seep signatures and constrain the regional quantification of seepage. The sea surface acoustic profiles detected bubble streams in the water column at all four study sites (Fig. II-3). There was an apparent discrepancy between the broad base of the streams imaged in the profile data and the narrow bubble streams observed from the submersible and imaged in the side-scan sonar. The broad base was most likely an artifact of the beam angle of the acoustic profilers, which would ensonify an increasingly large area with greater water depths. As was the case for side-scan sonar, the profile data exhibited distinct differences for oily and non-oily seeps. The oily bubble streams at Bush Hill, GC234 and the NW site of GC233 were easily recognized and reached the near surface. The non-oily bubble streams at the mud volcano GB425 and inactive mud volcano Brine Pool NR-1 were much less distinct and disappeared within 150 m above the bottom. There are two possible explanations for this. The oily coating of the bubbles from GC234 and Bush Hill may retard dissolution of gas and enhance transport of bubbles toward the surface (MacDonald et al. 2002). Additionally, recent evidence suggests that formation of a gas hydrate skin on the inside of bubbles might also retard bubble dissolution and enhance transport of bubbles toward the surface (Rehder et al. 2002). If this were the case, the relatively pure methane from Brine Pool NR-1 and GB425 would likely form structure I hydrate, which is known to reach its upper stability limits when water column temperatures exceeded about 7.5 °C (Sloan 1990). At GC234 and Bush Hill, the source gas includes higher molecular carbons and is known to form structure II hydrate, which has a significantly higher upper temperature limit. Inhibition of bubble dissolution due to gas hydrate coatings in the bubbles would therefore be restricted to greater depths at GB425 and Brine Pool NR-1.

Although side-scan sonar surveys with the submersible successfully imaged bubble streams at all four sites, not all of the active streams were imaged. However, we did observe two distinct side-scan signatures for gas venting: non-oily bubble streams produced high backscatter returns; oily bubble streams were imaged as acoustic shadows. By evaluating the signatures, we propose that side-scan sonar can differentiate oily bubble streams from non-oily bubble streams due to the difference in bubble size. Since oily bubbles are smaller than the non-oily bubbles, we hypothesize that the oily bubbles are below the resonance frequency of the side-scan sonar. At both Brine Pool NR-1 and GB425, the side-scan sonar records of the non-oily bubble streams are recognized as regions of high backscatter. The side-scan image from GB425 comprised a pronounced high-backscatter signature rising through the water column in which the pulses of the bubble stream are recognizable (Fig. II-4e). These bubbling pulses were confirmed by visualization from the submersible. No bubbles streams were recognized above the Brine Pool NR-1, but we did note areas of high backscatter from the middle and the side of the pool where bubble streams were sighted on other occasions (Fig. II-4d).

The oily bubble streams that we imaged at GC234 and Bush Hill were expressed in the side-scan sonar records as acoustic shadows. This potentially makes it difficult to differentiate them from shadows of topographic features, such as tubeworm bushes or carbonate rocks. However, the bubble streams were recognizable due to several attributes: First, the stream shapes were elongated with narrow origins and upper ends, whereas other shadows tend to have a broad base and narrow upper ends. Second, the upper ends of the streams were often deflected in the direction of prevailing currents. Finally, seafloor features were visible through the returns from the bubble streams, which indicates that sonar backscatter was reduced by the streams, but not blocked completely, as would often be the case for sonar shadows.

Our results indicate that the fine scale structure of the surfacing slicks as detected by RADARSAT SAR can be diagnostic of the number of sources contributing to the slick, depending on the distance between the sea-floor sources. At Bush Hill the bubble streams detected by the acoustic surveys are less than 200 meters apart and only one slick origin is recognizable in all of the SAR images. However, the sea-floor sources in the NW corner of GC233 and GC234 are over 200 meters apart and on numerous SAR images, there are distinguishable origins evident on the surface slicks. The acoustic survey indicated that the bubble streams were about 300 meters apart at GC234 and four slick origins are noted in the SAR imagery (Fig. II-6). The slicks with four origins, so from at least four sources over 200 meters apart, above GC234 cover about 2.5 times more area than the slicks with one origin at Bush Hill in GC185. This indicates that the average area covered by surface slicks can be indicative of the number of potential seep sources. So, the average area and the fine scale structure of the slicks can shed light on the number of potential sources at least 200 meters apart on the seafloor.

Bubble streams were imaged with the side-scan sonar and detected with the acoustic profiles at the mud volcano sites and yet no surface slicks were visible on the SAR images. This indicates that non-oily bubbles do not produce a sea surface slick. So, based on the integration of the acoustic profiles and side-scan sonar records with SAR surveys, we anticipate that any gulf-wide survey based solely on SAR will capture only a subset of the total quantity of venting gas. The visibility of slicks is strongly determined by surface meteorological conditions. Chapter III further investigates how many SAR images are required to detect seeps with reasonable certainty.

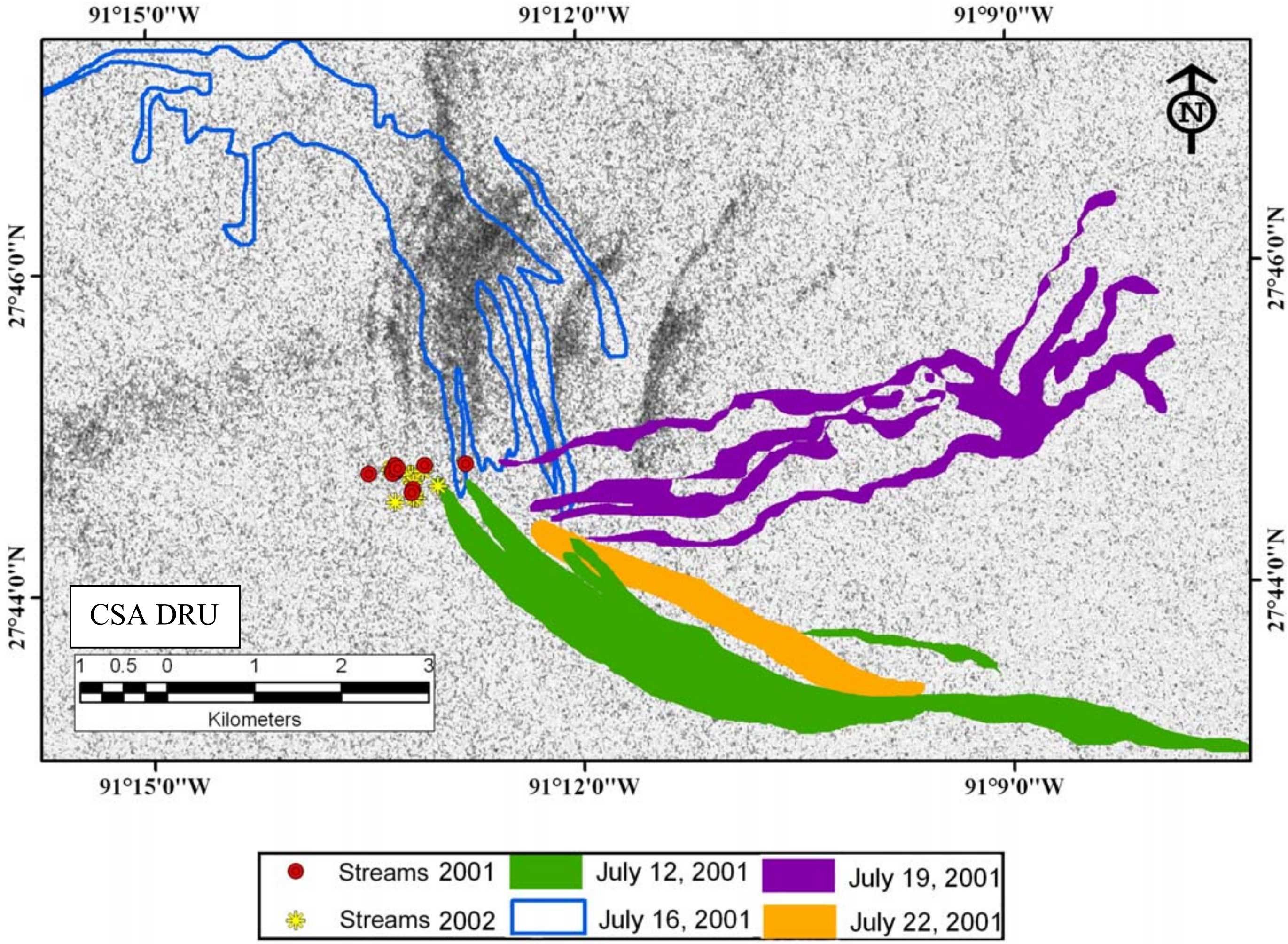

Fig. II-6. Detail of traced oil slicks above GC234 with locations of the bubble streams from acoustic profiles in 2001 (red) and 2002 (yellow). Background SAR image was taken by the Canadian Space Agency Data for Research Use and the dark gray areas represent oil slicks from June 20, 2002.

CHAPTER III

A SPATIAL ANALYSIS OF OIL AND GAS SEEPS ON THE NOTHERN CONTINENTAL SLOPE OF THE GULF OF MEXICO

INTRODUCTION

Synthetic Aperture Radar (SAR) is a proven tool used to verify the presence of oil slicks and other sea surfactants in a range of meteorological conditions (Espedal et al. 1996; Espedal 2001; MacDonald et al. 1993, 1996). Oil slicks drift under the influence of surface winds and currents from its origin or surfacing footprint, which is usually 1 km or less from its seafloor source (MacDonald et al. 2002). The natural slicks present a unique morphology that can be differentiated from anthropogenic spills or wakes and other natural occurrences, such as plankton blooms, rain cells, and variable surface wind stresses (Espedal 2001). Furthermore, regional perspective and temporal persistence can also be valuable factors to include when distinguishing signatures of slicks against other surface occurrences. Within 8 to 24 hours of surfacing, the oil evaporates, dissipates, disperses, and/or is consumed by sea surface bacteria (MacDonald et al 1993, 2002). However, the supply of oil can continually replace this slick, which varies in shape and size according to the dynamics of the wind and currents. Seeps that continually generate oily coated gas bubbles rising, at a speed of at ~15 cm/s, to the surface can produce perennial oil slicks (MacDonald et al. 1996, 2002). These surface expressions are observed in successive SAR images, permitting persistence and spatial analyses of the oil slicks and their sources.

Identifying the variability of the surface expressions of the slicks addresses the local and regional extents of the seeps' influence. Deciphering the persistence of a slick above a source provides information about the activity of the seep on the seafloor. Because the seep supplies carbon to benthic, water column, and surface bacteria, it will influence the local carbon cycle. The sea surface coverage of the slicks can be indicative of flux magnitude (MacDonald et al. 1993). As discussed in the previous chapter, inspecting the fine scale spatial distribution of the slicks on the surface can reveal the geometry of the sources on the bottom, which in turn can suggest the spatial extent of the influence of the seep on the benthos (MacDonald et al. 1989). Because not all slicks are produced by seeps that harbor a chemosynthetic community, further investigations of the sites at the seafloor are necessary (Reilly 1995). But a spatial analysis based on SAR imagery can reveal the potential regional distribution of chemosynthetic community sites. Furthermore, spatial analyses of slicks in SAR images reveals the charge, the extent of the source materials, and the extent of the migration from sub bottom offshore oil reserves (Behrens 1988). Seeps are usually not directly over commercially exploitable reserves (MacGregor 1993) but rather tend to be connected to reservoirs by a network of faults. Spatial and temporal analysis of seeps and seep sources continues a line of research that is important for petroleum geology and benthic ecology.

In this chapter, I will present the locations of seep sources on the seafloor by analyzing SAR images of the surface slicks covering the northern continental slope of the Gulf of Mexico. The SAR data were collected in month-long episodes during two consecutive summers in an area known to contain many seeps. A persistence analysis will be presented to show the consistency of slick formations above the source locations and to demonstrate the validity of using SAR for seep research. The resulting database of seep sources will corroborate the activity of known seeps and is an economical solution to identifying exploration sites for remotely operated vehicles (ROV's) or deep diving submersibles in search of new chemosynthetic communities. Geographical Information Systems (GIS) software is utilized to establish correlations between the sources, bathymetry, the slope of the bathymetry, and biological study sites. The reliability of the locations of the seep sources based on SAR is examined by plotting sources on side-scan sonar mosaics, which show geologic evidence of seepage in the Green Canyon lease area. Finally, a correlation between allochthonous salt structures of the continental slope and the seep source locations is evaluated to determine the relation of sub-bottom features and salt to the seeps. The lower slope is thought to support very few oil seeps relative to the upper slope due to the structure of the underlying allochthonous salt (Bryant, personal communication).

METHODS

SAR imaging

The RADARSAT satellite acquired 11 Synthetic Aperture Radar (SAR) images covering a total of 53, 693 km^2 on the northern continental slope of the Gulf of Mexico (Table III-1 and Fig. III-1). The images were collected during the summer months due to the probability of favorable wind conditions and the ability to visually verify some of the oil slicks during offshore research cruises. RADARSAT SAR images provide a rich set of information on oil slicks but also on other features such as current fronts, oil platforms, and ship locations. Oil slicks appear dark on SAR images because they reduce the backscatter by attenuating Bragg scattering from capillary and gravity waves imaged by the C-band radar on the SAR RADARSAT satellite (e.g. Fig. III-2). Current fronts are easily distinguishable due to the dichotomy in the backscatter (Fig. III-2). Oil platforms (e.g. Fig. III-3) and ship locations are shown as high backscatter and moving ships can be differentiated from the platforms by their wake (e.g. Fig. III-4).

Table III-1. Details of Synthetic Aperture Radar (SAR) images collected with RADARSAT over the northern continental slope of the Gulf of Mexico with MMS lease area covered. The Lease areas are: GB, Garden Banks; GC, Green Canyon; WR, Walker Ridge. The covered area refers to at least 25% coverage of that lease block by the image, so only a few blocks of Keathley Canyon and Ewing Bank were covered by some of the images. The SAR wide 1 and 2 settings have swath widths of 160 km and 150 km, respectively, compared to the SAR Standard, which has a swath width of 100 km.

Date	**UTC**	**Beam Mode**	**Scene ID**	**Orbit**	**Incidence Angle**	**Resolution**	**Lease area covered**
7/9/2001	12:12	Wide2	M029640	Descending	30.8º - 39.5º	~27 m	GB, GC
7/12/2001	0:05	Wide2	M0255277	Ascending	30.8º - 39.5º	~27 m	GC
7/16/2001	12:08	Wide1	M0256031	Descending	20.0º- 31.2º	~35 m	GC, WR
7/19/2001	0:01	Wide1	M0256193	Ascending	20.0º- 31.2º	~35 m	GC, WR
7/22/2001	0:13	Standard 6	M0256417	Ascending	41.4º- 46.5º	~25 m	GC
6/10/2002	12:12	Wide1	M0285291	Descending	20.0º- 31.2º	~35 m	GB, GC
6/17/2002	12:08	Wide1	M0285867	Descending	20.0º- 31.2º	~35 m	GC, WR
6/20/2002	0:01	Standard 2	M0291469	Ascending	24.2º- 31.2º	~25 m	GC
7/4/2002	12:12	Wide1	M0288984	Descending	20.0º- 31.2º	~35 m	GB, GC
7/11/2002	12:08	Wide1	C0023362	Descending	20.0º- 31.2º	~35 m	GC, WR
7/14/2002	0:01	Standard 2	M0289262	Ascending	24.2º- 31.2º	~25 m	GC

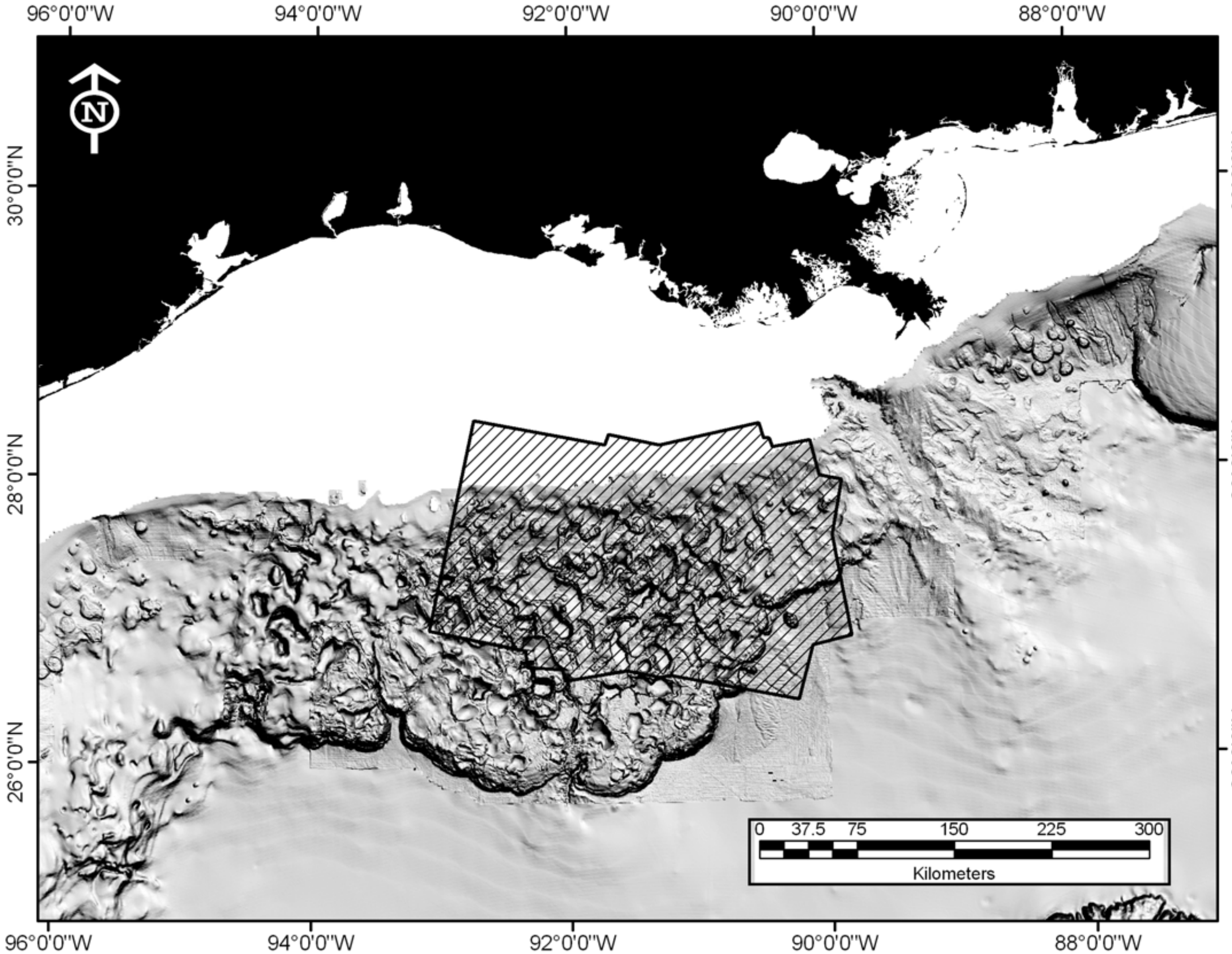

Fig. III-1. Area encompassed by 11 SAR images taken in the summers of 2001 and 2002. It covers a total of 53, 693 km^2. The black outlines show the combined boundaries of the 11 images.

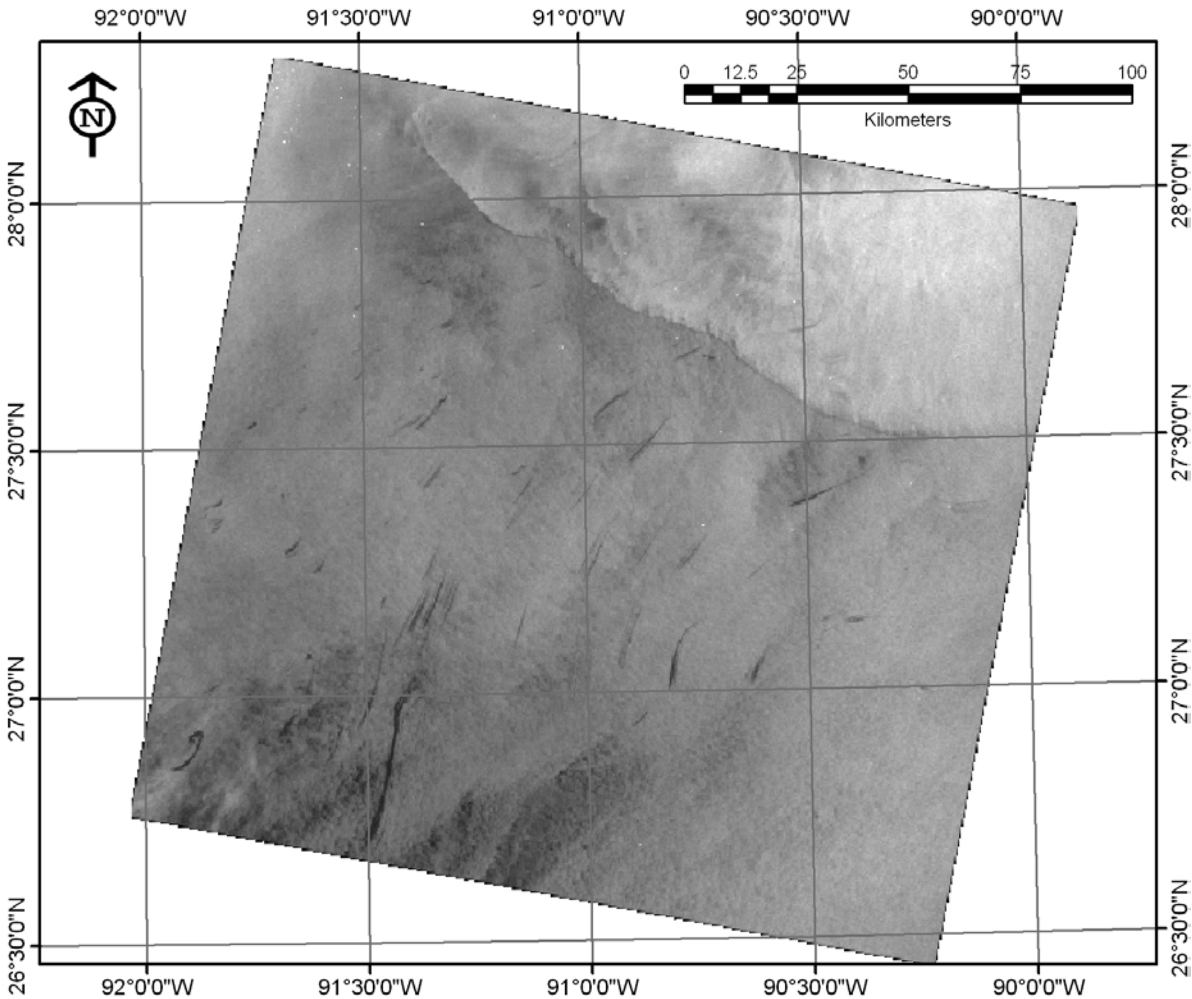

Fig. III-2. Synthetic Aperture Radar (SAR) image from June 17, 2002 (CSA DRU). The natural oil slicks are evident as black streaks and are predominantly in the middle of the image. There is a large current front visible in the NE part of the image and rain and wind cells in SW part of the image.

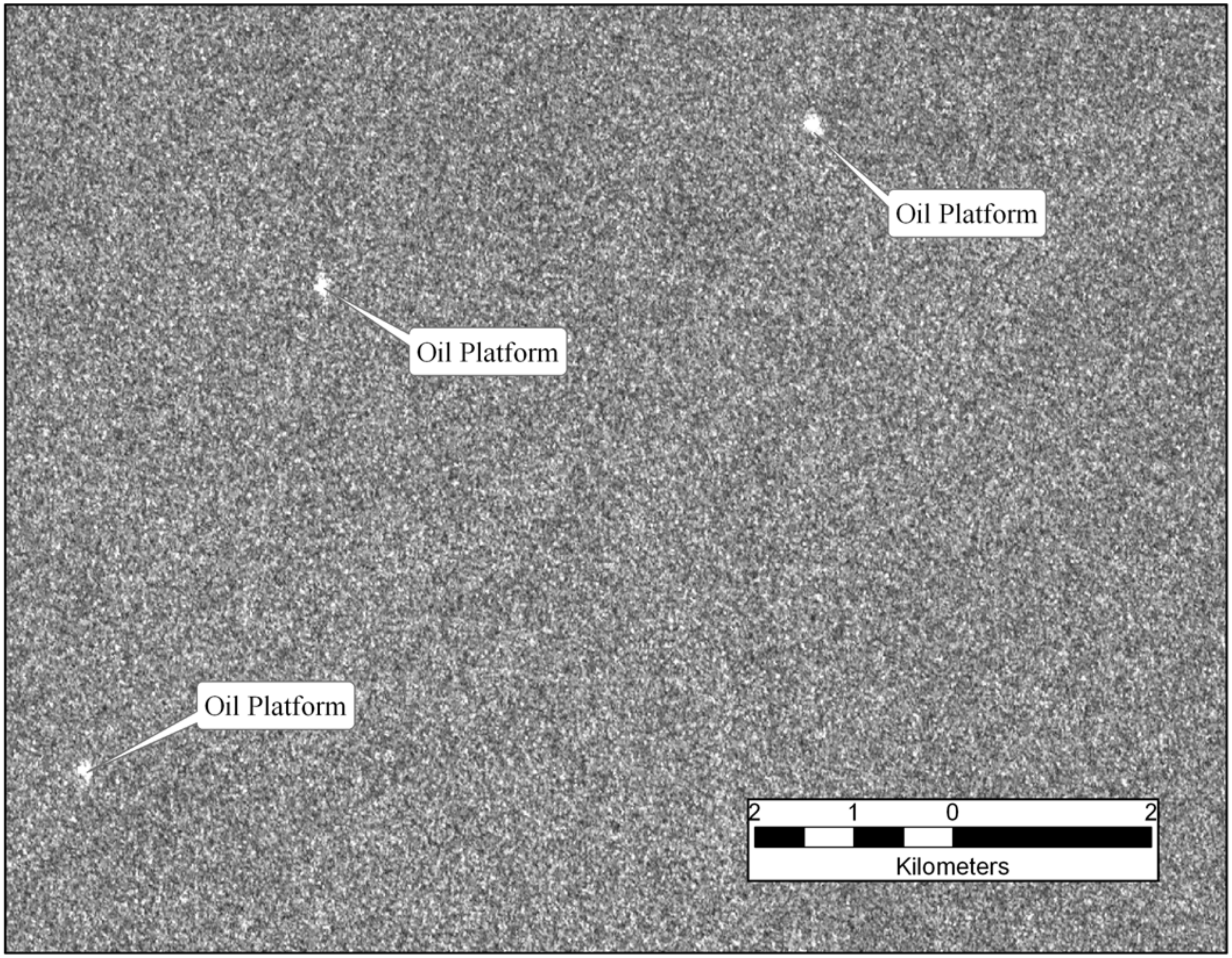

Fig. III-3. Three oil platforms evident as high backscatter on a SAR image (CSA DRU).

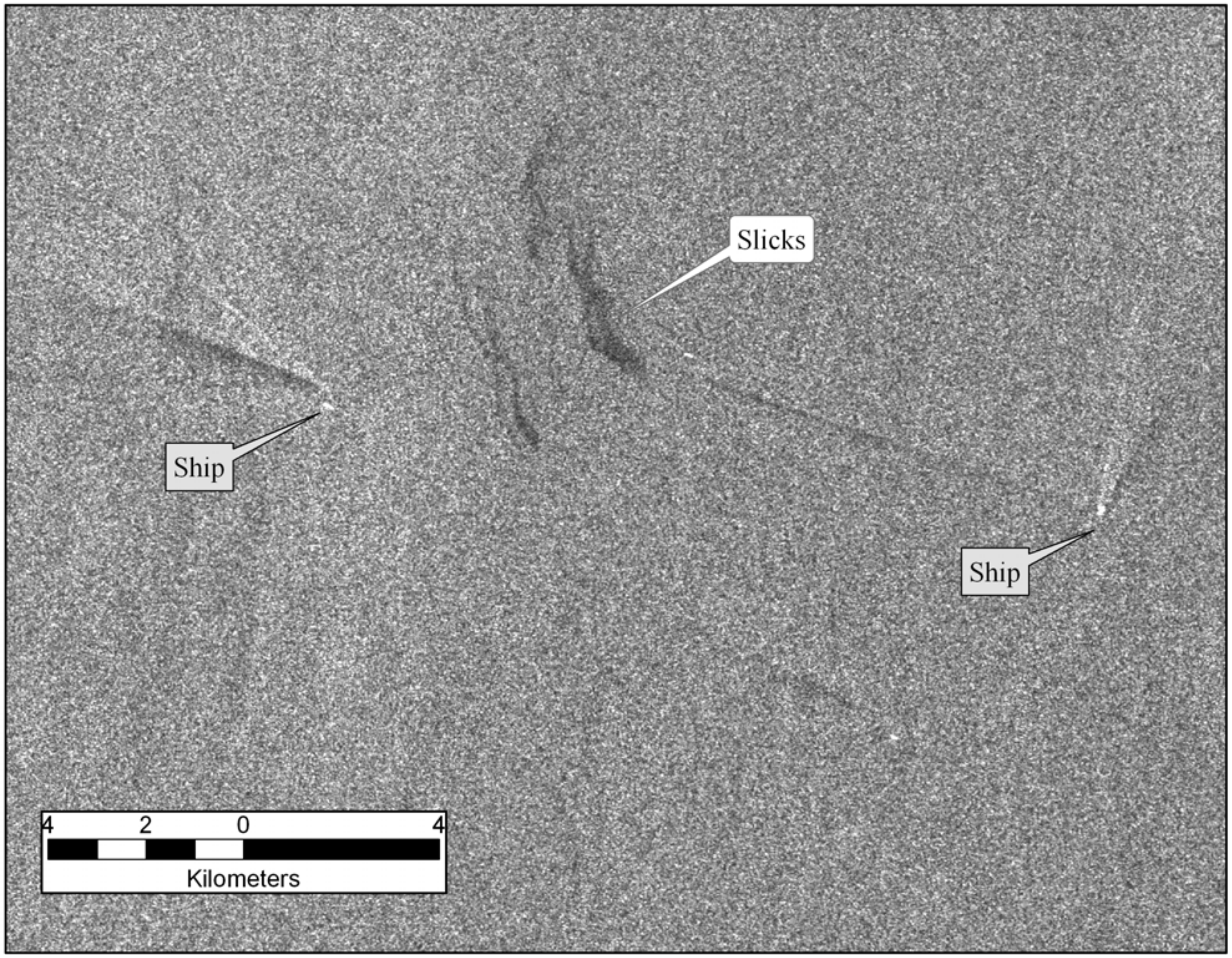

Fig. III-4. Two ships and their wakes on a SAR image (CSA DRU). Natural oil slicks are also evident in the upper middle part of this close-up.

Wind and current data

Wind information was made available by the Ocean Monitoring Workstation (OMW) from the Canadian Ice Service and SeaWinds from NASA. The OMW was developed to quickly extract information, such as winds and oil slicks, from RADARSAT images by using different algorithms (Henschel et al. 1997). The Canadian Ice Service processed SAR images taken in 2002 through a wind algorithm at a grid spacing of 10 km. The wind data has an 180º ambiguity and contains minimum and maximum wind speeds. However, if there was a lack of linear ocean features, the wind speed could be determined but the wind direction could not be calculated. Near-surface wind speed and direction can also be calculated by a scatterometer, which is provided by SeaWinds from NASA's QuickSCAT. Wind information from the covered area was applied to each of the SAR images not put through the OMW wind algorithm.

Current and sea surface temperature data were acquired from the Colorado Center for Astrodynamics Research's Gulf of Mexico Near Real-Time Altimeter Data Geostrophic Velocity Viewer. This data was useful in determining spatial and temporal anomalies as noted in Chapter II for the explanation of the morphology of the slick at Bush Hill on July 4, 2002.

Geographical Information Systems (GIS) procedures

The SAR images were georeferenced, which means they were positioned in real world map coordinates. First, a utility in ERMapper provided the means for importing SAR images without specifying a geodetic datum or map projection. Then the geocoding wizard in ESRI ArcMap was used to perform a polynomial transformation, specify the datum as World Geodetic System (WGS) 84, and project the image in Universal Transverse Mercator (UTM) 15 North. The polynomial transformations were based on the known corner points for each image and Minerals Management Services platform locations. The oil platforms were primarily located in the northern parts of the images and so the only rectification points used in the southern parts of the images were the corner locations of the image. The RMS of the georectified images averaged 50 m. The images were then combined in an ESRI ArcMap project along with MMS Lease Blocks and the bathymetry of the Gulf of Mexico. All of the slicks in each image were manually traced and saved as unique GIS shape files in order to overlay the slicks from different days. The manual tracing required recognizing the characteristic morphology of the surface expressions and comparing the slicks in the same image for similar directions of surface drift. If a surface signature was questioned, slicks present in the same location on one or more of the SAR images could corroborate that it was indeed a slick. The origin of each slick was estimated based on visual interpretation of slick morphology consistent with previous research.

Previous authors have suggested that appearance of a slick in the same locality distinguishes a true oil slick from other SAR targets. In this study, because of overlap of the SAR images, it was possible for a seep to produce a slick in up to 11 images. When there were multiple detections of a seep, the slick origins in each image could be used to estimate the seafloor location of the source based on the average x and y locations of the origins of the slicks. The origins of the slicks could to be separated by less than two kilometers in order to be included in the estimation of the seep source. In deeper waters, more than 1000 m in depth, it was more difficult to pinpoint the separate sources based on the fine scale structure of the slick because the origins of the slicks were further apart. Therefore, it was necessary to indicate the number of possible sources suggested by the most common number of origins detected on different days. This number of possible sources ranged from two to six possible sources on the seafloor.

A table was constructed with each source location including the MMS lease block, location, depth, seep source number (1 through 6), and the number of origins used to estimate the source location (Appendix A). Then a Visual Basics for Applications (VBA) statement was used to calculate the area of each of the traced slicks. The average area covered by a slick from a single source serves as the basis of annual carbon flux from the seep to the sea surface. A table detailing the temporal persistence of the traced slicks in the 11 SAR images was also compiled (Appendix B). This table also details which seep source locations were covered by each image and the estimated depth of the sources.

Statistics

In order to correlate the depth to the total number of sources at that depth, Pearson's product-moment correlation, a parametric test, was used. To apply this test, the data must satisfy two assumptions: they must be bivariate observations and have a normal distribution. The data are paired and normality was verified with a Kolmogorov-Smirnov test. A statistical estimation was used to determine the sample size necessary to calculate a sample mean with a specified level of precision. The equation is (Eckblad 1991):

$$\text{Sample size} \approx \frac{(\text{t-value})^2\ (\text{sample variance})}{(\text{accuracy} * \text{sample mean})^2}$$

The sample mean and variance included in the equation are based on the results of the SAR images analyzed in this thesis. The t-value, 1.812, was based on the two-tailed value with 10 degrees of freedom in the student's t-distribution chart.

Comparison to existing geologic data

Three geologic data sets were available: continental slope bathymetry (Liu and Bryant 1999), salt structure (Watkins et al. 1996) and side-scan sonar mosaics (Sager 2002). A slope analysis of the bathymetry dataset was completed in ESRI's Spatial Analyst. The seep source locations and the geologic data were merged into GIS projects in order to determine the relationships. In case of the bathymetry data set, the depth, the slope, and the seep sources topographical correlations were documented.

The sonar mosaics of the shallow and deep areas of Green Canyon by the TAMU^2 side-scan sonar were incorporated in this thesis to correlate the SAR identified slick sources with the seafloor features identified in the side-scan data. The final mosaics have a resolution of four meters per pixel and the dark shades indicate areas of high acoustic backscatter (sonar bright) whereas the lighter shades represent low backscatter (sonar dim). The seafloor features on the mosaic were interpreted by comparing them to the 3.5 kHz sub bottom profiles, which helped particularly in fault identification. Sager's (2002) study also indicated that the wipeout zones on the 3.5 kHz echo-sounder profiles correlated to the high backscatter areas, which implies that gas was likely present in those areas. He also found that seeps were more distinguishable in the shallow mosaic than in the deep mosaic. In the deep mosaic, it was difficult to differentiate the signatures of the seeps from the similar signatures of numerous disturbances from mass wasting. The seep sources and the side-scan mosaics were merged in one GIS project to test the reliability of the method used to identify seep source seafloor locations from the average x and y of the origins of the surface slicks captured by SAR.

A point comparison of the seep source locations to the structure of the allochthonous salt layer was completed to determine if there was a relationship between the depths of the salt and seep source locations. The allochthonous salt map showing the structural framework of the Northern Gulf of Mexico is an integration of 2-D seismic data, paleo, and/or well logs (Watkins et al. 1996). The upper and lower continental slope salt is indicated as less than 1 sec to over 4 sec or no salt. The time represents 2-way travel time, so at 1 sec, the salt is less than 750 m below the seafloor. The salt on the lower slope is shallower than the salt on the upper slope (Fig. I-1). The area of the salt structure map delineated by processed SAR imagery was scanned and the seep sources were manually located on the map according to latitude and longitude. The slope (in degrees) and related salt structure of each of the source locations were added to Appendix A.

RESULTS

The manual tracing of slicks in each of the 11 SAR images resulted in 11 separate vector shape files. Only one identifiable slick was present in the image taken on July 9, 2001 due to the weather disturbances covering the image. However, all of the other images included many more identifiable slicks that were traced. Table III-2 lists the number of traced slicks and a description of the morphology and direction of flow for the majority of the oil slicks captured by the SAR image. The different morphological features and direction of flow on the surface are due to the meteorological conditions on different days. It is important to note that in Table III-2 not every traced slick pinpoints an individual source; e.g. the 174 slicks from July 4 do not target 174 sources.

Table III-2. Description of slicks seen in each of the 11 SAR images taken in 2001 and 2002. The "Number of slicks" represent the total number of slicks that were manually traced in the image.

Date	**Number of slicks**	**Description of Slicks and Features in SAR image**
7/9/2001	1	Swirl-like slicks; many rain cells obscure the slicks in the image
7/12/2001	139	Long linear slicks flowing to the SE from sources; most have hook to E on end
7/16/2001	147	Curved slicks flowing to the NW from the sources
7/19/2001	105	Great variety in meteorological conditions evident in slick morphologies
7/22/2001	52	Short linear slicks flowing to the SSE from the sources
6/10/2002	15	Short linear slicks flowing to the NW from the sources
6/17/2002	115	Medium linear slicks flowing to the NNE from the sources (Fig. III-2)
6/20/2002	71	Long linear slicks in S part of image and wider short slicks in N all flowing to the NNE from the sources
7/4/2002	174	Long curved slicks in E part of image and shorter slicks in middle part of image under different conditions
7/11/2002	59	Short wide slicks flowing to the SE from the sources
7/14/2002	46	Medium linear slicks flowing to the E from the sources

The traced slicks were incorporated into one GIS project in order to identify the source locations. The origins of each of the slicks were identified and the source locations represent the average x and y of the origins of the slicks of that source (Appendix A). Some of the source locations were easy to identify, for example, the one source in MMS Lease Block GC232 (Fig. III-5 and Fig. III-6). Six individually traced slicks from different days neatly pinpoint the source location in GC232 but the slick from July 4, 2002 is offset 2 km to the northwest, so it was not included in the average x and y calculation. Most of the July 4th slicks that were correlated to a source displayed this offset. Where there was more than one distinct origin in at least two of the slicks, the separation of individual sources could be more challenging, e.g. the traced slicks in MMS Lease Block 539 (Fig. III-5 and Fig. III-7). In these cases individual sources could not be reliably located based on the fine scale structure of the slicks and the total number of sources are represented by unique symbols located in the average x and y position of all of the contributing origins. There were other locations where the individual sources were juxtaposed, but the individual locations of those sources could be deciphered, e.g. in GC415 and GC416 (Fig. III-5 and Fig. III-8).

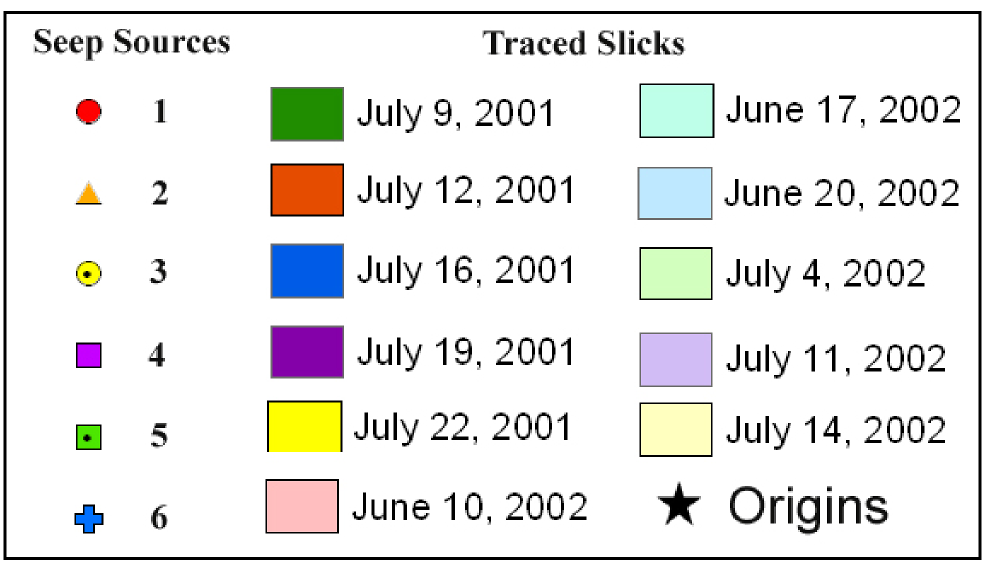

Fig. III-5. Legend of manually traced slicks, the origins of the slicks, and number of possible seep sources per location for figures III-6 through III-8.

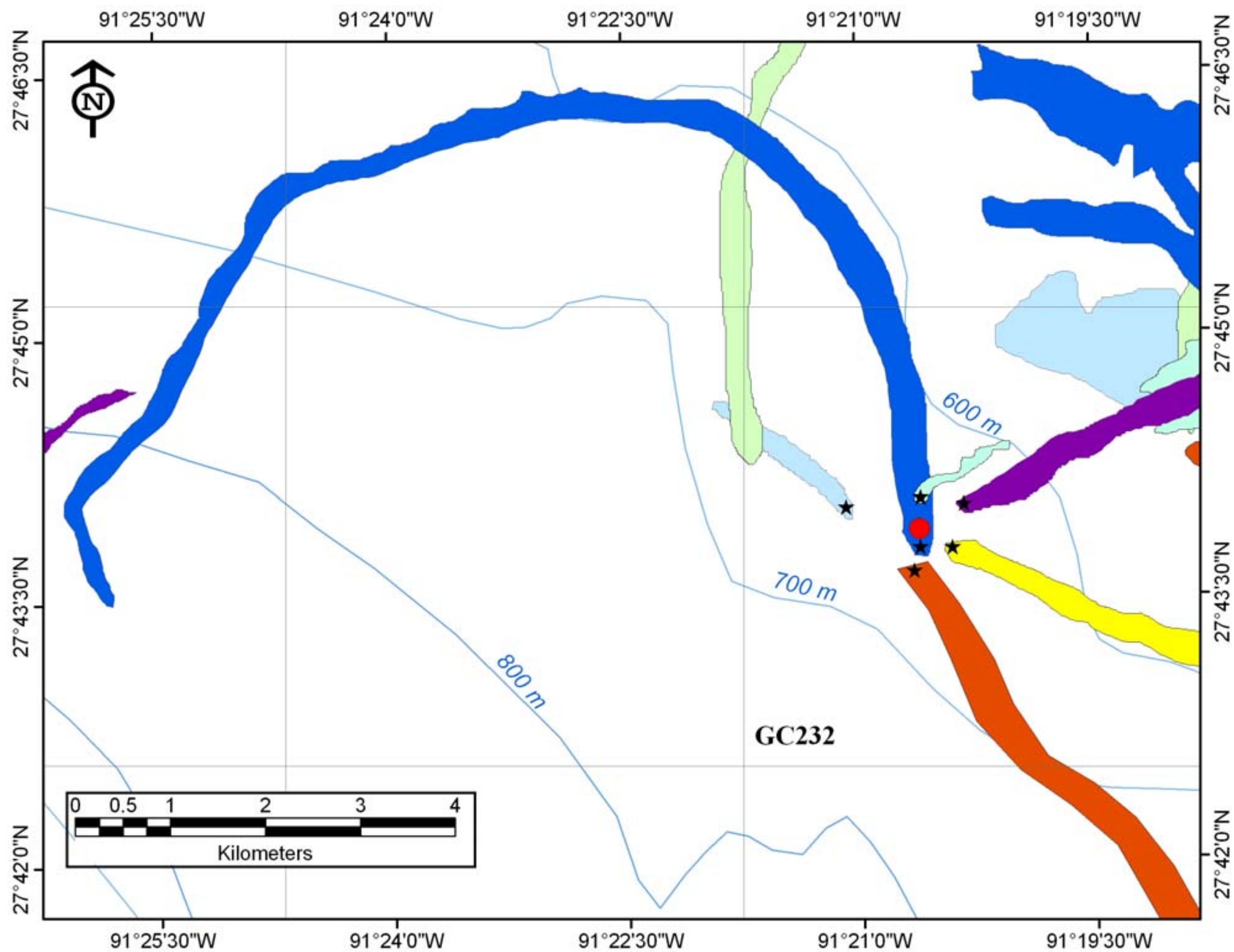

Fig. III-6. Example using the origins of manually traced slicks to find a seep source location in MMS Lease Block GC232.

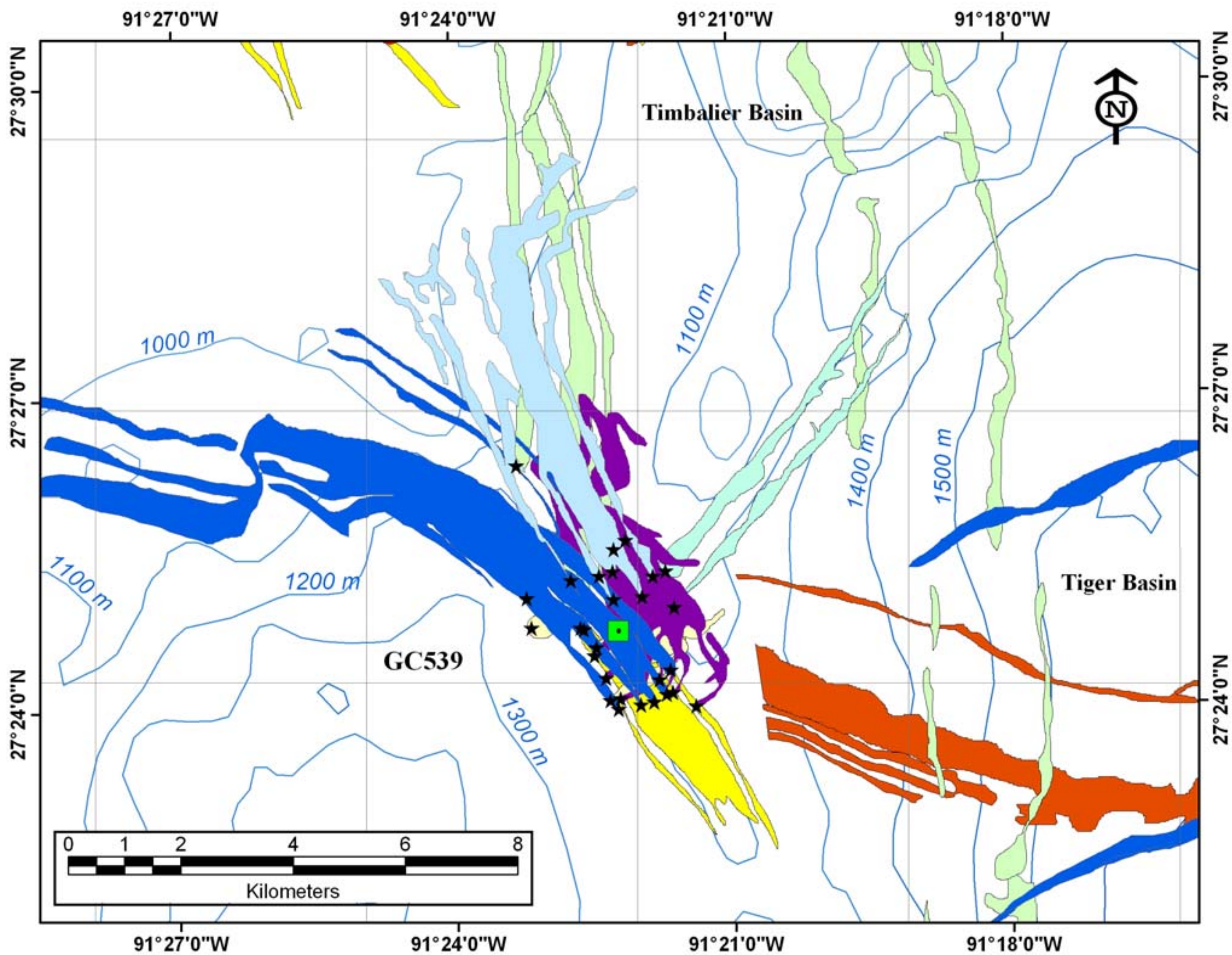

Fig III-7. Manually traced slicks and estimated location of five potential sources located in MMS Lease Block GC539. The slicks from July 12, 2001, symbolized in red, are cut off because they were at the edge of the SAR

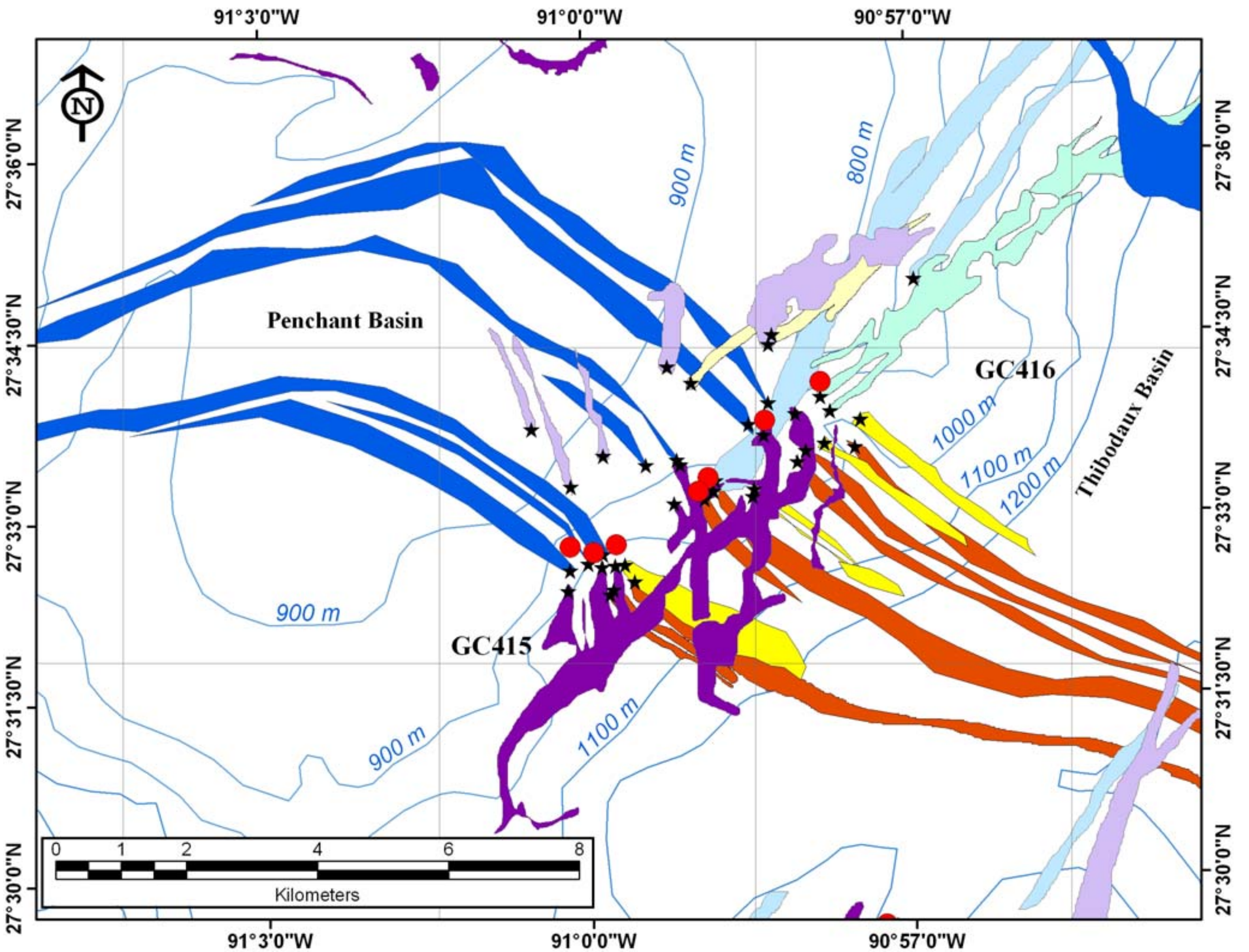

Fig III-8. Manually traced slicks and calculated seep source locations in MMS Lease blocks GC415 and GC416.

Working with these limitations, a total of 113 potential seep source locations was identified in the 53,693-km^2 area covered by the SAR images. These 113 locations were plotted on a topography map of the Gulf of Mexico slope (Fig. III-9). By analyzing the fine scale structure of the slicks, a single source could be differentiated from multiple seafloor seep sources and this is indicated by "number of sources" in Appendix A. The 113 locations symbolize a potential of 175 seeps. It is evident that more single sources were identified on the upper slope, which is shallower. Water column currents in the deeper waters (>1000 m) influence the surfacing perimeter and prevent the identification of individual origins due to large offsets in the slick origins on the sea surface.

The locations of the seep sources were correlated with the topography of the continental slope. Figure III-9 shows that none of the sources are located in the bottom of the basins but rather tend to be related to the sides or flanks of features, such as mounds and basins evident in the topography map. This relationship was further analyzed with the slope analysis described below. The total number of seep sources versus depth is shown in Figure III-10. The seeps ranged in depth from 100 to 2000 meters. Seventy nine percent of seeps are found on the 900 m isobaths or deeper. Pearson's product-moment correlation analysis did not indicate a significant association between depth and total number sources ($r = 0.348$, d.f. = 27, $p > 0.05$).

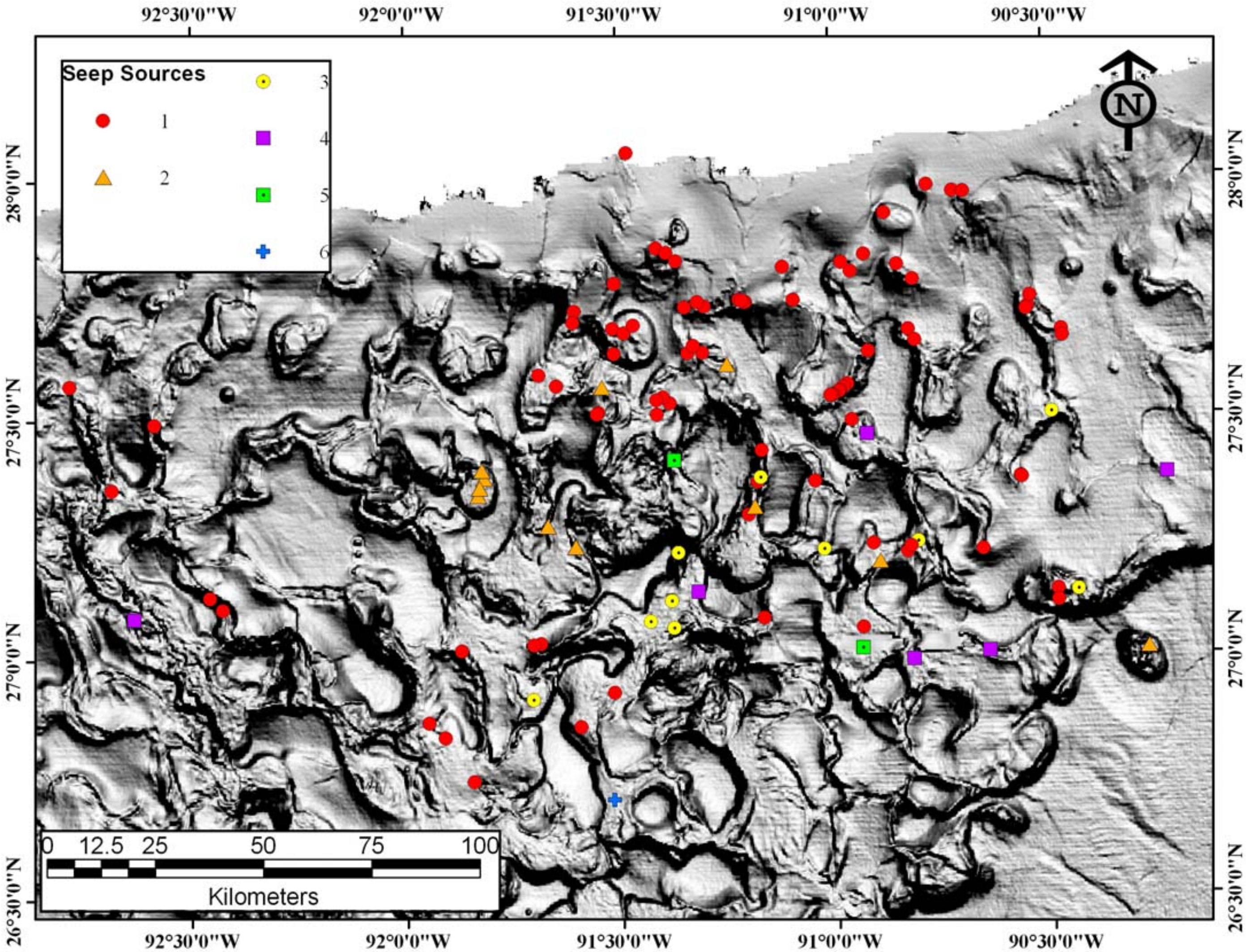

Fig. III-9. Seep sources located on the bathymetry map (Liu and Bryant 1999) of the continental slope of the northern Gulf of Mexico. The legend refers to the number of potential sources in that area.

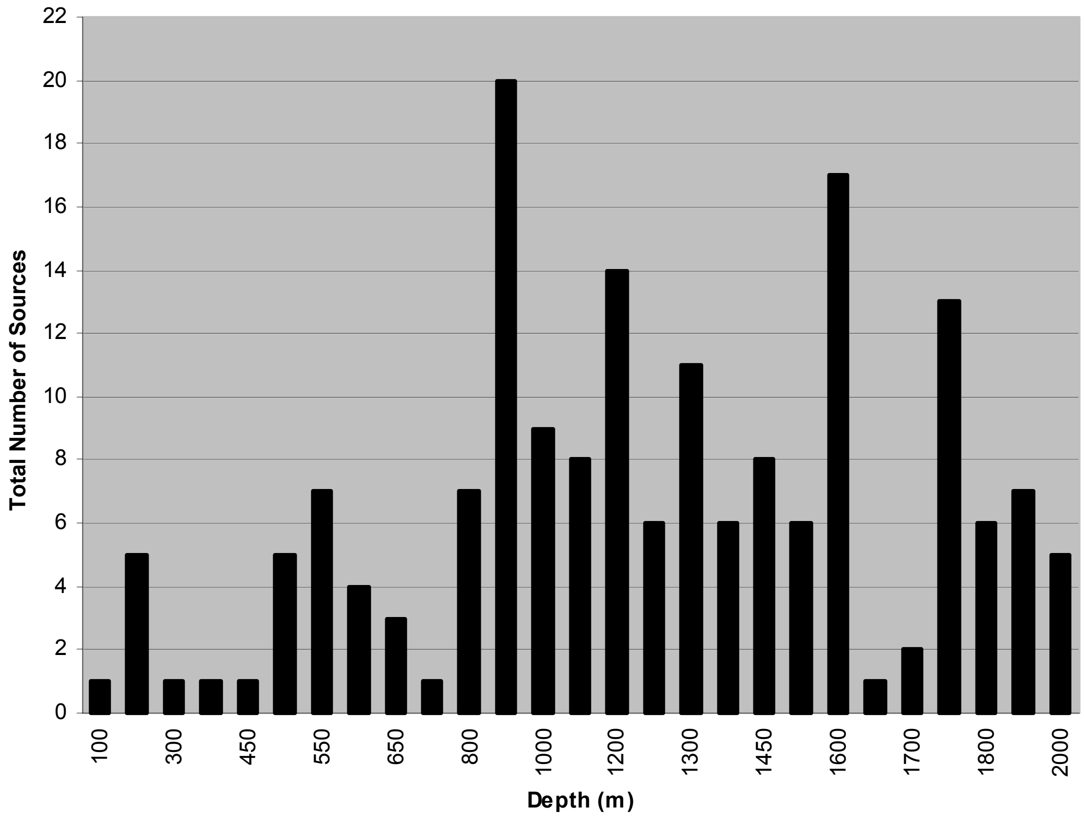

Fig. III-10. Graph of total number of seep sources versus depth.

Persistence analysis

Appendix B provides the basis of the completed persistence analysis of the surface slicks. In 2002 only seven of the 107 seep locations found the previous year were not corroborated, so 93.5% of seeps produced slicks captured in the 2002 images. In 2002 two of the SAR images covered the eastern Garden Banks lease blocks (Table III-1) and six more seep sources were added to the 2001 list, culminating to a total of 113 seep source locations. The percentage of slicks captured out of the total possible (those not outside of the perimeter of the image) was calculated to examine the persistence of the surface expressions (Appendix B). This percentage was also related to the depth of the seeps and there is no relationship between the depth of the sources and the percentage of surface expressions for either 2001 or 2002 (Fig. III-11). The ability of seeps to display surface expressions is thus not dependent on depth.

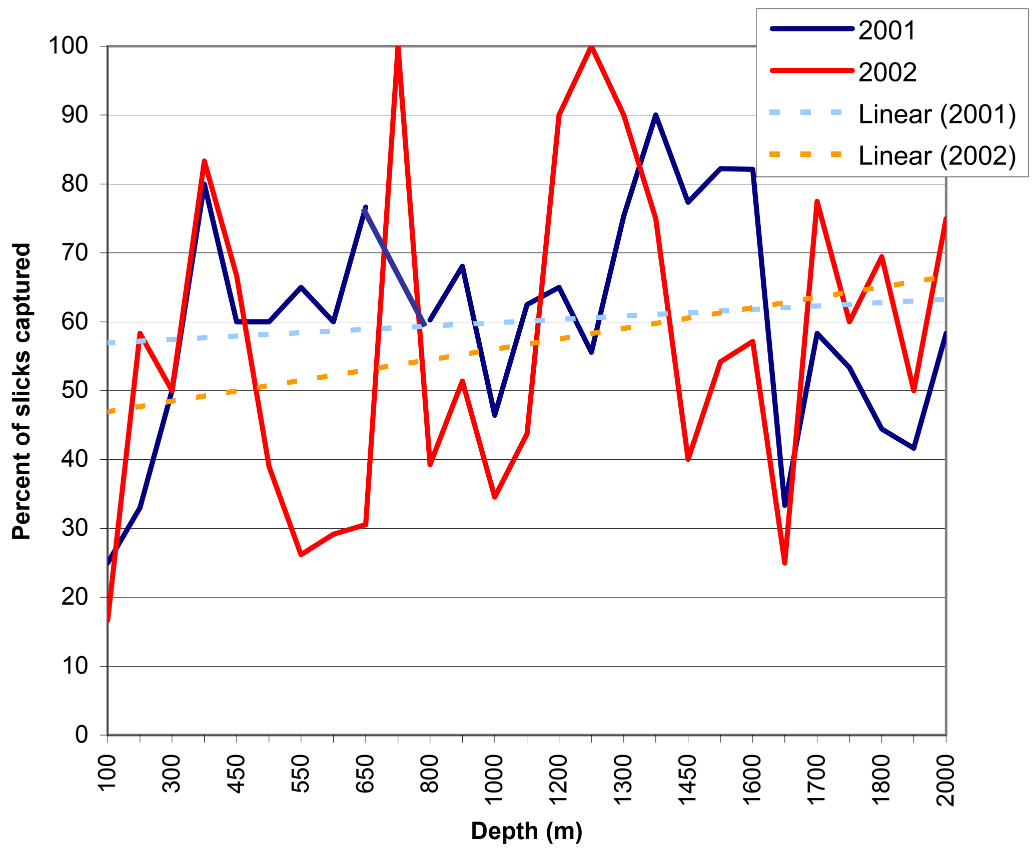

Fig.III-11. Average percent of captured slicks by SAR images from both 2001 and 2002 versus depth. Linear regression lines were added to verify that there is no relationship between the depth of a seep and the surface expression for either year. The r^2 for 2001 is 0.0142 and for 2002, $r^2 = 0.0641$.

Table III-3. Total number of source locations covered by SAR images defined by the date the images were taken. "Percent Identified" refers to the percentage of sources that were identified in the SAR image out of the total number of sources encompassed by the image.

Date	Total Number	Percent Identified
7/9/2001	61	2
7/12/2001	68	94
7/16/2001	106	84
7/19/2001	107	63
7/22/2001	68	53
6/10/2002	68	18
6/17/2002	107	57
6/20/2002	70	64
7/4/2002	66	61
7/11/2002	107	49
7/14/2002	71	41

Table III-3 sums up the results from Appendix B for each SAR image. First, the total number of seep sources covered by each image was determined. Second, the percent of sources identified in each individual image was calculated. As noted above, only one slick was clearly defined on July 9, 2001, but the image encompassed 61 seep locations so it portrays the lowest percentage of slicks identified in an image. If this image is considered an outlier, the average percent of sources identified for the other ten images is 58%. The most successful image was the one taken on July 12, 2001, as 94% of the seeps encompassed by the image produced slicks captured on that day. On July 12, 2003, there were no weather disturbances in the area covered and the slicks were all very dark, easily distinguishable features.

In order to determine the approximate accuracy of the mean estimate within a 90 % confidence interval, Eckblad's (1991) sample size equation was used. Based on the 11 images in Table III-3, the average number of sources encompassed by the images is 82 seep locations with a variance of 400. Appendix C illustrates the sample size versus the accuracy curve. Appendix C also shows that we can be 90% sure that the sample mean of 82 seep locations indicated in the SAR images is within $\pm$ 14 % of the population mean.

GIS Spatial Analysis

The area of each of the traced slicks was calculated in GIS. Table III-4 shows the average area and the standard deviation of the surface slicks for each of the number of seep sources. Since there was only a single location harboring 6 potential seep sources, it was considered an outlier. The calculation of one seep source producing a slick with an average surface area of 1.698 km^2 is based on the area values of seep sources 1 through 5. There are a total of 175 seep sources, which means that on average 297.15 km^2 is covered daily by the oil slicks in the 53,693 km^2, so slicks can cover 0.55 % of the sea surface area covered by the satellite imagery used in this thesis. A conservative estimate of the oil layer thickness is 0.1 μm (MacDonald et al.1993) and since 1m^3 is ~100 liters, the slicks contribute of an average of about 29,715 liters of oil per day to the sea surface. This is equivalent to 187 barrels per day or 68,213 barrels per year. Hunt (1979) calculated that oil is 84.5% carbon. Based on this ratio, the natural seeps will contribute about 9.165×10^6 liters of carbon per year to the surface. At an estimated density of 0.9 kg/l, the seeps will introduce about 8.248×10^9 grams of carbon per year into the oligotrophic Gulf of Mexico surface waters.

Table III-4. Average area (km^2) and standard deviation of manually traced slicks for the seep sources. The "Number of that seep source" refers to the number of locations symbolized by the seep sources.

Seep Source	**Number of that Seep Source**	**Average Area in km^2**	**Standard Deviation**
1	83	1.744	0.891
2	11	2.201	1.177
3	10	5.819	4.727
4	6	8.036	6.085
5	2	6.500	4.042
6	1	47.465	3.559

Slope analysis

GIS was also used to evaluate the relationship of the seep locations to elevations, such as mounds, banks, and domes, and depressions, such as basins. Seeps on the upper slope seem to be related to faults, as can be determined by their linearity. On the middle slope most seeps are located on the sides or rims of basins. Seeps on the lower slope the seeps are primarily located between the basins. The seep source locations were mapped on the resulting slope analysis from ESRI's Spatial Analyst (Fig. III-12). The average slope value for the seep source locations is 2.80º with a standard deviation of 2.27º. Seventy-seven percent of the seeps are located on areas with less than a 4-degree slope but the graph is heavily skewed to the right (Fig. III-13).

Historical comparisons

It was calculated that 73% of the locations of overlap of the slicks identified by MacDonald et al. in 1996 are less than 3 km from the sources identified in this study (Fig. III-14). The greatest distances are associated with the slicks identified over the Green Garden Banks Lease area; they were 25 to 38 km from sources identified in Green Garden Banks in this project. The source locations identified in this study were then compared to locations identified by Mitchell et al. (1999) in images from the SAR instrument on Earth Satellite. Using the distances calculated by ArcMap, it was evident that 73% of sources from this study were within 5 km from sources identified by Mitchell. The sources in the northeast and on Green Knoll were the most distant from the locations identified in the Earth Satellite study.

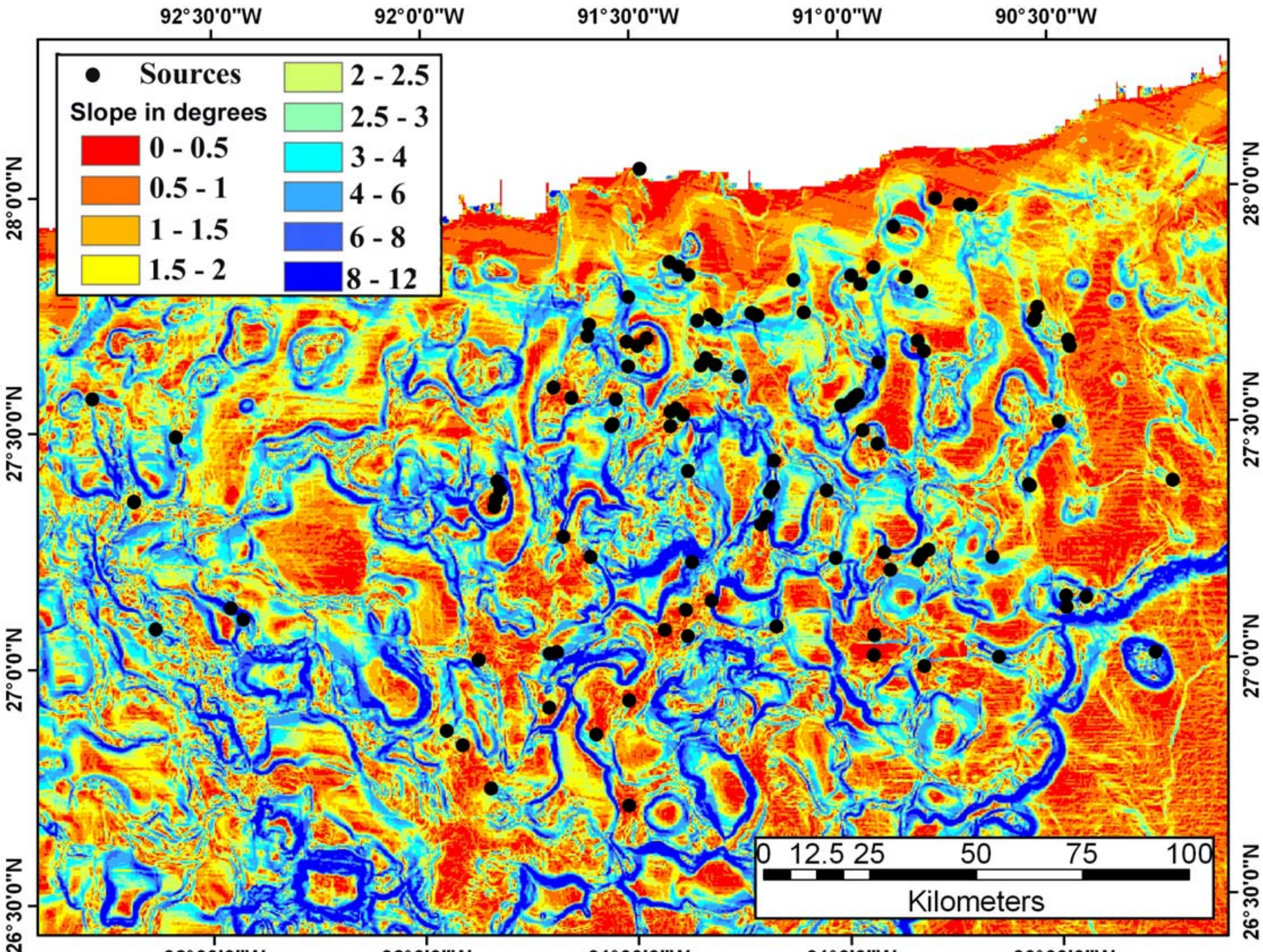

Fig. III-12. Seep sources (black dots) plotted on a slope map (in degrees) created in GIS spatial analyst.

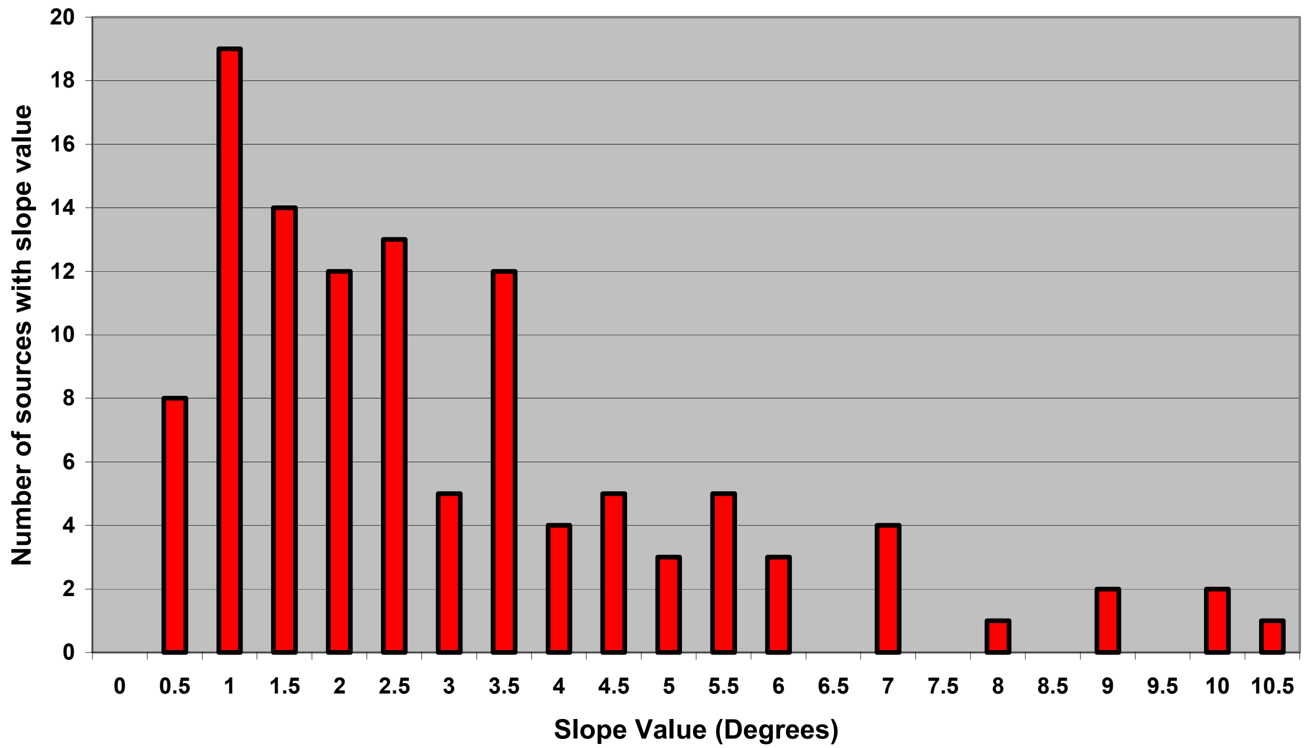

Fig. III-13. Slope value in degrees versus the total number of sources located on that slope value.

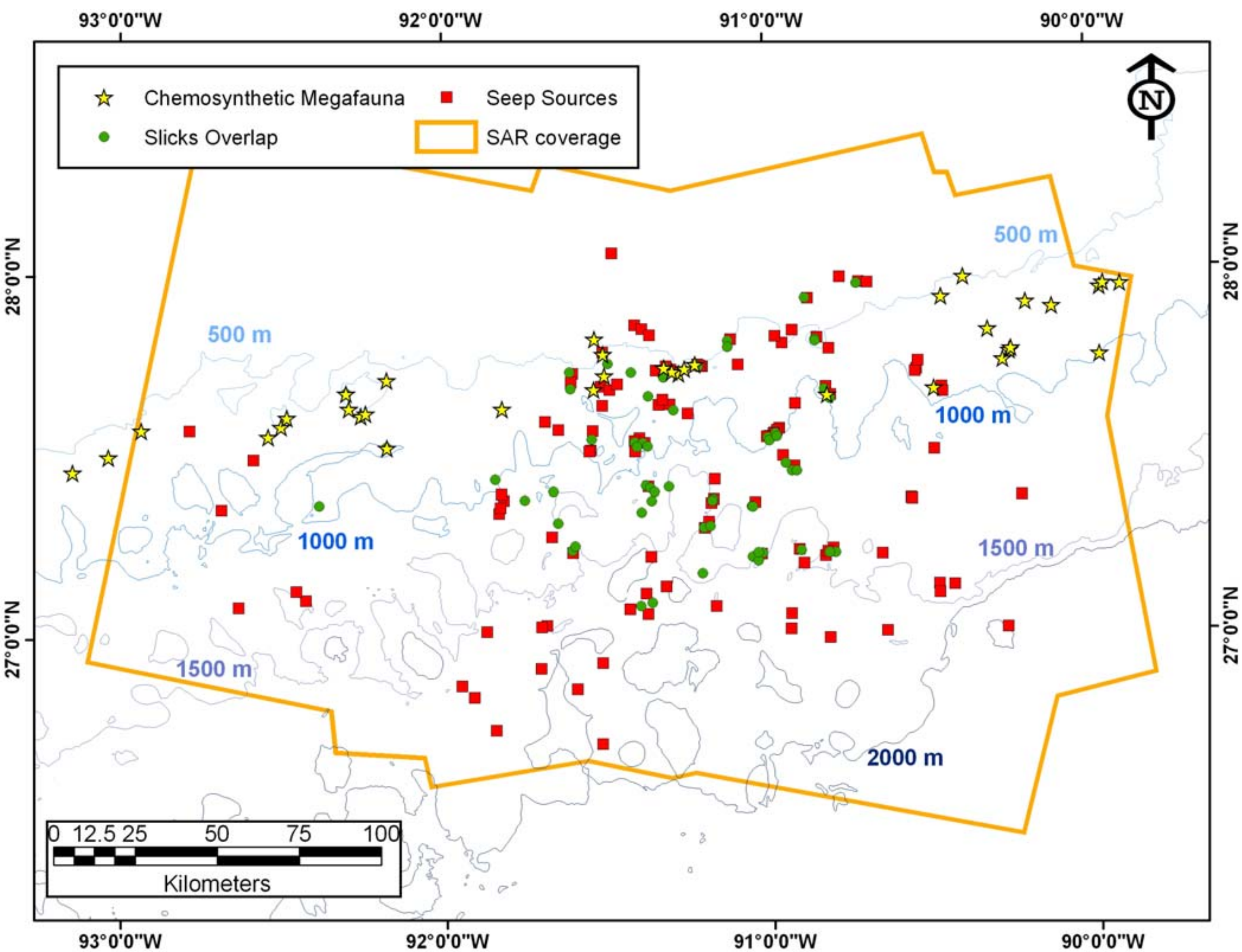

Fig. III-14. Locations of all of the seep sources identified in this study (red squares) were compared to overlap locations of slicks (green dots) and chemosynthetic megafauna (yellow stars) locations published by MacDonald et al. 1996. The orange outline shows the extent of the SAR coverage.

Seep sources related to side-scan sonar mosaics

The locations of the seep sources that are incorporated by a side-scan sonar mosaic of the upper slope in the Green Canyon lease area include well-studied chemosynthetic sites such as Bush Hill, Brine Pool NR-1 and GC234 (Fig. III-15). The sources identified in the SAR images line up with the dark shades, or the high acoustic backscatter on the side-scan sonar mosaic. The high acoustic backscatter represents features associated with seepage: carbonate mounds, sediment flows, and faults. The area around Brine Pool NR-1 site is depicted as high backscatter but no surface slicks were identified right above the Brine Pool NR-1. Slicks are produced by sources to the northwest of Brine Pool NR-1 as revealed in Chapter II. Those three sources are associated with high backscatter patches and the most easterly of these, Tamu-17, is known to researchers for harboring chemosynthetic organisms (Sager 2002). The four sources on Assumption Dome, which is the southwesterly diapir surrounded by faults, are all aligned with patches of high acoustic backscatter. The four source locations in the southeast of the image are also associated with dark backscatter areas that were correlated to a complex of faults. There are several areas of high backscatter that did not have associated seep sources. This could be due to temporal changes in the seepage. Active seeps can not be differentiated from passive seeps in side-scan sonar imagery, so relics of old seeps still appear in the side-scan records and will not be associated with current seep sources identified from surface slicks in recent SAR images (Sager 2002).

As noted by Sager (2002), there are many more disturbances visible in the side-scan sonar mosaic of the middle and lower slope of Green Canyon (Fig. III-16), making it difficult to make a significant correlation between seep location and high backscatter. However, sources located on this mosaic seem to be associated with patches of high backscatter and faults from the surface geology interpretation map (Sager 2002).

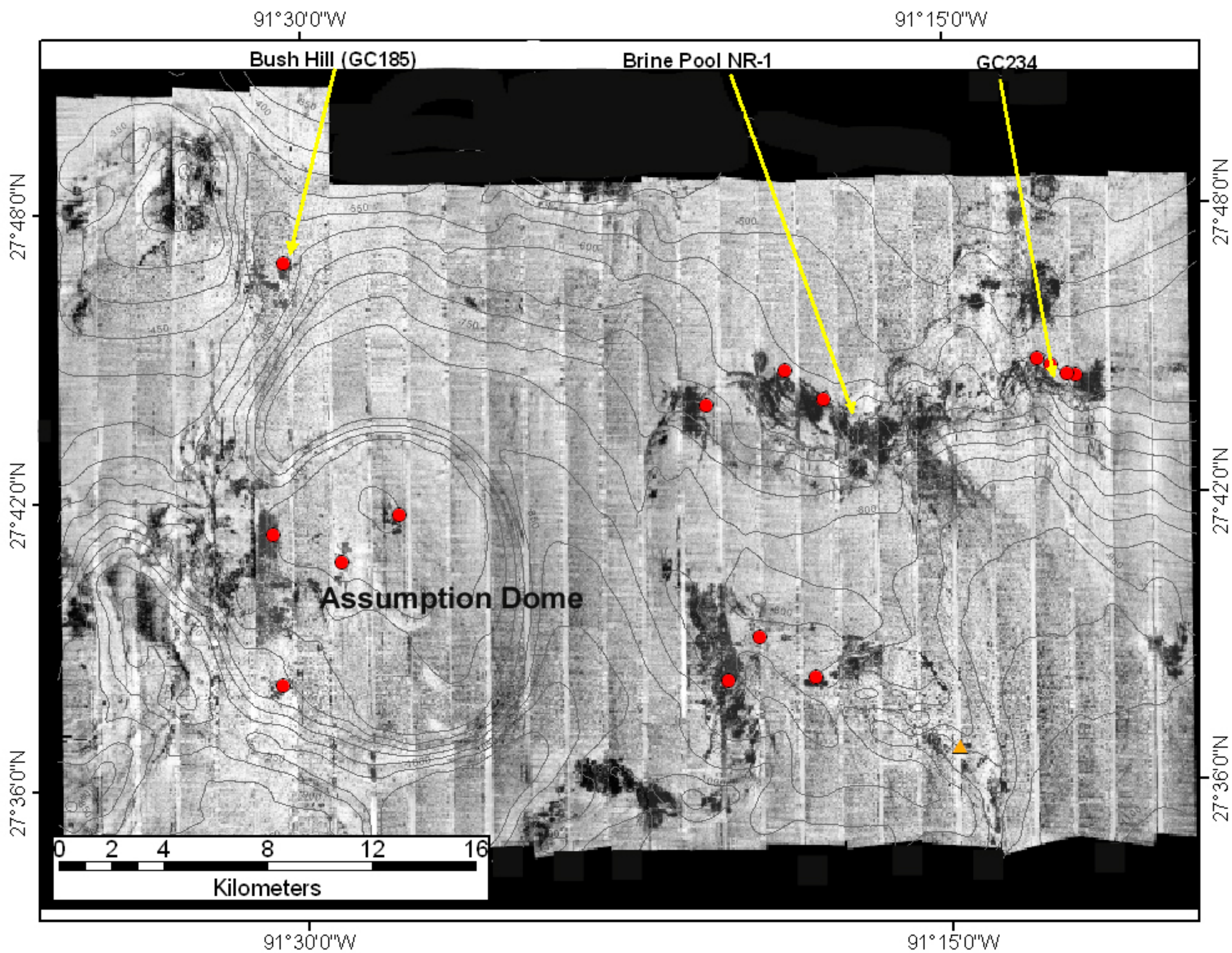

Fig. III-15. Seep sources identified in SAR images compared to the side-scan sonar image of the upper slope of Green Canyon (image by Sager 2002). The red dots indicate one source and the orange triangle indicates two sources. High acoustic backscatter is dark and lighter shades represent low backscatter. Lines are 50 m bathymetry over a depth range of 400 to 1200 m.

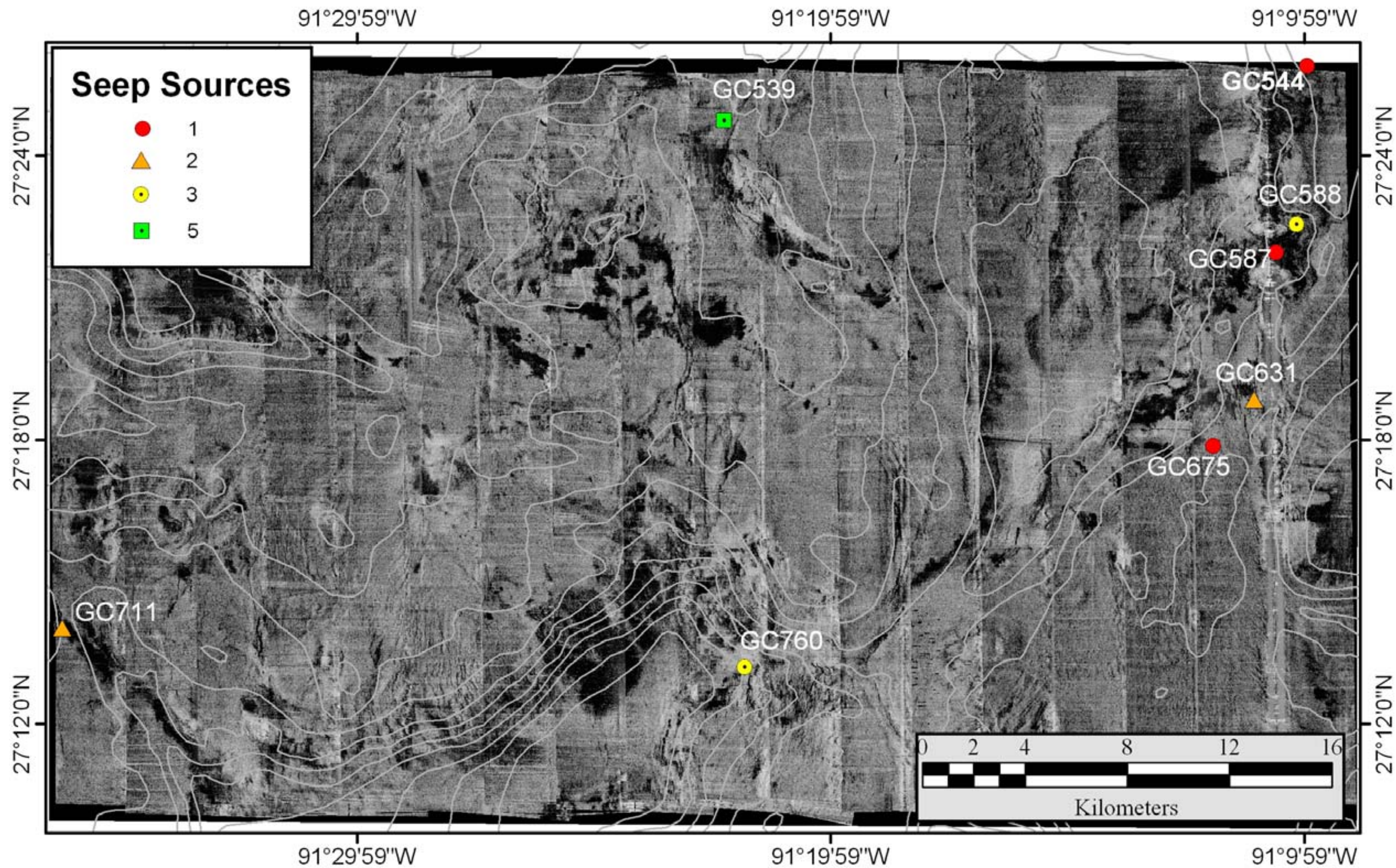

Fig. III-16. Seep sources identified in SAR images plotted on the side-scan sonar mosaic of the mid and lower slope of Green Canyon (image by Sager 2002). High acoustic backscatter is dark and lighter shades represent low backscatter. Contour lines represent 100 m contours over a depth range of 1000 m to 2300 m (in Pygmy basin which contains the three sources of GC760).

The sources seem to be laterally offset from the high backscatter more so than the sources that were plotted on the shallow mosaic. This could possibly be due to the greater influence of water column currents in the deeper water, which would cause the origin of the slick to be more laterally displaced from the source in deeper water than in shallower waters.

Seep sources related to allochthonous salt structure

Figure III-17 shows the identified seep sources plotted on the map of allochthonous salt structure. There is an area of in the northern section of the Green Canyon lease block where some of the seeps are linearly aligned and not associated with sub-seafloor salt structures. These source locations include: GC234, three in GC235, GC148, GC237, GC151, GC152, GC108, GC154, GC199, GC329, GC460, five in GC415, and two in GC416. The linearity of the seep sources could be due to the seeps association to faults, as is known for many of the sources. However, all of the other seep sources are located above allochthonous salt structures 750 to 3000 m below the sea floor but few are related to salt that is deeper than 1500 m (Fig. III-17). Figure III-18 graphically represents that 76% of the sources are located on salt that is less than 1500 m below the seafloor. Sources on the upper slope, are associated with the deeper salt (750-1500 m). Many of the seep sources tend to be associated with the edges of salt sheets, salt seams or salt ridges. Appendix A indicates the 38 seep sources of the 113 that were located on the edge of salt sheets. It is important to note that not one of the 113 sources is located within the bottom of a salt withdrawal basin on the continental slope. The Cameron Basin separates the sources in the Green Canyon area from those in the Garden Banks area (Fig. III-17). The seep source location on top of Green Knoll aligns with an anticline and it is the only one located south of the Sigsbee Escarpment as identified in this study.

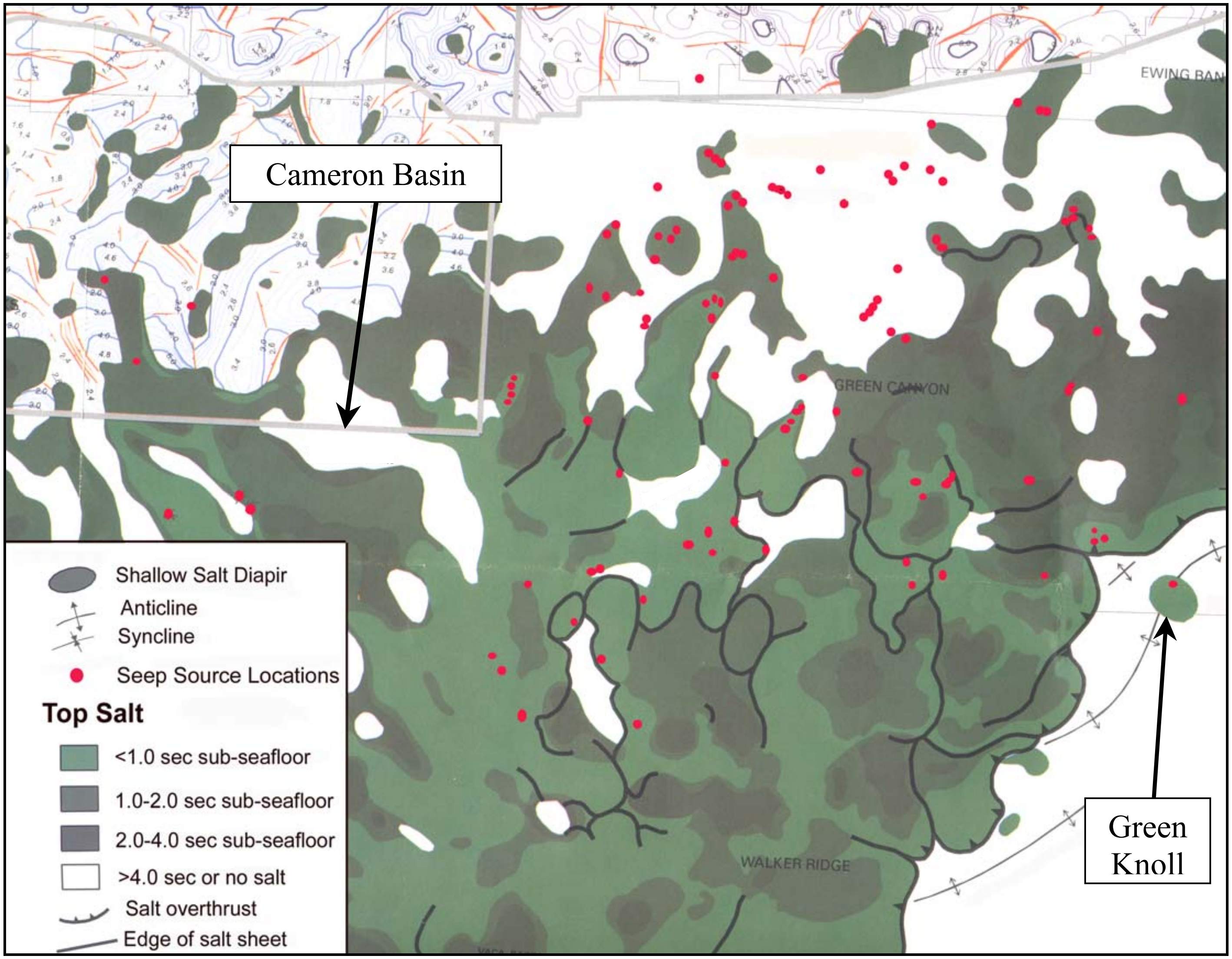

Fig. III-17. Seep sources identified in this study located on an allochthonous salt structure map from Watkins et al. 1996.

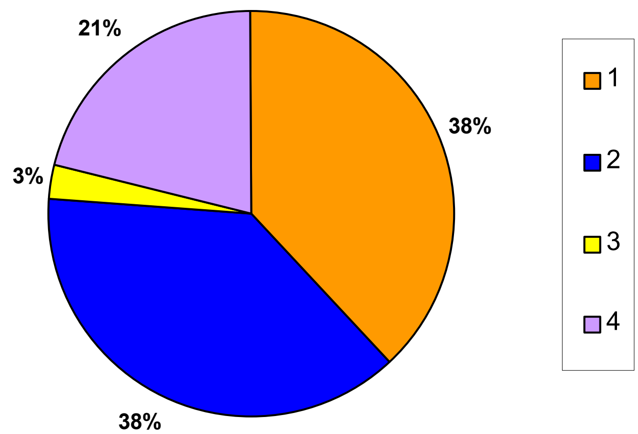

Fig. III-18. Percentage of seeps associated with four depth categories of allochthonous salt. Salt categories are: 1, <1 sec sub-seafloor (<750 m); 2, 1-2 sec sub-seafloor (750 to 1500 m); 3, 2-4 sec sub-seafloor (1500 to 3000m); 4, >4 sec sub-seafloor or no salt (>3000 m).

DISCUSSION

Overlaying manually traced slicks from 11 SAR images acquired over two consecutive summers allowed for the quantification of seep source locations and for a persistence analysis of the surface oil slicks. The average x and y locations of the seep sources, calculated from the origins of the slicks, indicate a more precise estimation of the actual seafloor source location than historical estimates based on slick overlap locations in fewer remotely sensed images. The depth gradient, however, did impact the ability to resolve the source location, but not the ability of a source to produce a surface slick. In deeper waters, the water column currents affect the rising oil and gas bubbles for a longer period of time than their shallower counterparts (MacDonald et al. 2002). The origins of the slicks on the surface represent this lateral offset due to water column current deflections and is referred to as the surfacing perimeter. In deeper waters, so in the southern part of the images, the surfacing perimeter was greater because of the longer influence on the bubble streams by the water column currents. Also, the lack of oil platforms in the deeper waters prevented georeferencing as precise as in the northern part of the images. In turn, these aspects made it more difficult to locate separate sources in waters deeper than 900 m based on the fine scale structure of the slicks. As a result, the source locations in these deeper waters often denote areas that represent more than one sea-floor source (Fig. III-9). However, the lack of correlations between the total numbers of sources with depth (Fig. III-10) and the activity of the sources with depth (Fig. III-11) corroborates that SAR images can be used for locating natural oil and gas seeps over the entire continental slope since all oily seep sources, independent of their depth, are capable of producing a surface signature.

The persistence analysis confirmed that SAR can be a valuable analytical tool for determining the temporal activity of natural oil and gas seeps. However, images must be taken regularly so that all of the seeps in the covered area can be identified, since an average of 58% of the seeps were found per image (Table III-3). Based on a statistical estimation, 20 SAR images are necessary to be 90% confident that the sample mean, the number of identified seeps of the combined 20 images, will be within $\pm$ 10% of the population mean, the number of total seeps (Appendix C). Satellite coverage of the same area over time reduces the chance that a surface expression is continually obscured by weather patterns and improves the ability of the researcher to differentiate slicks from seeps from other surfactants.

Pulsed flows such as the one from the mud volcano from Auger Basin can be tracked on satellite images because an oil slick has been associated with the infrequent eruptions (MacDonald et al. 2000). No slicks were identified above the Auger Basin site on the three images that covered the Garden Banks lease area (Table III-1). The Auger Basin mud volcano eruption of oil and gas has been linked to a temperature flux in the water column (MacDonald et al. 2000). The lack of slicks in the SAR images suggests that no large temperature fluctuation occurred to induce an eruption of oil and gas from the mud volcano at this site during the SAR image collections of 2001 and 2002.

The spatial distribution of the seeps can be qualitatively and quantitatively analyzed with GIS. The seep source locations plot on top of the seep features evident on the side-scan sonar mosaics, which suggests that the estimation of the source location based on the origin of the surface slicks, is quite robust. The topography of the slope is varied and complex and when the sources were plotted on this data, a number of correlations were revealed. On the upper and lower slope the seep sources do not tend to be closely (<2 km) related to topographic elevations and depressions but on the middle slope, the sources tend to be on the top or sides of elevations and on the sides of the basins. A slope analysis of the topography using ESRI's spatial analyst illustrated that 77% of seeps were located on slopes of less than 4 degrees but some were associated with much steeper slopes (Fig. III-12 and Fig. III-13). Local slopes on the sides of basins tend to be steeper but would not have been resolved in the slope analysis based on the bathymetry dataset whose resolution is not high enough to accurately depict the slope of the sides of individual basins. The movement of subsurface salt generates the features and topography of the continental slope so the locations of the seep sources, as estimated from the satellite imagery, were located on a subsurface salt map.

The sources are related to the subsurface salt structures, especially the crests or edges of these structures, because the faults occur at these salt structures. Sources on the upper slope not related to shallow salt structures are known to be related to faults, such as GC234, and, as indicated by their linearity, most of the other sources in that region could be related to faults. The subsurface salt structure depicts salt withdrawal basins but no seeps are located within those basins. The few seeps in the Garden Bank lease area are separated by ~60 km from the main patch of seeps in the Green Canyon area by a large salt-withdrawal basin, Cameron Basin. The lack of seeps in the bottom of these basins has been hypothesized but never been illustrated.

Comparing the source locations to the categories of salt depths reveals several relationships. The deepest salt, deeper than 1500 m, has very little seepage associated with it (Fig. III-17 and Fig. III-18). Seeps on the middle slope tend to be related to shallow salt (<750 m) edges or ridges. Seeps located on the upper slope tend to be related to deeper (750 to1500 m) salt (Fig. III-17). This study did not identify any seeps closely associated with supralobal basins on the lower slope. No slicks are found south of the Sigsbee Escarpment, except for the seep on top of Green Knoll, which is a well-exposed solitary diapir with an anticline running through it to the northwest. An anticline can form an ideal oil and gas trap, which suggests the potential of an oil seep source on the top of Green Knoll. Historical data, however, identified a few slicks south of the escarpment above the continental rise (Mitchell et al. 1999). The SAR images analyzed in this thesis did not cover that far south and thus did not corroborate any of those slicks. Since the Sigsbee Escarpment marks the edge of the salt sheet, it is unlikely that many natural oil and gas seeps will be found south of it.

In Chapter II it was revealed that not all seeps harboring chemosynthetic community sites produce slicks. Figure III-14 shows that sites in the eastern and western parts of the satellite coverage area where chemosynthetic megafauna has been found did not produce slicks captured by the SAR images nor by the study conducted by MacDonald et al. in 1996. The lack of slicks in the eastern part of the coverage area could be due to the tilt of the RADARSAT satellite, which causes the signatures on the side of the images to be faint or imperceptible. The western chemosynthetic communities could be associated with non-oily bubble streams that would not produce a surface oil slick.

SAR imaging has been shown to be a reliable method for the identification of seep sources and the results of this study can be used for exploration of chemosynthetic communities often associated with natural oil and gas seeps across the continental slope. Although some of the sources have been ground-truthed by side-scan or 3-D seismic data, a survey by a submarine or an ROV can finalize the investigation of the sites to determine if there is a chemosynthetic community associated with the seep. Finally, we should continue to collect SAR images covering the Gulf of Mexico slope so that the temporal variation of the seeps can be analyzed even if the ground-truth data is not yet available.

CHAPTER IV

SUMMARY

SUMMARY OF RESULTS

This work was able to determine limits of the technology available to characterize seeps. Individual bubble streams are adequate to produce acoustic evidence in profile data and separate distinct slicks on satellite data. The Northern Gulf of Mexico seep representation (Fig. IV-1) illustrates that Synthetic Aperture Radar (SAR) will only capture a subset of the total number of active seeps. Seeps can consist of either oily or non-oily bubble streams but only oily bubble streams produce a surface expression, a slick that can be captured by SAR. This limitation suggests that Reilly's scheme (1996) on the order of analyses for finding a chemosynthetic community starting with the review of satellite data will not locate non-oily bubble streams from seeps. Through submarine and historical research, it is known that chemosynthetic organisms can thrive near both oily and non-oily seeps. For example, a large mussel community surrounds the non-oily seeps of Brine Pool NR-1. So, not only will SAR studies underestimate the total number of seep sources and the carbon flux potential in the water column, it will also underestimate the density and number of chemosynthetic communities that could be present on the Gulf of Mexico slope since some thrive near non-oily bubble streams not detected with SAR.

Acoustic profiles can distinguish between the oily and non-oily bubble streams. The non-oily bubble streams surveyed did not produce a signature that rose to the sea-surface on the acoustic profiles as exhibited by their oily counterparts. The oily coating on the bubble streams is likely to keep them from dissolving in the water column and it is also hypothesized that the different hydrate structures at the seeps might influence the dissolution of the bubbles. The smaller oily bubbles are hypothesized to be below the

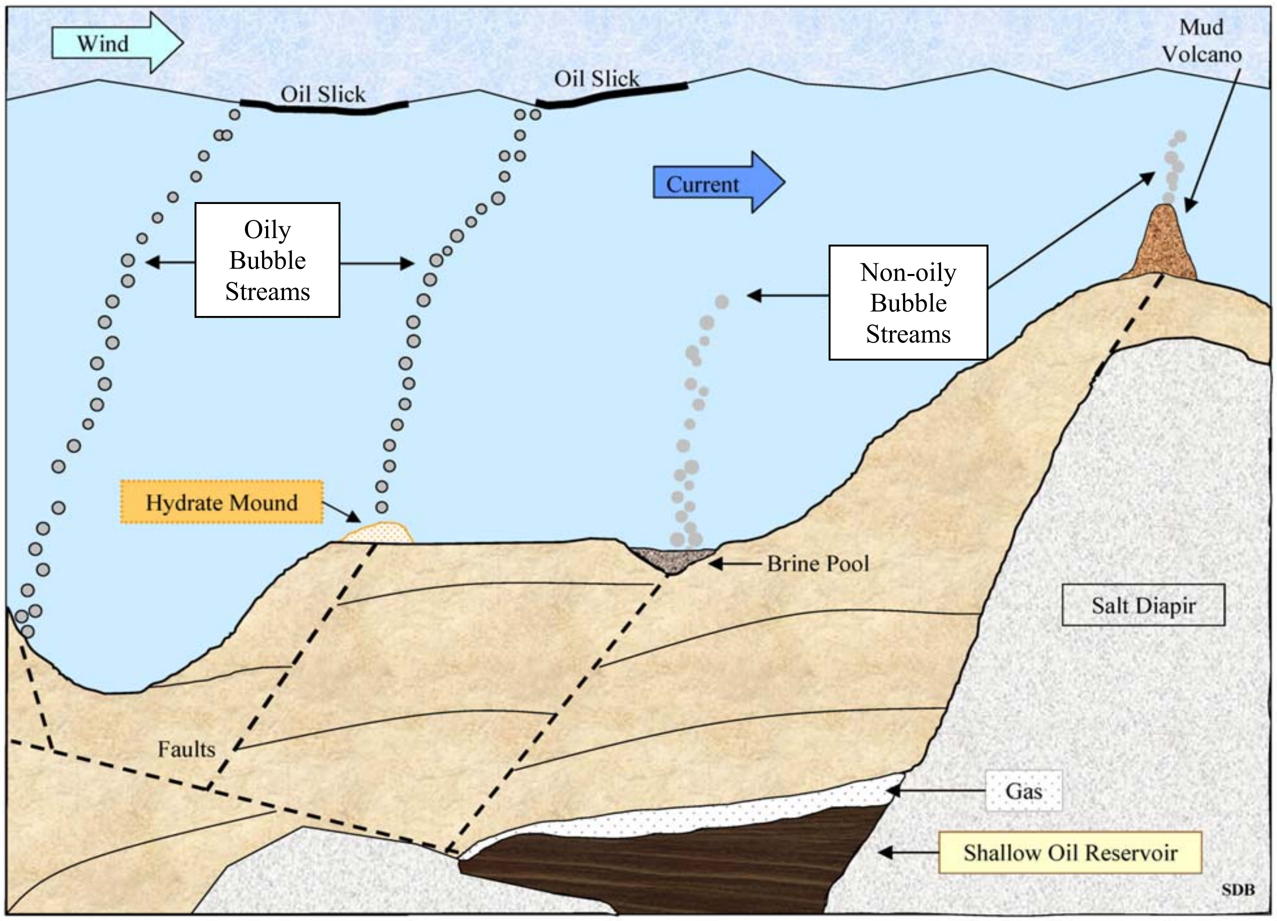

Fig. IV-1. Northern Gulf of Mexico seep representation developed on the basis of the results in this thesis and on literature review.

resonance frequency of the side-scan sonar and therefore, they do not produce a high-backscatter signature on the side-scan records as exhibited by the larger non-oily bubbles. If these techniques are used in combination with SAR, a researcher would be able to provide a more accurate estimate of carbon flux based on both oil and gas seeps. A calculation of the average amount of oil entering the region, based the average area of a slick recorded on these SAR images, is comparable Mitchell's (1999) minimum estimate of 4 x 10^7 liters per year.

The seep source of these slicks was estimated based on the average location of the slick origins on different days. The resulting 113 seep locations (Fig. III-9) identified in this work represent known and previously unidentified seeps. The new seeps are likely to be similar to ground-truthed seeps. However, the composition of the chemosynthetic communities at depths greater than a 1000 m can include different species than their shallower counterparts (Fisher 2003). The fine-scale structures of the slicks indicate that the 113 seep locations depict 175 individual seep sources. Based on the slick areas, the seeps contribute about 8.248 x 10^9 grams of carbon per year to the sea surface. This is a conservative estimate but even then, it is an impressive amount of carbon that should not be neglected when considering carbon fluxes in the oligotrophic Gulf of Mexico.

Geographical Information Systems (GIS) has proven to be an extremely valuable tool. GIS allowed for the analysis of large datasets and the combination of the datasets, such as satellite images, manually traced slicks, and continental slope bathymetry. Spatial analyst was used to accurately calculate the area of the surface slicks and to complete a slope analysis based on the bathymetry dataset. It would be useful to assemble both reliable wind and current data as the SAR images are collected so that they could be imported in the GIS database with the images for immediate analysis.

FUTURE RESEARCH RECOMMENDATIONS

Investigations by high-resolution geophysical data and piston coring of the previously unidentified seep sites would be of interest to researchers and the Minerals Management Services (MMS). Submersible investigations of deeper seeps ($\geq$ 900 m) determined in this thesis warrant the use of DSV Alvin since Alvin can dive deeper than the Johnson Sea Link or the NR-1. It is of interest to further investigate these sites since both researchers and MMS wish to protect chemosynthetic communities from potential harm by future oil exploration and by installation of various types of platforms. As drilling for oil and gas occurs in deeper waters, the SAR slicks might be indicative of the repercussions such activities have on the chemosynthetic communities. Sassen et al. (1993) showed that on the upper continental slope, chemosynthetic communities and major oil fields are associated and Quigley et al. (1999) that the seepage decreased in half where commercial drilling took place off of the California coast. However, several MMS studies indicate that such activities do not have an effect on the seepage providing carbon to the chemosynthetic communities in the Gulf of Mexico. So, in persistence studies of surface slicks, the disappearance of a slick that has previously had a perennial signature could indicate a reduced carbon source to a community due to commercial exploitation of the oil and gas reserves nearby.

Further investigation into the carbon input from the sources is also warranted. The partitioning of the hydrocarbons to the benthos, water column, and surface is of significant interest to modelers. The microbiology of the sea-surface in areas of perennial slicks should be explored in order to provide information to bioremediation scientists interested in the biological removal of anthropogenic oil spills.

REFERENCES

Addy SK, Worzel JL (1979) Gas Seeps and Subsurface Structure off Panama City, Florida. AAPG 63(4):668-675.

Aharon P, Graber ER, Roberts HH (1992) Dissolved Carbon and $\delta^{13}C$ Anomalies in the Water Column Caused by Hydrocarbon Seeps on the Northwestern Gulf of Mexico Slope. Geo-Marine Letters 12:33-40.

Anderson AL, Bryant WR (1990) Gassy Sediment Occurrence and Properties: Northern Gulf of Mexico. Geo-Marine Letters 10:209-220.

Behrens EW (1988) Geology of a Continental Slope Oil Seep, Northern Gulf of Mexico. AAPG Bulletin 72(2):105-114.

Bergquist DC, Williams FM, Fisher CR (2000) Longevity Record for Deep-Sea Invertebrate. Nature 403:499-500.

Boetius A, Ravenschlag K, Schubert CJ, Rickert D, Widdel F, Gieseke A, Amann R, Jorgensen BB, Witte U, Pfannkuche O (2000) A Marine Microbial Consortium Apparently Mediating Anaerobic Oxidation of Methane. Nature 407:623-626.

Bouma AH, Roberts HH (1990) Northern Gulf of Mexico Continental Slope. Geo-Marine Letters 10:177-181.

Brooks JM, Kennicutt MC, Fay RR, McDonald TJ, Sassen R (1984) Thermogenic Gas Hydrates in the Gulf of Mexico. Science 225:409-411.

Brooks JM, Anderson AL, Sassen R, MacDonald IR, Kennicutt MC, Guinasso NL (1994) Hydrate Occurrences in Shallow Subsurface Cores from Continental Slope Sediments, International Conference on Natural Gas Hydrates. Annals of the New York Academy of Sciences 715: 381-391.

Bryant WR, Bryant JR, Feeley MH, Simmons GR (1990) Physiographic and Bathymetric Characteristics of the Continental Slope, Northwest Gulf of Mexico. Geo-Marine Letters 10:182-199.

Bryant WR, Simmons GR, Grim P (1991) The Morphology and Evolution of Basins on the Continental Slope Northwest Gulf of Mexico. Gulf Coast Association of Geological Societies Transactions 41:73-82.

Carney RS (2002) Currents in a Cul-de-Sac. NOAA. Available online: http://www.oceanexplorer.noaa.gov/explorations/02mexico/background/currents/currents.html, February 17, 2003.

Childress JJ, Fisher CR, Brooks JM, Kennicutt MC, Bridigare R, Anderson AE (1986) A Methanotrophic Marine Molluscan (Bivalvia, Mytilidae) Symtiosis- Mussels Fueled by Gas. Science 233(4470):1306-1308.

Eckblad JW (1991) How many samples should be taken? BioScience 41(5):346-348

Espedal HA, Johannessen OM, Knulst J (1996) Satellite Detection of Natural Films on the Ocean Surface. Geophysical Research Letters 23(22):3151-3154.

Espedal HA (2001) Oil Spill and its Look-alikes in ERS SAR Imagery. Earth Observation and Remote Sensing 16(5):813-825.

Fisher CR (1990) Chemoautotrophic and Methanotrophic Symbioses in Marine Invertebrates. Reviews in Aquatic Sciences 2(3-4):399-436.

Fisher CR (2003) Chemosynthetic Communities in the Gulf of Mexcio. The Oceanography Society-Oceanology International Americas 2003 Ocean Conference, New Orleans, LA, June 3-6, 2003.

Guinasso N (2002) The Physical Environment at the Seep Sites. In: I. MacDonald (Editor), Stability and Change in Gulf of Mexico Chemosynthetic Communities. Volume II: Technical Report. Minerals Management Service, New Orleans, Louisiana, pp 5-1-5-20.

Hamilton P (1990) Deep Currents in the Gulf of Mexico. Journal of Geophysical Research 20(7)1087-1104.

Henschel MD, Olsen RB, Hoyt V, Vachon PW (1997) The Ocean Monitoring Workstation: Experience Gained with RadarSat, Geomatics in the Era of RADARSAT 92-97, Ottawa, Canada.

Hovland-Espedal HA, Johannessen JA, Digranes G (1994) Slick detection in SAR images. Proceedings of International Geoscience and Remote Sensing Symposium 1994, Pasadena, California, 2038-2040.

Hunt JM (1979) Petroleum geochemistry and geology. W.H. Freeman and Company, San Francisco, pp 617.

Hyun JB, Bennison BW, LaRock PA (1997) The Formation of Large Bacterial Aggregates at Depth Within the Louisiana Hydrocarbon Seep Zone. Microbial Ecology 33:216-222.

Kennicutt MC, Brooks JM (1990) Recognition of Areas Effected by Petroleum Seepage-Northern Gulf of Mexico Continental Slope. Geo-Marine Letters 10(4):221-4.

Kennicutt MC, Brooks JM, Bidigare RR, Denoux GJ (1988a) Gulf of Mexico Hydrocarbon Seep Communities-I. Regional Distribution of Hydrocarbon Seepage and Associated Fauna. Deep-Sea Research 35(9):1639-51.

Kennicutt MC, Brooks JM, Denoux GJ (1988b) Leakage of Deep, Reservoired Petroleum to the Near Surface on the Gulf of Mexico Continental Slope. Marine Chemistry 24:39-59.

Kornacki AS, Kendrick JW, Berry JL (1994) Impact of Oil and Gas Vents and Slicks on Petroleum Exploration in the Deepwater Gulf of Mexico. Geo-Marine Letters 14:160-9.

Kvenvolden KA, Harbaugh, JW (1983) Reassessment of the Rates at which Oil from Natural Sources Enters the Marine Environment. Marine Environmental Research 10(4): 223-243.

Leifer I, MacDonald IR (2003) Dynamics of the Gas Flux from Shallow Gas Hydrate Deposits Interaction Between Oily Hydrate Bubbles and the Oceanic Environment. Earth and Planetary Science 210:411-424.

Liu JY, Bryant WR (1999) Texas A&M University Gulf of Mexico/ NOAA Bathymetry, Texas Sea Grant College Program, College Station, Texas.

MacAvoy SE, Carney RS, Fisher CR, Macko SA (2002) Use of Chemosynthetic Biomass by Large, Mobile, Benthic Predators in the Gulf of Mexico. Marine Ecology Progress Series 225:65-78.

MacDonald IR, Boland GS, Bake JS, Brooks JM, Kennicutt MC, Bidigare RR (1989) Gulf of Mexico Hydrocarbon Seep Communities II. Spatial Distribution of Seep Organisms and Hydrocarbons at Bush Hill. Marine Biology 101:235-247.

MacDonald IR, Reilly JF, Guinasso N, Brooks JM, Carney RS, Bryant WA, Bright TJ (1990a) Chemosynthetic Mussels at a Brine-Filled Pockmark in the Norhtern Gulf of Mexico. Science 248:1096-1099.

MacDonald IR, Guinasso NL, Reilly JF, Brooks JM, Callender W.R, Gabrielle S (1990b) Gulf of Mexico Hydrocarbon Seep Communities: VI. Patterns of Community Structure and Habitat. Geo-Marine Letters 10:244-252.

MacDonald IR, Guinasso NL, Ackleson SG, Amos JF, Duckworth R, Sassen R, Brooks JM (1993) Natural Oil Slicks in the Gulf of Mexico Visible from Space. Journal of Geophysical Research 98(C9):16351-16364.

MacDonald IR, Guinasso NL, Sassen R, Brooks JM, Lee L, Scott KT (1994) Gas Hydrate that Breaches the Sea Floor on the Continental Slope of the Gulf of Mexico. Geology 22:699-702.

MacDonald IR, Reilly JF, Best SE, Venkataramaiah R, Sassen R, Guinasso NL, Amos J (1996) Remote Sensing Inventory of Active Seeps and Chemosynthetic Communities in the Northern Gulf of Mexico. Hydrocarbon migration and its near-surface expression: AAPG Memoir 66:27-37.

MacDonald IR, Buthman D, Sager W, Peccini M, Guinasso N (2000). Pulsed Oil Discharge from a Mud Volcano. Geology 27(10):907-910.

MacDonald IR, Leifer I, Sassen R, Stine P, Mitchell R, Guinasso N (2002). Transfer of Hydrocarbons from Natural Seeps to the Water Column and Atmosphere. Geofluids 2:95-107.

MacDonald IR (2002), Stability and Change in Gulf of Mexico Chemosynthetic Communities. U.S. Department of the Interior, New Orleans, Louisiana, pp 456

MacDonald IR, Vardaro M, Bender L (2003) A temperature and Photographic Time-Series from a Seafloor Gas Hydrate Deposit on the Gulf of Mexico Slope. Geophysical Research Abstracts 5:12714.

MacGregor DS (1993) Relationships Between Seepage, Tectonics and Subsurface Petroleum Reserves. Marine and Petroleum Geology 10(6):606-619.

Mitchell R, MacDonald IR, Kvenvolden K (1999) Estimates of Total Hydrocarbon Seepage into the Gulf of Mexico Based on Satellite Remote Sensing Images. EOS 30(49):242.

Mitchell R, MacDonald I, Kvenvolden K (2000) Estimates of Total Hydrocarbon Seepage into the Gulf of Mexico Based on Satellite Remote Sensing Images, 2000 Ocean Science meeting, San Antonio, Texas.

Melsheimer C, Alper W, Gade M (2001) Simultaneous Observations of Rain Cells Over the Ocean by the Synthetic Aperture Radar Aboard the ERS Satellites and by Surface-based Weather Radars. Journal of Geophysical Research 106 (C3):4665-4678.

Orange DL, Yun J, Maher N, Barry J, Greene G (2002) Tracking California Seafloor Seeps with Bathymetry, Backscatter and ROVs. Continental Shelf Research 22:2273-2290.

Quigley D, Hornafius JS, Luyendyk BP, Francis RD, Clark J, Washburn L (1999) Decrease in Natural Marine Hydrocarbon Seepage near Coal Oil Point, California, Associated with Offshore Oil Production. Geology 27(11):1047-1050.

Rehder G, Brewer PW, Peltzer ET, Fiederich G (2002) Enhanced Lifetime of Methane Bubble Streams Within the Deep Ocean. Geophysical Research Letters 29(15): art. no. 1731.

Reilly J (1995) Geological Controls on the Distribution of Chemosynthetic Communities in the Gulf of Mexico. Dissertation, University of Texas at Dallas, Dallas, pp 223.

Reilly JF, MacDonald IR, Biegert EK, Brooks JM (1996) Geologic controls on the Distribution of Chemosynthetic Communities in the Gulf of Mexico. Hydrocarbon Migration and its Near-Surface Expression. D. Schumacher and M. A. Abrams. Tulsa, Oklahoma, American Association Petroleum Geology 66: 38-61.

Roberts HH, Aharon P, Carney R, Larkin J, Sassen R (1990) Sea Floor Responses to Hydrocarbon Seeps, Louisiana Continental Slope. Geo-Marine Letters 10:232-243.

Roberts HH (1996) Surface Amplitude Data: 3D-Seismic for Interpretation of Sea Floor Geology (Louisiana Slope). Gulf Coast Association of Geological Societies Transactions 46:353-362.

Roberts HH, Doyle E, Clark B, Kaluza M, Hartsook A (1996) 3D -Seismic Amplitude Analysis of the Sea Floor: An Important Interpretive Method for Imporved Geohazards Evaluations, Offshore Technology Conference. Houston, Texas, p 283-292.

Roberts HH, Carney R (1997) Evidence of Episodic Fluid, Gas, and Sediment Venting on the Northern Gulf of Mexico Slope. Economic Geology 92:289-293.

Roberts HH, Sassen R, Milkov AV (2001) Seafloor Expression of Fluid and Gas Expulsion from Deep Petroleum Systems, Continental Slope of the Northern Gulf of Mexico, GCSSEPM Foundation 21st Annual Research Conference; Petroleum systems of Deep-Water Basins, Houston, Texas, December 2-5, p 407-421.

Roberts HH, Hunt J, Shedd W, Sassen R (2002) Surficial Gas Hydrates, Part of the Fluid and Gas Expulsion Response Spectrum: Identification From 3D Seismic Data, 2002 Offshore Technology Conference, Houston, Texas, May 6-9.

Sager WW, Macdonald IR, Bryant WR, Carlson RL, Prior DB (1998) *TAMU*^{2} Digital Side-Scan Sonar Survey of Louisiana Slope Areas Containing Active Oil Seeps and Halokinetic Sediment Modification, paper 8595, Proceedings of the 1998 Offshore Technology Conference, Houston, Texas, 4-7 May 1998, p 57-69.

Sager WW (2002) Geophysical Detection and Characterization of Chemosynthetic Organism Sites. In: MacDonald IR (Editor), Stability and Change in Gulf of Mexico Chemosynthetic Communities. U.S. Department of the Interior, New Orleans, Louisiana, pp 456.

Sager WW, MacDonald IR, Hou R (2003) Geophysical Signatures of Mud Mounds at Hydrocarbon Seeps on the Louisiana Continental Slope, Northern Gulf of Mexico, Marine Geology 198: 97-132.

Sassen R, Brooks JM, MacDonald IR, Kennicutt MC, Guinasso NL, Requejo AG (1993) Association of Oil Seeps and Chemosynthetic Communities with Oil Discoveries, Upper Continental Slope, Gulf of Mexico. Gulf Coast Association of Geological SocietiesTransactions 43: 349-355.

Sassen R, MacDonald IR, Guinasso N, Joye S, Requejo A, Sweet S, Alcala-Herrera J, DeFreitas D, Schink D (1998) Bacterial Methane Oxidation in Sea-Floor Gas Hydrate: Significance to Life in Extreme Environments. Geology 26:851-854.

Sassen R, Sweet ST, Milkov AV, DeFreitas DA, Salata GG, McDade EC (1999) Geology and Geochemistry of Gas Hydrates, Central Gulf of Mexico Continental Slope. Gulf Coast Association of Geological Societies Transactions 49:462-468.

Sassen R, Roberts HH, Milkov AV, DeFreitas DA (2001a) Sea Floor Vents, Seeps, and Gas Hydrate: Relation to Flux Rate from the Deep Gulf of Mexico Petroleum System, GCSSEPM foundation 21st Annual Research Conference. Petroleum Systems of Deep-Water Basins, Houston, Texas, Dec. 2-5.

Sassen R, Sweet S, Milkov A, DeFreitas D, Kennicutt MC (2001b) Thermogenic Vent Gas and Gas Hydrate in the Gulf of Mexico Slope: Is Gas Hydrate Decomposition Significant? Geology 29:107-110.

Simmons G, Bryant W, Bluffer R, Lee G, Fiduk C (1996) Regional Distribution of Salt and Basin Architecture in the Northwestern Gulf of Mexico. 45th Annual Convention of Gulf Coast Association of Geological Societies, San Antonio, Texas, Oct. 2-4, p 93-94.

Sloan ED (1990) Clathrate Hydrates of Natural Gases. Marcel Drekker, Inc., New York, pp 641.

Venkataramaiah RH (1996) Application of an Integrated Environmental Monitoring Model for Natural Hydrocarbon Seeps in the Gulf of Mexico. Dissertation Thesis, Texas A&M University, College Station, pp 166.

Watkins J, Bryant WR, Buffleer R (1996) Sturctural Framework Northern Gulf of Mexico. Gulf Coast Association of Geological Societies, San Antonio, Texas, p 95.

APPENDIX A

SLICK ORIGIN LOCATIONS FOR EVERY SOURCE AND THE RESULTING AVERAGE X AND Y LOCATION (WGS 84, UTM 15N) OF THE SEEP SOURCES IN MMS LEASE BLOCKS AND THEIR ESTIMATED DEPTH IN METERS. SLOPE REPRESENTS THE SLOPE OF THE SEAFLOOR IN DEGREES. SALT CATAGORIES ARE: 1, <1 SEC SUB-SEAFLOOR; 2, 1-2 SEC SUB-SEAFLOOR; 3, 2-4 SEC SUB-SEAFLOOR; 4,>4 SEC SUB-SEAFLOOR OR NO SALT. EDGE SYMBOLIZES THAT THE SEEP SOURCE IS ON THE EDGE OF A SALT SHEET OR BETWEEN 2 SUB-SEAFLOOR SALT CATAGORIES.

		X	Y	Sources	Total origins	Slope	Salt	Salt Edge
1		649787.7044	3104287.9951					
Shelf		649754.4225	3104121.5857					
100 m		649920.8319	3104239.5851					
	avg	**649820.9862**	**3104216.3886**					
	sdev	88.0556	85.5954	1	3	**0.71**	4	
2		645921.4602	3073290.4054					
GC185		648051.9452	3074884.3239					
550 m		647199.7512	3073937.4416					
		646884.1238	3073874.3162					
		646584.2778	3073905.8789					
		647452.2532	3074205.7250					
		647515.3786	3074000.5671					
	avg	**647087.0271**	**3074014.0940**					
	sdev	696.7929	475.2288	1	7	**2.92**	4	

		X	Y	Sources	Total origins	Slope	Salt	Salt Edge
3		637803.0054	3068225.3925					
GC227		637925.8726	3067948.9414					
500 m		637895.1558	3066459.1769					
	avg	**637874.6780**	**3067544.5036**					
	sdev	63.9421	950.0299	1	3	**1.68**	2	Edge
4		637173.3112	3065522.3147					
GC271		637265.4616	3064892.6205					
600 m		637726.2135	3065122.9964					
		637864.4390	3064186.1343					
	avg	**637507.3563**	**3064931.0165**					
	sdev	339.3650	560.5990	1	4	**1.18**	2	
5		647309.8528	3063710.0240					
GC272		646019.7475	3062988.1793					
650 m		646664.8002	3064078.6255					
		646879.8177	3064078.6255					
		646173.3315	3063863.6079					
		647140.9105	3062865.3122					
	avg	**646698.0767**	**3063597.3957**					
	sdev	517.6866	539.2234	1	6	**3.06**	2	
6		649572.6528	3062617.3264					
GC273		649874.4445	3063183.0745					
650 m		649369.9747	3063153.3998					
		649488.6734	3061981.2494					
		648190.4055	3061803.2012					
	avg	**649299.2302**	**3062547.6503**					
	sdev	647.3054	642.3717	1	5	**1.60**	2	
7		650423.4264	3064429.4117					
GC273		650964.9896	3064058.4780					
600 m		651654.9262	3064785.5081					
		651966.5105	3064451.6678					
		651973.9292	3064147.5021					
		651847.8117	3064058.4780					
		651684.6009	3064414.5744					
	avg	**651502.3135**	**3064335.0886**					
	sdev	586.8707	264.5432	1	7	**1.43**	2	

		X	Y	Sources	Total origins	Slope	Salt	Salt Edge
8		646903.4037	3058160.9551					
GC316		647019.4438	3057882.4588					
800 m		647441.8299	3057552.9049					
		646416.0352	3057831.4012					
		647553.2284	3057576.1129					
	avg	**647066.7882**	**3057800.7666**					
	sdev	455.4382	249.6260	1	5	**3.70**	2	Edge
9		664177.2594	3057954.4695					
GC320		664473.4915	3058092.2519					
800 m		664163.4812	3057658.2374					
		664115.2573	3057913.1348					
		663839.6926	3058388.4840					
	avg	**664153.8364**	**3058001.3155**					
	sdev	225.2753	267.3209	1	5	**0.80**	2	
10		667986.9423	3058099.1410					
GC321		667525.3713	3058050.9172					
800 m		667291.1413	3058801.8312					
		667194.6936	3057699.5721					
		667442.7019	3057961.3587					
	avg	**667488.1701**	**3058122.5640**					
	sdev	307.0724	409.8765	1	5	**3.66**	2	
11		665782.4242	3059449.4084					
GC320		665803.0915	3059056.7286					
800 m		665396.6335	3058953.3918					
		664928.1734	3060117.6530					
		665272.6294	3060096.9856					
		664969.5081	3060344.9939					
	avg	**665358.7434**	**3059669.8602**					
	sdev	380.1833	596.0900	1	6	**2.28**	2	
12		660037.7737	3046396.6531					
GC451		660156.6057	3046436.2637					
1000 m		659889.2337	3046812.5650					
		659592.1538	3047089.8396					
		660334.8536	3045465.8026					
	avg	**660002.1241**	**3046440.2248**					
	sdev	281.3647	614.8271	1	5	**3.24**	1	

		X	Y	Sources	Total origins	Slope	Salt	Salt Edge
13		658532.5686	3047941.4688					
GC407		658790.0379	3047862.2475					
1000 m		657898.7981	3048387.0887					
		658136.4620	3047654.2915					
		658542.4713	3047258.1849					
	avg	**658380.0676**	**3047820.6563**					
	sdev	356.6059	412.6810	1	5	**1.74**	1	
14		657344.2488	3046693.7330					
GC407		656660.9650	3047238.3796					
1000 m		657007.5582	3047248.2823					
	avg	**657004.2573**	**3047060.1316**					
	sdev	341.6539	317.3491	1	3	**1.71**	1	
15		643901.6490	3044218.8897					
GC448		643048.9090	3043583.6854					
1000 m		643901.6490	3044358.1125					
		643248.8036	3044466.2319					
	avg	**643525.2526**	**3044156.7299**					
	sdev	442.2201	395.2174	1	4	**3.10**	4	
16		642585.4541	3043063.7043					
GC448		643246.3359	3044464.0341					
1000 m		643398.8470	3043784.6662					
		643421.9548	3043793.9093					
	avg	**643163.1480**	**3043776.5785**					
	sdev	392.9315	571.8830	1	4	**2.19**	4	
17		629758.7472	3052983.2227					
GC357		629927.5111	3053187.5159					
800 m		629199.1616	3052308.1671					
	avg	**629628.4733**	**3052826.3019**					
	sdev	381.2502	460.1974	1	3	**0.56**	2	
18		633867.7106	3050621.0700					
GC402		634325.2135	3050610.0458					
800 m		633112.5553	3049750.1609					
	avg	**633768.4931**	**3050327.0922**					
	sdev	612.3872	499.6676	1	3	**0.43**	2	

		X	Y	Sources	Total origins	Slope	Salt	Salt Edge
19		701651.7284	3050455.7205					
GC416		700656.2026	3050538.6810					
900 m		701187.1497	3050588.4573					
		700241.4002	3051600.5752					
		700241.4002	3050704.6020					
		702464.7412	3052612.6932					
		700291.1765	3051749.9041					
		701568.7680	3050040.9181					
	avg	**701037.8208**	**3051036.4439**					
	sdev	818.4367	861.7857	1	8	**9.54**	4	
20		699942.7424	3050372.7601					
GC416		699063.3613	3051003.2597					
900 m		698698.3351	3051252.1412					
		701037.8208	3050804.1546					
		701104.1892	3050090.6944					
		700689.3868	3049808.6287					
		700822.1236	3049974.5497					
		700175.0318	3050206.8391					
	avg	**700191.6239**	**3050439.1284**					
	sdev	907.0539	521.7567	1	8	**8.63**	4	
21		700031.1333	3049387.3484					
GC415		699400.7781	3049357.8005					
900 m		699440.1753	3049515.3893					
		698898.4638	3049751.7725					
		698849.2173	3049830.5669					
	avg	**699323.9535**	**3049568.5755**					
	sdev	481.1260	213.4823	1	5	**1.96**	4	
22		698376.4509	3049741.9232					
GC415		699272.7372	3049229.7596					
900 m		699410.6274	3049357.8005					
		698809.8201	3049160.8145					
		700011.4347	3049269.1568					
	avg	**699176.2140**	**3049351.8909**					
	sdev	619.6220	229.3640	1	5	**3.41**	4	

		X	Y	Sources	Total origins	Slope	Salt	Salt Edge
23		697726.3971	3048382.7198					
GC415		697726.3971	3049889.6627					
900 m		697913.5338	3048205.4324					
		698061.2733	3048225.1310					
		698209.0128	3047969.0492					
	avg	**697927.3228**	**3048534.3990**					
	sdev	211.0832	771.8861	1	5	**5.17**	4	
24		697224.0828	3049416.8963					
GC415		697499.8632	3048234.9803					
900 m		697883.9859	3047841.0083					
		697706.6985	3048185.7338					
	avg	**697578.6576**	**3048419.6547**					
	sdev	283.7556	687.5430	1	4	**6.82**	4	
25		696624.3230	3050289.7996					
GC415		697221.6385	3048132.8269					
900 m		697188.4543	3047817.5771					
		697838.6526	3047764.1645					
	avg	**697218.2671**	**3048501.0920**					
	sdev	496.1680	1203.5155	1	4	**8.84**	4	
26		657337.7557	3082338.5806					
GC99		656787.4774	3082323.2951					
250 m		656970.9035	3081085.1690					
		656023.2020	3082552.5777					
		656833.3339	3082246.8676					
		656680.4788	3082965.2864					
	avg	**656772.1919**	**3082251.9627**					
	sdev	431.9069	628.2077	1	6	**4.43**	2	
27		659126.1601	3080962.8849					
GC99		658652.3093	3080978.1704					
250 m		658713.4514	3080748.8878					
		659859.8645	3081956.4429					
		658682.8804	3081192.1675					
	avg	**659006.9331**	**3081167.7107**					
	sdev	514.4431	467.9713	1	5	**3.14**	2	

		X	Y	Sources	Total origins	Slope	Salt	Salt Edge
28		661969.2645	3079342.6211					
GC143		662030.4066	3079082.7675					
330 m		660486.5703	3078991.0544					
		660975.7065	3079312.0501					
		661097.9906	3079312.0501					
		660792.2804	3079571.9037					
		662060.9776	3079419.0486					
		660828.8652	3079057.4883					
	avg	**661280.2577**	**3079261.1230**					
	sdev	637.4914	199.8460	1	8	**1.14**	2	
29		663222.8417	3068100.4421					
GC232		663621.8378	3068345.9781					
650 m		663744.6058	3068806.3582					
		662501.5796	3068760.3202					
		663284.2257	3068345.9781					
		663284.2257	3068867.7422					
	avg	**663276.5527**	**3068537.8032**					
	sdev	434.0234	314.7615	1	6	**2.36**	2	
30		668029.5514	3068440.4993					
GC233		668529.4218	3068701.3013					
550 m		667051.5441	3069114.2377					
		667258.0123	3069255.5054					
		668149.0856	3068538.3001					
		667453.6138	3068168.8306					
		668246.8864	3069288.1057					
	avg	**667816.8736**	**3068786.6829**					
	sdev	559.5006	437.6224	1	7	**1.75**	2	Edge
31		665845.3351	3069592.3746					
GC233		665660.6004	3070027.0445					
550 m		666910.2764	3070450.8477					
		666127.8706	3069624.9748					
		666877.6762	3070005.3110					
		666443.0063	3069983.5775					
		666616.8742	3069940.1105					
		666138.7373	3069385.9064					
	avg	**666327.5471**	**3069876.2684**					
	sdev	461.6929	331.5153	1	8	**3.27**	2	Edge

		X	Y	Sources	Total origins	Slope	Salt	Salt Edge
32		676027.4777	3070146.5787					
GC234		675788.4092	3070168.3122					
550 m		676570.8151	3070418.2474					
		676896.8175	3069679.3086					
		675092.9374	3070776.8501					
		675408.0731	3070994.1850					
	avg	**675964.0883**	**3070363.9137**					
	sdev	684.2572	474.3183	1	6	**3.14**	4	
33		677559.6891	3069548.9076					
GC235		678244.2942	3070190.0457					
550 m		676885.9508	3069679.3086					
		677353.2209	3069505.4406					
		677244.5534	3069929.2438					
	avg	**677457.5417**	**3069770.5893**					
	sdev	503.0846	286.7463	1	5	**0.99**	4	
34		677146.7527	3070016.1778					
GC235		677277.1537	3069353.3061					
550 m		677114.1525	3070146.5787					
		676896.8175	3069701.0421					
		677135.8860	3069777.1093					
	avg	**677114.1525**	**3069798.8428**					
	sdev	137.2398	306.8774	1	5	**0.91**	4	
35		676896.8175	3069907.5103					
GC235		676885.9508	3069690.1753					
550 m		676125.2784	3070179.1790					
		676233.9459	3070342.1802					
		676462.1476	3070483.4479					
	avg	**676520.8280**	**3070120.4985**					
	sdev	359.4742	322.0483	1	5	**1.62**	4	
36		685593.1621	3078479.2090					
GC148		684979.3220	3078187.6349					
450 m		686897.5724	3077757.9468					
		686928.2644	3077404.9888					
		686652.0363	3076683.7266					
		685746.6222	3078141.5969					
		685086.7440	3079307.8932					
		685593.1621	3078417.8250					
	avg	**685934.6107**	**3078047.6027**					
	sdev	786.4305	783.5027	1	8	**1.64**	4	

		X	Y	Sources	Total origins	Slope	Salt	Salt Edge
37		687336.4942	3071472.9090					
GC237		688445.9288	3070811.5153					
600 m		688968.6433	3070832.8506					
		689331.3431	3068838.0017					
		687869.8762	3070011.4422					
	avg	**688390.4571**	**3070393.3437**					
	sdev	806.9209	1012.2293	1	5	**1.87**	4	
38		700843.8207	3077726.8982					
GC152		701266.6237	3078127.4484					
500 m		702386.6809	3077289.2599					
		702698.2200	3076992.5560					
		702357.0105	3076169.2027					
		701570.7452	3076502.9946					
		701437.2285	3076606.8410					
		700502.6112	3077126.0728					
	avg	**701632.8676**	**3077067.6592**					
	sdev	784.1225	649.6518	1	8	**1.76**	4	
39		704702.4255	3081360.5287					
GC108		705197.7102	3080932.7828					
500 m		704623.6302	3080448.7545					
		704207.1408	3081405.5546					
	avg	**704682.7267**	**3081036.9051**					
	sdev	406.3129	446.2425	1	4	**0.94**	4	
40		709246.5650	3091331.4168					
GC21		709215.7856	3091146.7403					
300 m		710241.7660	3089043.4805					
		708661.7561	3091198.0394					
	avg	**709341.4682**	**3090679.9192**					
	sdev	657.6086	1093.7323	1	4	**1.06**	2	Edge
41		719070.8551	3096698.1152					
EW993		719111.6599	3097310.1858					
250 m		718815.8257	3097279.5823					
		719172.8669	3097585.6176					
		719529.9081	3097279.5823					
	avg	**719140.2232**	**3097230.6166**					
	sdev	256.7983	324.3108	1	5	**0.87**	2	Edge

		X	Y	Sources	Total origins	Slope	Salt	Salt Edge
42		725050.9357	3095988.7960					
EW995		725250.2468	3095763.4879					
250 m		725102.9299	3096144.7786					
		724796.7420	3095512.1827					
		724834.2933	3095824.1478					
	Avg	**725007.0295**	**3095846.6786**					
	sdev	189.9592	238.9439	1	5	**1.33**	2	
43		727133.3052	3095099.1107					
EW995		727689.5260	3096129.9053					
250 m		727753.3128	3095997.2288					
	avg	**727525.3814**	**3095742.0816**					
	sdev	341.0425	560.7668	1	3	**0.75**	2	
44		711737.6820	3079109.9868					
GC154		712013.0757	3078953.3904					
500 m		712563.8631	3078812.9936					
		712941.8545	3078926.3910					
		712515.2642	3078802.1939					
		712115.6734	3078181.2081					
	avg	**712314.5688**	**3078797.6940**					
	sdev	437.9885	322.0684	1	6	**0.54**	4	
45		716489.9108	3076433.1668					
GC199		715106.1925	3076829.7203					
600 m		715738.9905	3076509.1026					
		716447.7243	3074517.8981					
		715949.9232	3074290.0909					
		715376.1863	3074771.0174					
		716523.6600	3074669.7697					
	avg	**715947.5125**	**3075431.5380**					
	sdev	570.6829	1101.0251	1	7	**2.22**	4	

		X	Y	Sources	Total origins	Slope	Salt	Salt Edge
46		714098.8711	3063731.0497					
GC287		714169.8193	3064823.6528					
900 m		715021.1984	3064057.4117					
		715163.0949	3063376.3085					
		715177.2845	3063731.0497					
		717263.1631	3065589.8939					
		714950.2501	3063035.7568					
		714709.0261	3062879.6707					
		714496.1813	3062936.4293					
	avg	**715005.4321**	**3063795.6915**					
	sdev	936.9050	914.0247	1	9	**4.71**	2	
47		716113.8014	3062269.5157					
GC331		715801.6291	3061120.1540					
900 m		716127.9911	3060964.0679					
		715858.3877	3060850.5507					
		716780.7150	3060722.8438					
		716425.9737	3061843.8262					
		716766.5254	3061545.8436					
		717859.1284	3062198.5675					
		717873.3181	3062425.6019					
		716511.1116	3060637.7059					
		716269.8876	3060623.5163					
		715886.7670	3060694.4645					
	avg	**716522.9364**	**3061324.7215**					
	sdev	706.9971	694.5543	1	12	**2.50**	2	
48		742867.4677	3069538.9073					
GC248		742421.3542	3069451.0364					
900 m		742515.9844	3069106.3123					
		742718.7632	3069545.6666					
		742617.3738	3069261.7761					
	avg	**742628.1887**	**3069380.7397**					
	sdev	173.8861	191.4564	1	5	**3.45**	2	Edge

		X	Y	Sources	Total origins	Slope	Salt	Salt Edge
49		741752.1839	3068869.7370					
GC248		741569.6829	3068484.4571					
900 m		742732.2818	3068856.2184					
		743394.6928	3068964.3671					
		741596.7201	3068315.4747					
		741522.3679	3068295.1968					
		741711.6281	3068639.9209					
		743888.1214	3068869.7370					
	avg	**742270.9599**	**3068661.8886**					
	sdev	939.5716	267.8190	1	8	**2.08**	2	Edge
50		742061.5491	3071572.6831					
GC204		744253.8609	3072001.1480					
900 m	avg	**743157.7050**	**3071786.9155**					
	sdev	1550.1985	302.9704	1	2	**0.68**	2	Edge
51		748975.1868	3064766.6915					
GC294		751800.9917	3063727.7927					
900 m		751333.4872	3063146.0093					
		749411.5244	3064319.9650					
		750284.1994	3063997.9064					
	avg	**750361.0779**	**3063991.6730**					
	sdev	1209.0480	610.9927	1	5	**2.91**	2	Edge
52		751769.8247	3061826.6078					
GC294		748798.5740	3062782.3947					
900 m		749245.3005	3062138.2775					
		752881.4465	3063540.7909					
	avg	**750673.7865**	**3062572.0177**					
	sdev	1969.0993	758.6274	1	4	**2.38**	2	Edge
53		747072.4148	3045126.1406					
GC470		747080.3508	3044737.2750					
1000 m		747199.3913	3044324.6012					
		748865.9582	3045697.5349					
		749008.8068	3045364.2215					
		750024.6190	3045887.9997					
		748873.8942	3044380.1535					
		748445.3484	3044213.4968					
		747310.4957	3044626.1705					
	avg	**748209.0310**	**3044928.6215**					
	sdev	1075.7554	617.0035	3	9	**3.64**	2	

		X	Y	Sources	Total origins	Slope	Salt	Salt Edge
54		740669.6341	3030620.0832					
GC600		742092.2165	3030752.0754					
1250 m		743441.4698	3030840.0702					
		741006.9475	3030532.0884					
		739863.0153	3029344.1589					
		740156.3313	3028390.8821					
	avg	**741204.9357**	**3030079.8930**					
	sdev	1342.7897	991.9725	1	6	**6.59**	3	
55		740786.9605	3028757.5270					
GC600		739848.3495	3029344.1589					
1250 m		743162.8196	3029857.4618					
		742605.5194	3030297.4357					
		741300.2634	3030165.4435					
		741021.6133	3030532.0884					
	avg	**741454.2543**	**3029825.6859**					
	sdev	1223.0870	664.9555	1	6	**4.76**	3	
56		774925.9818	3031891.4194					
GC607		777190.2498	3030813.1965					
1250 m		779639.3560	3029580.9418					
		773462.6794	3030736.1806					
		773770.7431	3031182.8729					
		773978.7643	3031458.8112					
		774111.0215	3031579.3987					
		774437.7747	3031843.9132					
		774332.7469	3031540.4995					
		773959.3147	3031447.1415					
		774570.0319	3030564.1299					
	avg	**774943.5149**	**3031148.9550**					
	sdev	1844.6695	681.3727	4	11	**1.37**	3	Edge
57		770325.4844	2991972.3527					
GC958		770369.5366	2990100.1320					
2000 m		770553.0877	2991495.1200					
		770993.6102	2990518.6284					
		771529.5793	2990819.6521					
		771742.4985	2990195.5785					
	avg	**770918.9661**	**2990850.2439**					
	sdev	607.3856	745.2721	2	6	**5.68**	1	

		X	Y	Sources	Total origins	Slope	Salt	Salt Edge
58		749579.4028	3002714.8882					
GC822		749147.6964	3004700.7380					
1200 m		751059.5393	3004602.0622					
	avg	**749928.8795**	**3004005.8961**					
	sdev	1002.6895	1119.1337	1	3	**1.50**	1	
59		750960.8635	3001999.4889					
GC866		749073.6895	3002184.5060					
1200 m		749900.0991	3000309.6665					
		750109.7851	3000951.0589					
	avg	**750011.1093**	**3001361.1801**					
	sdev	775.2095	886.7890	1	4	**1.13**	1	
60		756178.3446	3004799.4137					
GC823		756375.6961	3004577.3933					
1200 m		756005.6620	3004306.0349					
		755475.2797	3003812.6561					
		754698.2081	3002862.9019					
		755302.5971	3003232.9360					
		754624.2013	3003689.3114					
		754537.8600	3005046.1032					
		753316.7474	3004935.0929					
		753045.3890	3004565.0588					
		754229.4982	3003097.2568					
		754069.1501	3003047.9189					
		753575.7713	3003035.5845					
		753366.0853	3003257.6049					
	avg	**754628.6064**	**3003876.0905**					
	sdev	1107.2058	801.6728	3	14	**2.82**	1	
61		734132.2985	3013709.3476					
GC774		732187.8266	3011962.4424					
1300 m		730742.4704	3012939.8774					
		732666.1458	3012201.6020					
		732686.9423	3013428.5950					
		733134.0669	3014229.2599					
		732291.8090	3013522.1792					
	avg	**732548.7942**	**3013141.9005**					
	sdev	1028.1075	821.3047	1	7	**4.02**	2	Edge

		X	Y	Sources	Total origins	Slope	Salt	Salt Edge
62		715088.5062	3012623.6435					
GC771		715115.3295	3011778.7117					
1450 m		715262.8572	3012677.2899					
	avg	**715155.5643**	**3012359.8817**					
	sdev	93.8813	504.0222	1	3	**0.76**	1	
63		717435.5388	3014072.0978					
GC727		717636.7130	3014192.8024					
1450 m		717904.9453	3014139.1559					
		717167.3065	3014970.6760					
		718629.1725	3015855.8426					
		718843.7583	3015802.1961					
		717583.0666	3015480.3174					
		718334.1170	3016861.7137					
		717878.1221	3016338.6607					
		717690.3595	3015386.4361					
		716416.2561	3014769.5018					
		716228.4935	3014635.3856					
		716872.2510	3013294.2242					
		717194.1297	3012905.2874					
		717301.4227	3013455.1636					
	avg	**717541.0435**	**3014810.6307**					
	sdev	734.5121	1152.6575	3	15	**1.25**	1	
64		716255.3167	3015319.3780					
GC727		715450.6198	3014005.0398					
1450 m		715920.0263	3012395.6460					
		715946.8496	3013937.9817					
		716376.0212	3013280.8126					
		716000.4960	3013253.9893					
	avg	**715991.5550**	**3013698.8079**					
	sdev	321.6179	984.6872	1	6	**1.38**	1	Edge

		X	Y	Sources	Total origins	Slope	Salt	Salt Edge
65		707792.5879	3016352.0723					
GC725		707430.4743	3015533.9638					
1600 m		707846.2344	3015359.6128					
		707685.2950	3013066.2267					
		707474.9721	3013265.5907					
		706292.2584	3014689.6745					
		706326.0502	3014317.9645					
		706359.8420	3014163.4876					
		707233.6019	3012879.3985					
		707137.0539	3012763.5408					
	avg	**707157.8370**	**3014239.1532**					
	sdev	615.8987	1245.4915	1	10	**2.42**	1	
66		708930.6470	3009818.9841					
GC769		708603.3558	3010416.6462					
1500 m		709037.8783	3009882.2655					
		708373.1347	3010592.9212					
		708522.3334	3010025.6813					
	avg	**708693.4698**	**3010147.2996**					
	sdev	280.5767	340.5699	2	5	**0.99**	2	Edge
67		695252.5341	3012749.5802					
GC767		695167.6975	3012664.7436					
1400 m		695040.4427	3012562.9398					
		695608.8475	3012070.8880					
		695490.0763	3012053.9207					
		695803.9715	3012977.5783					
		694086.0319	3013221.4833					
		693820.9177	3012468.5592					
		697490.0974	3012860.9281					
		697341.6334	3012627.6276					
		696726.5686	3013985.0120					
		697458.2837	3013073.0194					
		695793.3669	3010983.9200					
		695867.5988	3010655.1785					
		696907.5090	3015023.2653					
		696112.1666	3015056.4045					
		696609.2556	3015636.3417					
		695548.7991	3015188.9616					
		693245.6200	3010698.5909					
		697205.7624	3015255.2401					
		694886.0138	3010466.6161					
		696692.1038	3010334.0590					
		695714.4954	3011411.0852					

67		X	Y	Sources	Total origins	Slope	Salt	Salt Edge
GC767		695117.9886	3011991.0223					
(Cont.)		695747.6347	3016332.2663					
	avg	**695789.4167**	**3012893.9693**					
	sdev	1113.4833	1725.9119	3	25	**6.82**	2	
68		707134.2331	3040848.0286					
GC505		707349.5238	3039705.3316					
1200 m		708003.6765	3039705.3316					
		707854.6291	3039324.4325					
		705676.8803	3041013.6369					
		705552.6741	3039564.5645					
		705892.1710	3039208.5067					
		706090.9010	3039133.9830					
		705287.7009	3039026.3376					
		707200.4764	3041253.7689					
		706844.4186	3039506.6016					
		707457.1692	3039738.4532					
		707117.6723	3038653.7190					
		705329.1029	3039374.1150					
		705221.4575	3038024.4076					
		703391.4861	3040442.2884					
		702869.8201	3040251.8389					
		703424.6078	3039241.6284					
		701795.1621	3040084.4668					
		702503.2816	3039986.1169					
		705683.2628	3038760.0210					
		705493.1196	3037769.9651					
	Avg	**705598.7921**	**3039573.5247**					
	sdev	1798.6167	879.1880	4	22	**0.12**	2	Edge
69		701637.0972	3042993.4969					
GC460		702210.5249	3042791.1107					
1300 m		702345.4491	3042436.9348					
	avg	**702064.3571**	**3042740.5141**					
	sdev	376.1175	281.7097	1	3	**5.99**	4	
70		735879.3947	2987290.3815					
GC951		733994.7814	2988754.3222					
1600 m		733742.3779	2988720.6684					
		733607.7626	2989006.7258					
		735189.4917	2990510.6304					
		734937.0881	2990725.1734					
		734722.5451	2990863.9954					

70		X	Y	Sources	Total origins	Slope	Salt	Salt Edge
GC951		734558.4827	2991002.8173					
(Cont.)		734444.9011	2991154.2595					
		734861.3670	2988478.7817					
		734735.1652	2988504.0220					
		734293.4590	2988302.0992					
		734028.4352	2988175.8974					
		732481.8355	2990423.6609					
		732217.9657	2989974.1050					
		731973.6418	2989974.1050					
		734143.2379	2990931.8546					
		734260.5133	2990443.2068					
		734495.0643	2989495.2302					
	avg	**734135.1321**	**2989617.4703**					
	sdev	1000.5491	1175.4556	4	19	**3.14**	2	
71		714230.4663	2988078.7055					
GC991		714506.2816	2988837.1976					
1600 m		714911.3854	2989526.7359					
		715350.9660	2989268.1590					
		717393.7231	2988733.7669					
		716980.0001	2990190.4164					
		718178.0728	2985329.1718					
		718221.1690	2987578.7903					
		716350.7965	2984405.8369					
		715844.4168	2984675.1878					
		716426.2147	2989060.2201					
		716566.2772	2986000.3941					
		716900.2722	2986592.9661					
		717320.4596	2987476.4370					
		717880.7094	2987185.5380					
		717628.6460	2987037.0179					
		718120.7501	2987561.9289					
	avg	**716635.9180**	**2987502.2630**					
	sdev	1288.5409	1699.5042	4	17	**0.27**	1	
72		705750.3868	2994788.4299					
GC901		705310.4614	2994268.5180					
1600 m		705540.4224	2994178.5333					
		705650.4037	2993708.6130					
		705940.3546	2994028.5587					
		703170.8242	2996168.1959					
		703810.7157	2995528.3044					
		704040.6767	2995428.3214					

72		X	Y	Sources	Total origins	Slope	Salt	Salt Edge
GC901	avg	**704901.7807**	**2994762.1843**					
(cont.)	sdev	1059.7992	865.2671	1	8	**1.04**	1	Edge
73		706310.2919	2988439.5064					
GC945		706170.3156	2988429.5081					
1600 m		705240.4733	2989719.2894					
		705360.4529	2988959.4183					
		704740.5580	2989679.2962					
		702190.9903	2992178.8724					
		702990.8547	2991409.0029					
		702860.8767	2992018.8995					
		703730.7293	2991009.0707					
		703600.7513	2991598.9707					
		703700.7343	2989149.3861					
		705250.4716	2988919.4250					
		705870.3664	2989499.3267					
		706010.3427	2989619.3064					
		706350.2851	2989929.2538					
		706560.2495	2989549.3182					
	avg	704808.6715	2990006.7407					
	sdev	1428.6278	1239.4591	5	16	**0.26**	1	
74		684542.9209	2996930.823					
GC896		683650.8061	2997376.88					
1700 m		682025.8829	2998412.371					
		682089.6053	2999001.804					
		682647.177	2994875.773					
		680369.0983	2996213.945					
		680177.9309	2996213.945					
		680114.2084	2995863.471					
	avg	**681952.2037**	**2996861.126**					
	sdev	1653.431694	1364.569454	1	8	**3.04**	1	Edge
75		693466.8302	3027764.2513					
GC590		693689.1938	3027405.0486					
1300 m		693167.4945	3027396.4961					
		692791.1869	3027704.3842					
		693680.6413	3030270.1182					
		694125.3685	3029962.2301					
		694920.7461	3029329.3490					
	avg	**693691.6373**	**3028547.4111**					
	sdev	687.3903403	1260.5878	1	7	**3.31**	2	Edge

		X	Y	Sources	Total origins	Slope	Salt	Salt Edge
76		678770.1041	3020112.2229					
GC675		678479.2592	3020623.7088					
1450 m		678068.0646	3020924.5829					
		678238.5600	3020914.5537					
		677927.6567	3020924.5829					
	avg	**678296.7289**	**3020699.9302**					
	sdev	335.1442	352.9201	1	5	**2.06**	1	
77		679464.5153	3023619.4631					
GC631		680135.7830	3022561.7079					
1450 m		679464.5153	3022429.4885					
		680379.8804	3021473.4405					
		680664.6607	3021564.9771					
		679851.0028	3022999.0490					
		679617.0762	3022531.1958					
		679434.0031	3022561.7079					
		679179.7351	3022673.5859					
		678619.6671	3022830.1187					
	avg	**679681.0839**	**3022524.4734**					
	sdev	598.9129	630.4338	2	10	**5.70**	1	
78		680680.3361	3028166.8370					
GC587		680484.4749	3027625.3384					
1500 m		680507.5174	3028178.3582					
		679724.0727	3028915.7180					
		680553.6024	3028397.2619					
		680242.5288	3028443.3469					
	avg	**680365.4220**	**3028287.8101**					
	sdev	345.0737	423.3019	1	6	**5.19**	1	Edge
79		681454.3144	3029145.2935					
GC588		681263.4753	3028703.3504					
1400 m		680962.1504	3028783.7037					
		681856.0809	3030440.9906					
		680630.6930	3029697.7225					
		680389.6331	3029346.1768					
		680078.2641	3029466.7068					
		681906.3017	3029225.6468					
		681645.1535	3028984.5869					
		681193.1662	3028894.1895					
		681866.1251	3028874.1011					
		680068.2199	3029938.7824					
		681263.4753	3028683.2620					

79		X	Y	Sources	Total origins	Slope	Salt	Salt Edge
GC588		680368.7824	3031432.1500					
(cont.)	avg	**681067.5597**	**3029401.1902**					
	sdev	660.1818	773.5363	3	14	**6.97**	2	Edge
80		681988.5867	3034309.7237					
GC544		680876.2503	3035261.7233					
1300 m		680946.3977	3035983.2388					
		681400.4301	3036802.6463					
		681412.0622	3035563.8223					
		681406.2462	3035563.8223					
	avg	**681338.3289**	**3035580.8295**					
	sdev	400.9658	821.3266	1	6	**5.35**	2	Edge
81		617854.7440	3028147.1163					
GC574		617188.9405	3028054.2135					
1100 m		616972.1672	3029525.1747					
		616925.7158	3029370.3367					
		616430.2342	3029153.5635					
	avg	**617074.3603**	**3028850.0809**					
	sdev	517.0987	697.5105	2	5	**2.29**	1	
82		617034.1025	3031290.3281					
GC574		617390.2299	3030872.2655					
1100 m		616523.1370	3031274.8443					
		614881.8540	3029602.5937					
	avg	**616457.3308**	**3030760.0079**					
	sdev	1108.9671	795.5094	2	4	**0.79**	1	
83		616368.2990	3023889.0707					
GC618		616430.2342	3023006.4940					
1100 m		614603.1455	3024740.6799					
		614308.9533	3023981.9736					
		614788.9511	3027016.7988					
		616538.6208	3025994.8678					
		616786.3616	3025669.7080					
	avg	**615689.2236**	**3024899.9418**					
	sdev	1066.9762	1399.2570	2	7	**0.64**	1	
84		616739.6307	3025845.7750					
GC618		616814.8402	3025432.1230					
1100 m		614525.7265	3026397.4467					
		615114.1110	3025716.1594					
		616306.3638	3027109.7016					

84		X	Y	Sources	Total origins	Slope	Salt	Salt Edge
GC618		616306.3638	3027527.7642					
(cont.)		614665.0807	3027481.3128					
		617235.3919	3027063.2502					
		617003.1348	3026784.5417					
	avg	**616078.9604**	**3026595.3416**					
	sdev	1037.7492	782.6805	2	9	**0.39**	1	
85		632814.1655	3017325.9799					
GC665		632294.4597	3019318.1855					
1300 m		631168.4304	3019036.6782					
		631320.0113	3018127.1930					
		631255.0481	3017629.1416					
		631016.8496	3019318.1855					
		631190.0848	3018430.3547					
		629977.4379	3019448.1119					
		632207.8421	3017347.6343					
		632402.7317	3016070.0241					
		633138.9816	3016654.6932					
		633247.2537	3015160.5390					
	avg	**631836.1080**	**3017822.2267**					
	sdev	995.7961	1384.4499	2	12	**1.31**	2	Edge
86		638942.3632	3012388.7746					
GC711		637145.0473	3014814.0684					
1500 m		635694.2019	3014575.8699					
		638964.0177	3011132.8189					
		640371.5542	3010180.0249					
		637253.3193	3013839.6200					
		636993.4664	3013579.7671					
		637513.1723	3014294.3626					
		638877.4000	3014272.7082					
		638357.6942	3012626.9731					
		638660.8559	3013103.3701					
		639007.3265	3012756.8996					
		639635.3043	3012410.4290					
	avg	**638262.7479**	**3013075.0528**					
	sdev	1272.2323	1366.4425	2	13	**3.56**	1	Edge
87		659537.8135	3033213.6393					
GC539		660697.0462	3032864.2815					
1200 m		660951.1246	3031927.3674					
		661094.0437	3031768.5684					
		661491.0412	3031847.9679					

87		X	Y	Sources	Total origins	Slope	Salt	Salt Edge
GC539		661729.2397	3031895.6076					
(cont.)		661951.5583	3032038.5267					
		662015.0779	3032467.2840					
		661697.4799	3034134.6735					
		661506.9211	3033769.4358					
		660982.8844	3034214.0730					
		660998.7643	3033721.7961					
		660236.5291	3034055.2740					
		660411.2080	3033213.6393					
		660998.7643	3034611.0705					
		661205.2030	3034769.8695					
		660665.2864	3032721.3624					
		660871.7251	3032324.3649					
		661125.8035	3031959.1272					
		661824.5191	3032292.6051					
		662062.7176	3032070.2865					
		662475.5950	3031832.0880					
		659458.4140	3033737.6760					
		661919.7985	3034229.9529					
		662078.5975	3033578.8770					
		660744.6859	3034134.6735					
		660474.7276	3033181.8795					
		659267.8552	3036087.9012					
	avg	**661088.3723**	**3033166.5667**					
	sdev	823.3786	1123.2401	5	28	**1.95**	1	Edge

88	658638.8572	2998215.2233
GC847	661408.7006	2999168.4082
1750 m	662496.4529	2999437.5428
	664234.6137	3000637.4345
	660522.7993	2999493.6125
	661431.1285	3000872.9272
	661846.0443	3002319.5256
	659064.9870	3001781.2564
	658851.9221	3002151.3165
	658661.2851	3002532.5905
	663427.2099	2999717.8913
	660590.0829	3000727.1460
	660231.2368	3000570.1508
	659356.5494	3000368.2999
	659378.9773	3000536.5090
	661666.6212	3000637.4345

88		X	Y	Sources	Total origins	Slope	Salt	Salt Edge
GC847		658616.4294	3002364.3814					
(cont.)	avg	**660613.1704**	**3000678.3324**					
	sdev	1749.3319	1243.5973	3	17	**0.75**	1	
89		666372.4826	3004010.8601					
GC849		666405.3721	3003660.0394					
1800 m		666909.6770	3002826.8400					
		667370.1293	3001193.3307					
		665647.5702	3003149.3572					
		666331.6206	3002498.9486					
		665703.6399	3003743.6961					
		666398.9042	3002173.7444					
		667845.5026	3001904.6098					
		666656.8249	3002925.0784					
		667139.0243	3002992.3620					
		667318.4474	3002891.4366					
		667598.7959	3002655.9438					
	avg	**666745.9993**	**3002817.4036**					
	sdev	688.1982	772.6008	4	13	**4.85**	1	Edge
90		662042.0385	3010226.9660					
GC760		662721.7538	3010139.2609					
2000 m		663094.5009	3010731.2709					
		663061.6114	3010259.8555					
		661548.6968	3013088.3481					
		662403.8224	3013033.5324					
		663730.3636	3012134.5541					
		661943.3701	3014184.6631					
		662107.8174	3013230.8691					
		662283.2278	3013088.3481					
		662524.4171	3012605.9695					
		661746.0335	3011498.6914					
		660551.0501	3011586.3966					
		661428.1021	3011257.5021					
		660507.1975	3011301.3547					
		661658.3283	3011476.7651					
	avg	**662084.5207**	**3011865.2717**					
	sdev	867.9683	1232.8611	3	16	**5.44**	1	Edge
91		655096.0588	2998210.5664					
GC890		655301.4881	2998572.5131					
1750 m		656025.3816	2996400.8324					
		656866.6633	2995549.7684					

91		X	Y	Sources	Total origins	Slope	Salt	Salt Edge
GC890		655614.5231	2994043.2872					
(cont.)		655399.3115	2994199.8047					
		655281.9234	2994297.6282					
		655907.9935	2995960.6269					
	avg	**655686.6679**	**2995904.3784**					
	sdev	573.8194	1763.2641	3	8	**0.53**	1	
92		660652.4311	2992644.4118					
GC891		660975.2485	2992438.9825					
1750 m		661219.8071	2992448.7649					
		661640.4480	2995129.1275					
		661943.7007	2994649.7926					
		661894.7889	2994053.0695					
		660583.9546	2996576.9147					
		660623.0840	2996332.3560					
		660691.5604	2995941.0622					
	avg	**661136.1137**	**2994468.2757**					
	sdev	560.6554	1667.9051	3	9	**2.28**	1	
93		613020.2905	2988909.1561					
GC969		612647.0677	2988370.0565					
1600 m		612470.8236	2988214.5470					
		610158.9157	2990288.0070					
	avg	**612074.2744**	**2988945.4417**					
	sdev	1297.2906	943.2344	1	4	**0.69**	1	Edge
94		601665.2205	2974269.8626					
KC129		603619.2188	2972234.4477					
1700 m		606143.1332	2972153.0312					
		605166.1341	2972315.8643					
		605695.3420	2971053.9071					
		604942.2385	2971664.5316					
	avg	**604538.5478**	**2972281.9408**					
	sdev	1647.4752	1082.6928	1	6	**4.42**	1	
95		606529.8621	2969018.4922					
WR133		609827.2342	2970280.4495					
1750 m		608544.9228	2967166.2647					
	avg	**608300.6730**	**2968821.7355**					
	sdev	1662.2001	1566.3881	1	3	**0.39**	1	
96		628761.1961	2976443.4188					
WR49		625310.5561	2978411.6538					
1750 m								

96		X	Y	Sources	Total origins	Slope	Salt	Salt Edge
WR49		626518.9030	2978847.6553					
(cont.)		626693.3036	2979096.7989					
		629446.3412	2976406.0472					
		631414.5763	2975035.7570					
		630467.8303	2978885.0268					
		629483.7128	2978872.5696					
		629408.9697	2977801.2518					
	avg	**628611.7099**	**2977755.5755**					
	sdev	2011.6520	1452.9184	3	9	**2.81**	1	Edge
97		639955.3799	2972567.6125					
WR95		640071.9713	2972392.7255					
1800 m		639733.8564	2969804.3981					
		638789.4667	2971110.2209					
	avg	**639637.6686**	**2971468.7393**					
	sdev	582.5970	1285.7994	1	4	**0.43**	1	Edge
98		648078.2619	2977597.3790					
WR9		647204.2163	2978951.5342					
1800 m		647610.4629	2978668.3926					
		647007.2483	2981709.0866					
		647093.4218	2980330.3104					
	avg	**647398.7222**	**2979451.3405**					
	sdev	444.6631	1594.5213	1	5	**0.58**	1	Edge
99		616185.1884	2958660.5519					
WR222		616476.6446	2957841.6987					
1850 m		615185.9098	2956814.6625					
		612479.5305	2960506.4414					
		613145.7162	2959715.3459					
		613437.1725	2959340.6165					
		613686.9921	2959090.7968					
		619016.4775	2957924.9719					
	avg	**614951.7039**	**2958736.8857**					
	sdev	2193.8452	1179.5755	1	8	**1.78**	1	
100		644345.9702	3049482.9757					
GC404		644326.1249	3049360.5962					
900 m		644104.5187	3050637.3122					
		644130.9792	3050686.9255					
	avg	**644226.8982**	**3050041.9524**					
	sdev	126.7560	718.1330	2	4	**0.38**	2	Edge

		X	Y	Sources	Total origins	Slope	Salt	Salt Edge
101		645618.6003	2956301.2645					
WR229		645224.9451	2954775.8507					
1850 m		645421.7727	2954398.5978					
		645749.8187	2953676.8967					
		647357.2439	2951708.6208					
		647800.1060	2956416.0806					
		647209.6232	2956432.4829					
		648242.9681	2956350.4714					
		648242.9681	2955284.3220					
		648685.8301	2954677.4369					
		649145.0945	2953955.7358					
		650178.4393	2952315.5059					
	avg	**647406.4508**	**2954691.1055**					
	sdev	1611.8317	1592.7949	6	12	**1.03**	1	
102		556686.3737	2998553.7722					
GB911		556918.6762	2998151.1146					
1500 m	avg	**556802.5249**	**2998352.4434**					
	sdev	164.2626	284.7219	1	2	**1.25**	1	Edge
103		553827.5048	3001038.6342					
GB866		553914.2311	3001162.5288					
1300 m	avg	**553870.8679**	**3001100.5815**					
	sdev	61.3247	87.6067	1	2	**10.36**	1	Edge
104		535204.0488	2996262.5562					
GB907		536212.6988	2996080.9992					
1300 m		535708.3738	2995546.4147					
		536898.5808	2995586.7607					
		535183.8758	2996666.0162					
		537412.9923	2995959.9612					
		537423.0788	2996696.2757					
	avg	**536291.9499**	**2996114.1406**					
	sdev	971.4584	463.8224	4	7	**2.14**	1	
105		521303.6756	3049895.4974					
GB419		521352.3479	3050024.6279					
800 m	avg	**521328.0118**	**3049960.0627**					
	sdev	34.4165	91.3091	1	2	**3.38**	2	
106		540504.2293	3041108.7669					
GB512		541041.3561	3041202.7641					
700 m		541135.3533	3040712.6359					

106		**X**	**Y**	**Sources**	**Total origins**	**Slope**	**Salt**	**Salt Edge**
GB512	avg	**540893.6463**	**3041008.0556**					
(cont.)	sdev	340.5041	260.1221	1	3	**2.50**	2	Edge
107		531107.6844	3026193.8619					
GB642		531164.3129	3025783.3057					
900 m	avg	**531135.9987**	**3025988.5838**					
	sdev	40.0424	290.3071	1	2	**0.80**	2	
108		630012.9966	2991621.9109					
GC929		630724.6591	2989861.4827					
1650 m	avg	**630368.8279**	**2990741.6968**					
	sdev	503.2213	1244.8107	1	2	**4.33**	1	Edge
109		628015.3477	2990722.9688					
GC929		629501.0991	2990061.2476					
1650 m	avg	**628758.2234**	**2990392.1082**					
	sdev	1050.5849	467.9076	1	2	**7.64**	1	Edge
110		698957.2460	3079952.5926					
GC151		699089.0898	3078912.4912					
500 m		700363.5803	3078604.8555					
	avg	**699469.9720**	**3079156.6464**					
	sdev	776.6901	706.2632	1	3	**4.25**	4	
111		657191.4779	3043698.7448					
GC451		656847.8549	3043845.4603					
1000 m	avg	**657019.6664**	**3043772.1025**					
	sdev	242.9782	103.7435	1	2	**2.93**	1	Edge
112		673143.2318	3055961.6432					
GC366		673548.4503	3054965.6845					
900 m		672464.6128	3055390.4316					
	avg	**673052.0983**	**3055439.2531**					
	sdev	547.6357	499.7711	2	3	**5.28**	2	
113		705663.3979	3059529.3839					
GC329		705986.1454	3057868.7016					
900 m	avg	**705824.7716**	**3058699.0427**					
	sdev	228.2169	1174.2797	1	2	**9.88**	4	

APPENDIX B

PERSISTENCE ANALYSIS OF SYNTHETIC APERTURE RADAR (SAR) IMAGES USED IN THIS STUDY. THE BLOCK, DEPTH AND # (NUMBER OF SOURCES) ARE THE SAME AS APPENDIX A. “X” MEANS THAT AT LEAST ONE SLICK WAS PRESENT AT THAT SITE ON THAT DAY. “N/A” MEANS THAT THE SEEP LOCATION WAS OUTSIDE OF THE PERIMETER OF THE SAR IMAGE TAKEN ON THAT DAY. THE LAST TWO COLUMNS ARE THE CALCULATED PERCENTAGES OF SLICKS CAPTURED BY THE IMAGES.

Block	Depth	#	9-Jul-01	12-Jul-01	16-Jul-01	19-Jul-01	22-Jul-01		10-Jun-02	17-Jun-02	20-Jun-02	4-Jul-02	11-Jul-02	14-Jul-02	2001%	2002%
Shelf	100	1		n/a	X						X				25	17
GC185	550	1		n/a	X	X	X			X		X	X		75	50
GC227	500	1		n/a	X		X				n/a			n/a	50	0
GC271	600	1		n/a	X	X	X				n/a			n/a	75	0
GC272	650	1		n/a	X	X	X				n/a		X	n/a	75	25
GC273	650	1		n/a	X	X	X							X	75	17
GC273	600	1		n/a	X	X	X			X					75	17
GC316	800	1		n/a	X	X	X			X	n/a		X	n/a	75	50
GC320	800	1		X	X	X	X				X				80	17
GC321	800	1		X	X	X	X				X				80	17

Block	Depth	#	9-Jul-01	12-Jul-01	16-Jul-01	19-Jul-01	22-Jul-01		10-Jun-02	17-Jun-02	20-Jun-02	4-Jul-02	11-Jul-02	14-Jul-02	2001%	2002%
GC320	800	1		X	X	X					X				60	17
GC451	1000	1		n/a	X		X			X	X				50	33
GC407	1000	1		n/a	X		X			X	X				50	33
GC407	1000	1		n/a	X		X			X	X				50	33
GC448	1000	1		n/a	X	X					n/a	X	X	n/a	50	50
GC448	1000	1		n/a	X	X					n/a	X	X	n/a	50	50
GC357	800	1		n/a	X		n/a			X	n/a			n/a	33	25
GC402	800	1		n/a	X		n/a			X	n/a	X		n/a	33	50
GC416	900	1	n/a	X	X	X	X		n/a	X		n/a	X	X	100	75
GC416	900	1	n/a	X	X	X	X		n/a			n/a		X	100	25
GC415	900	1	n/a	X	X	X	X		n/a		X	n/a	X		100	50
GC415	900	1	n/a	X	X	X	X		n/a			n/a			100	00
GC415	900	1	n/a	X	X	X	X		n/a			n/a	X		100	25
GC415	900	1	n/a	X	X	X			n/a			n/a	X		75	25
GC415	900	1	n/a	X	X	X			n/a			n/a	X		75	25
GC99	250	1				X				X	X	X	X		20	67
GC99	250	1		X						X	X	X			20	50
GC143	330	1		X	X	X	X			X	X	X	X	X	80	83
GC232	650	1		X	X	X	X			X	X	X			80	50
GC233	550	1		X	X	X				X		X			60	33
GC233	550	1		X	X	X				X		X			60	33
GC234	550	1		X	X	X					X				60	17
GC235	550	1		X	X	X					X				60	17
GC235	550	1		X	X	X	X				X				80	17
GC235	550	1		X	X	X					X				60	17
GC148	450	1	X	X	X					X	X	X	X		60	67
GC237	600	1		X	X					X	X	X			40	50
GC152	500	1	n/a	X	X	X			n/a			n/a	X		75	25
GC108	500	1	n/a	X	X				n/a		X	n/a	X		50	50
GC21	300	1	n/a	X	X				n/a		X	n/a	X		50	50

Block	Depth	#	9-Jul-01	12-Jul-01	16-Jul-01	19-Jul-01	22-Jul-01		10-Jun-02	17-Jun-02	20-Jun-02	4-Jul-02	11-Jul-02	14-Jul-02	2001%	2002%
EW993	250	1	n/a	X	X				n/a		X	n/a	X		50	50
EW995	250	1	n/a	X			X		n/a		X	n/a	X	X	50	75
EW995	250	1	n/a	X					n/a		X	n/a	X		25	50
GC154	500	1	n/a	X	X		X		n/a	X	X	n/a	X	X	75	100
GC199	600	1	n/a	X	X				n/a		X	n/a	X		50	50
GC287	900	1	n/a	X	X	X	X		n/a	X		n/a	X	X	100	75
GC331	900	1	n/a	X	X	X	X		n/a	X	X	n/a	X	X	100	100
GC248	900	1	n/a	X		X			n/a			n/a	X	X	50	50
GC248	900	1	n/a	X		X			n/a	X	X	n/a	X	X	50	100
GC204	900	1	n/a	X					n/a		X	n/a			25	25
GC294	900	1	n/a	X			n/a		n/a	X	X	n/a	X	X	33	100
GC294	900	1	n/a	X			n/a		n/a	X	X	n/a	X		33	75
GC470	1000	3	n/a	X		X			n/a			n/a		X	50	25
GC600	1250	1	n/a	X			X		n/a	X	X	n/a	X	X	50	100
GC600	1250	1	n/a	X			X		n/a	X	X	n/a	X	X	50	100
GC607	1250	4	n/a	X	X		n/a		n/a	X	n/a	n/a	X	n/a	67	100
GC958	2000	2	n/a	X	X		n/a		n/a	X	n/a	n/a	X	n/a	67	100
GC822	1200	1	n/a	X	X		n/a		n/a	X	n/a	n/a	X	n/a	67	100
GC866	1200	1	n/a	X	X		n/a		n/a	X	n/a	n/a	X	n/a	67	100
GC823	1200	3	n/a	X	X		n/a		n/a	X	n/a	n/a	X	n/a	67	100
GC774	1300	1	n/a	X	X	X	n/a		n/a	X	X	n/a	X	X	100	100
GC771	1450	1	n/a	X	X	X	n/a		n/a			n/a			100	00
GC727	1450	3	n/a	X	X	X	n/a		n/a	X	X	n/a	X	X	100	100
GC727	1450	1	n/a	X	X		n/a		n/a			n/a	X	X	67	50
GC725	1600	1	n/a	X	X	X			n/a	X	X	n/a		X	75	75
GC769	1500	2	n/a	X	X	X	n/a		n/a			n/a			1.00	00
GC767	1400	3	n/a	X	X	X	X		n/a	X	X	n/a	X	X	1.00	100
GC505	1200	4	n/a	X			X		n/a	X	X	n/a	X	X	50	100
GC460	1300	1	n/a	X		X			n/a		X	n/a		X	50	50
GC951	1600	4	n/a	X	X	X	n/a		n/a	X	n/a	n/a	X	n/a	100	100

Block	Depth	#	9-Jul-01	12-Jul-01	16-Jul-01	19-Jul-01	22-Jul-01		10-Jun-02	17-Jun-02	20-Jun-02	4-Jul-02	11-Jul-02	14-Jul-02	2001%	2002%
GC991	1600	4	n/a	X	X	X	n/a		n/a	X	n/a	n/a	X	n/a	100	100
GC901	1600	1	n/a	X	X	X	n/a		n/a	X	n/a	n/a		n/a	100	50
GC945	1600	5	n/a	X	X	X	n/a		n/a		n/a	n/a		n/a	100	00
GC896	1700	1			X	X	n/a			X	X	n/a	X	X	50	80
GC590	1300	1	n/a	X	X	X	X		n/a	X	X	n/a	X		100	75
GC675	1450	1		X	X		X				X				60	17
GC631	1450	2		X	X		X			X			X		60	33
GC587	1500	1		X	X	X	X							X	80	17
GC588	1400	3		X	X	X	X			X	X			X	80	50
GC544	1300	1		X	X		X			X	X				60	33
GC574	1100	2		n/a	X	X	n/a			X	n/a	X		n/a	50	50
GC574	1100	2		n/a	X	X	n/a			X	n/a			n/a	67	25
GC618	1100	2		n/a	X	X	n/a			X	n/a	X		n/a	67	50
GC618	1100	2		n/a	X	X	n/a			X	n/a	X		n/a	67	50
GC665	1300	2		n/a	X	X	n/a		X	X	n/a	X	X	n/a	67	100
GC711	1500	2		n/a	X	X	n/a		X	X	n/a	X	X	n/a	67	100
GC539	1200	5		n/a	X	X	X			X	X	X		X	75	50
GC847	1750	3		n/a	X	X	n/a		X	X	n/a	X	X	X	67	100
GC849	1800	4		n/a	X	X	n/a			X	X	X	X	X	67	83
GC760	2000	3		n/a	X	X				X		X		X	50	50
GC890	1750	3		n/a	X		n/a			X	n/a	X		n/a	33	50
GC891	1750	3		n/a	X		n/a			X	n/a	X		n/a	33	50
GC969	1600	1		n/a	X	X	n/a			X	n/a	X		n/a	67	50
KC129	1700	1		n/a	X	X	n/a		X	X	n/a	X		n/a	67	75
WR133	1750	1		n/a	X	X	n/a				n/a	X	X	n/a	67	50
WR49	1750	3		n/a	X	X	n/a			X	n/a	X		n/a	67	50
WR95	1800	1		n/a	X		n/a			X	n/a	X		n/a	33	50
WR9	1800	1		n/a	X		n/a		X	X	n/a	X		n/a	33	75
WR222	1850	1		n/a	n/a	X	n/a		X		n/a	X		n/a	50	50
GC404	900	2		n/a	X	X					n/a	X	X	n/a	50	50

Block	Depth	#	9-Jul-01	12-Jul-01	16-Jul-01	19-Jul-01	22-Jul-01		10-Jun-02	17-Jun-02	20-Jun-02	4-Jul-02	11-Jul-02	14-Jul-02	2001%	2002%
WR229	1850	6		n/a	X		n/a			X	n/a	X		n/a	33	50
GB911	1500	1	n/a	n/a	n/a	n/a	n/a		X	n/a	n/a	X	n/a	n/a	n/a	100
GB866	1300	1	n/a	n/a	n/a	n/a	n/a		X	n/a	n/a	X	n/a	n/a	n/a	100
GB907	1300	4	n/a	n/a	n/a	n/a	n/a		X	n/a	n/a	X	n/a	n/a	n/a	100
GB419	800	1	n/a	n/a	n/a	n/a	n/a		X	n/a	n/a	X	n/a	n/a	n/a	100
GB512	700	1	n/a	n/a	n/a	n/a	n/a		X	n/a	n/a	X	n/a	n/a	n/a	100
GB642	900	1	n/a	n/a	n/a	n/a	n/a		X	n/a	n/a	X	n/a	n/a	n/a	100
GC929	1650	1		n/a	X		n/a				n/a	X		n/a	33	25
GC929	1600	1		n/a	X		n/a				n/a	X		n/a	33	25
GC151	500	1	n/a		X	X						n/a	X		50	20
GC451	1000	1		n/a			X						X		25	17
GC366	900	2		X		X									40	00
GC329	900	1	n/a			X			n/a			n/a		X	25	25

APPENDIX C

SAMPLE SIZE VERSUS ACCURACY OF MEAN ESTIMATE BASED ON A 90% CONFIDENCE INTERVAL.

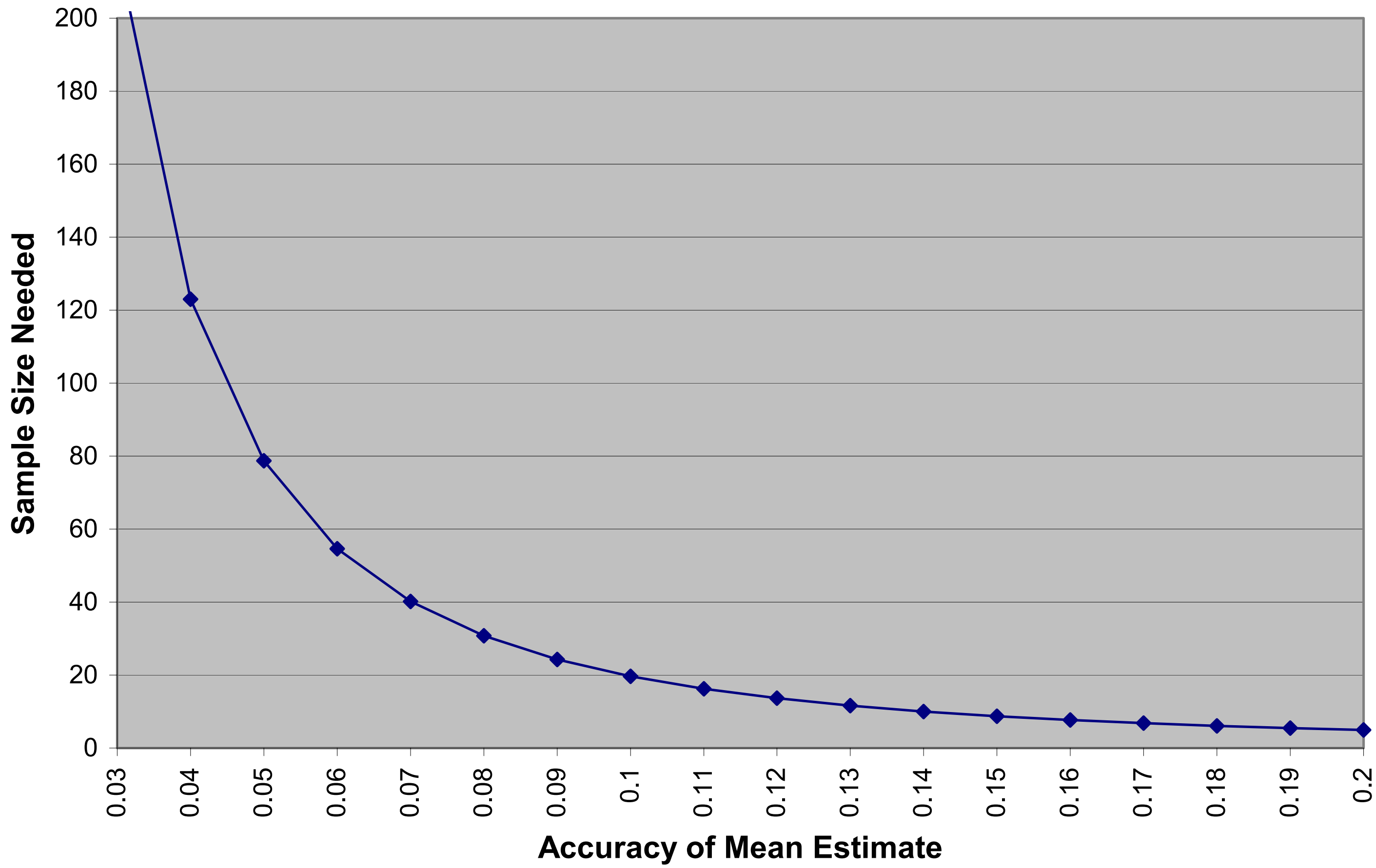

VITA

Sophie Magdalena De Beukelaer

182 Swan Sea Lane; Madison, MS, 39110

Education

Texas A&M University, College Station, TX — August 2003
M.S., Oceanography
GPA 4.0, Phi Kappa Phi Honor Society

New College, Sarasota, FL — May 1997
B.A., Natural Sciences
Thesis: "The Analysis of *Tozeuma carolinense* as an Indicator Species for Non-Point Pollution in the Sarasota Bay."

Professional Experience

Graduate Research Assistant — May 2000 – July 2003
Geochemical and Environmental Research Group, College Station, TX

- Participate as navigator, data manager, and GIS technician in three research programs (Life in Extreme Environments, Deep Gulf of Mexico Benthos, and Northern Gulf of Mexico Ecology Alvin Cruise)
- Plan and administer four side-scan sonar surveys of chemosynthetic communities with the Johnson Sea Link submersible

Chemical Analyst — July 1998 -November 1999
AnalySys, Inc., Austin, TX

- Analyze water, soil, and waste samples for metals contamination employing five analytical instruments
- Reduced sample turnover time while increasing sample quality assurance
- Passed the EPA mercury test for the company, which it had not accomplished in eight years

Physical Science Technician — July 1997 – June 1998
Environmental Careers Organization, Arvada, CO

- Prepare water samples using solid phase extraction techniques for pesticide and herbicide analysis at the USGS National Water Quality Laboratory